RF subsystem power consumption and induced radiation emulation

Musiige, Deogratius

Publication date:
2013

Document Version
Publisher's PDF, also known as Version of record

RF subsytem power consumption and induced radiation emulation

Deogratius Musiige

Kongens Lyngby 2013
DTU space-PhD-2013-304

Technical University of Denmark
National Space Institute
Elektrovej, building 327+328 and
Ørsteds Plads, building 348 DK-2800 Kgs. Lyngby
Phone +45 45259730,
Fax +45 45882673
reception@space.dtu.dk
www.space.dtu.dk DTU space-PhD-2013-304

Summary

The thesis introduces a novel approach towards the emulation of the RF subsystem power consumption when transmitting a LTE signal. The RF subsystem which is made up of analog components has not been covered by the status quo emulation methodologies which are compatible with digital circuits. Though the study of the RF subsystem architectures revealed numerous architectures with different impacts on power consumption, we have decided to consider the RF subsystem as a black box.

The RF subsystem power emulation has been studied for the telecommunication technology *Long Term Evolusion (LTE)*. Given the fact that major power consumptions of wireless devices are largely functions of sequences of protocol/logical activities, it is this technology that provided the inputs to the RF subsystem as a black black box which are Tx power, carrier frequency and signal bandwidth. The physical environmental variable temperature has also proven to be very influential on power consumption. These inputs also do constitute to the input parameters of the emulation methodology.

The emulation methodology has been proven to be a mathematical mapping between the input parameters and a predefined mathematical model. For the mathematical model, multivariate modeling approaches were analyzed for an approach with the least modeling error and complexity. Herein, the homotopy continuation numerical approach proved to have the least modeling error of 3%. The RF subsystem power consumption has been emulated with accuracies of 84% $\pm$2.25% and 94.3% $\pm$2.25% on different devices.

Resume

Denne afhandling introducerer en ny tilgang til emulering af RF subsystemets strømforbrug. RF subsystemet, som består af analoge komponenter, er ikke blevet dækket af nuværende emulerings metoder, der er kompatible med digitale kredsløber. Selvom evalueringen af RF subsystemers arkitekturer afslørede adskillige arkitekturer med forskellige virkninger på strømforbrug, har vi besluttet at betragte RF subsystemet som en sort boks.

Emuleringen af RF subsystemets strømforbrug er blevet undersøgt for telekommunikationsteknologi "*Long Term Evolusion (LTE)*". I betragtning af at de store strømforbruge af trådløse enheder er stort set funktioner af sekvenser af protokol /logiske aktiviteter, det er denne teknologi, der fastsat input til RF subsystemet. Disse input er transmissionsstyrke, frekvens og signal båndbredde og det fysiske miljø variable temperatur som også har vist sig til at have en stor indflydelse på strømforbruget. Disse input udgør også de input parametre til emulering metodologien.

Emulering metodologien har vist sig at være en matematisk mapping mellem input parametre og et foruddefineret matematisk model. For at finde matematiske modelet, blev multivariabel modelleringsmetoder analyseret for en model med mindste modellering fejl og kompleksitet. Heri "homotopy continuation" numeriske tilgang viste sig at have den mindste modellering fejl på 3%. RF subsystemets strømforbrug er blevet emuleret med nøjagtigheder af 84% $\pm$2.25% og 94% $\pm$2.25% på forskellige enheder.

Preface

This thesis was prepared at the National Space Institute of the Technical University of Denmark in fulfilment of the requirements for acquiring the degree of Doctor of Philosophy.

The thesis deals with the emulation of the RF subsystem power consumption. The thesis also looked into the possibilities of emulating the induced SAR when using the wireless devices close to our bodies. The experimental part of this research have been mainly conducted at the Renesas Mobile Europe site where all power measurements related to the thesis where conducted in the SW laboratory. The microwave laboratory of the Colorado University at Boulder was used for the radiation studies. This research was funded by Nokia/Renesas Mobile Europe, The Danish Ministry for Innovation and an industrial Ph.D scholarship.

The thesis presents the summary of the research conducted in five chapters. The introductory part consists of the introduction to the problem and the concepts and the status quo over the previously applied approaches. The rest of the thesis summaries our published work on the approaches applied for solving the task in this research.

The industrial supervision of the research has been conducted by Vincent Laulagnet and the academic supervision by Francois Anton, and Darka Mioc of The Danish Space Institute at the Technical University of Denmark.

Lyngby, 30-June-2013

Deogratius Musiige

Publications

Shortlisted below are the patents and scientific publications (journal and conference papers) made during the course of this work. All the publications directly concerned with the problem at task.

Patents

- METHOD AND APPARATUS FOR PROVIDING A DYNAMIC PAGING PERIOD(Link), Europe PCT/IB2009/052039
- Methods, devices and computer program products providing for establishing a model for emulating a physical quantity which depends on at least one input parameter, and use thereof(Link), United States 20130013270

Journal papers:

- D. Musiige, F. Anton, V. Yatskevich, L. Vincent, D. Mioc, and N. Pierre, "Rf power consumption emulation optimized with interval valued homotopies," World Academy of Science, Engineering and Technology 81 2011, vol. 81, pp. 147-153, Sep 2011.(Published)
- D. Musiige, F. Anton, V. Laulagnet, Florin Apetri and Darka Mioc "LTE RF subsystem power consumption modeling," : IEEE Transactions on Very Large Scale Integration Systems 2013 (Under review)

Conference papers (all published)

- Deogratius Musiige, Laulagnet Vincent, Francois Anton, Darka Mioc "Lte handset rf power consumption emulation," in The Third International Conference on Digital Information Processing and Communications, February 2013, pp. 371-378.
- D. Musiige, V. Laulagnet, and F. Anton, "LTE RF subsystem power consumption modeling," in The 1st IEEE Global Conference on Consumer Electronics 2012 (IEEE GCCE 2012), Tokyo, Japan, Oct. 2012.
- D. Musiige, L. Vincent, and F. Anton, "Lte modem power consumption, sar and rf signal strength emulation," in Ultra Modern Telecommunications and Control Systems and Workshops (ICUMT), 2012 4th International Congress on, 2012, pp. 1-6.

Acknowledgements

Praise be to God for providing me with the gift of life and the intellect to reach this academic stage.

My greatest gratitude to Vincent Laulagnet and Francois Anton my main supervisors, for proposing the project and pursuing the application processes through Nokia, DTU and the Danish Ministry of Innovation. The whole supervisory team which also included Darka Mioc, the co-supervisor, have done a great job in guiding, supervising and motivating during the whole coarse of this project. I do appreciate all of your work that you have invested in me.

My colleagues at Renesas, without spelling any names, you have been very helpful in my research with your guidance especially for the practical stuffs in the SW Laboratory. And a special thanks to the colleagues who reviewed my work and attended my talks.

Lastly my family, my parents who put me on the right path from day one and taught me always to pursue for the highest. My siblings who have always been there as my biggest motivator and my friends, especially Muhan who have always peep talked me through hard times. I want to say thank you. And my one and only, thanks for enduring my long working hours and the support.

Contents

List of Figures

List of Tables

Chapter 1

Introduction

Wireless devices as cellular phones, portable and mobile devices have become an integral part of our daily lives. The complexity of our expectations for these devices is also on a rampage. We are expecting these devices to provide cellular, high data rates and GPS connections on top of elegant, smart and slim designs. Our dependence on these gadgets makes a "wishing-full thinking" requirement that they can operate indefinitely on a single charge of the battery or realistically a single charge a day.

On the other hand, electromagnetic exposure regulatory bodies are tightening on the allowable electromagnetic radiation. The demand for slim and tender devices makes this very challenging as the users are increasingly exposed to electromagnetic radiation as the distance between the radiating devices and users' bodies shrink [1].

From a wireless modem chipset point of view, the target is to apply technologies that would achieve the highest possible data rates at a minimal production price and power consumption per throughput bit. Sophisticated modulation and access schemes, such as OFDMA and SC-FDMA in LTE [2] down-link and uplink respectively, have been introduced to increase capacity and meet the high data rate demands.

However, in terms of minimal production price and power consumption per

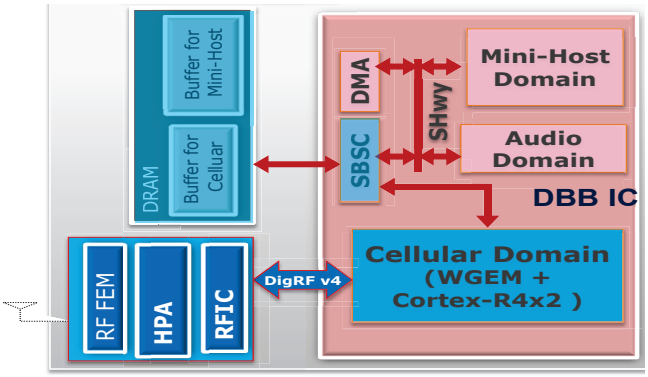

Figure 1.1: The wireless modem whose power consumption is emulated in this work. The modem consists of two main modules, the Digital Base Band Integrated Circuit (DBB IC) and the RF subsystem made up of the RFIC (Radio Frequency Integrated Circuit), HPA (High Power Amplifier) and RF FEM (Front End Modules).

throughput bit for a wireless handset, the low cost and low power consumption criteria are heavily influenced by both the baseband (BB) and radio-frequency (RF) components [3] of the modem shown in Figure 1.1. This is stated with respect to the double and quad core application processors applied in today's smart-phones because seen over 24 hours, the modem would be active for every given paging period of around a second. A power consumption analysis of a smartphone [4] showed that the modem consumes on average 80.6% and 59% of the total smartphone power (excluding the blacklight) for a GSM phone call and General Packet Radio Service (GPRS) emailing, respectively. In the uplink direction, measurements conducted in this work show the RF subsystem as the worst power consumer as a function of the transmission power (Tx power). Figure 1.2 shows the distribution of the power consumption among modem modules when transmitting at Tx powers of $0dBm$ and $23dBm$ where the RF subsystem (RFIC and PA) consumes 61% and 86% of the total modem power consumption.

It is of interest for modem chipset developers to be able to predict the average power consumption when transmitting a LTE signal, at sub-frame resolution, of the wireless modem during the design process as it relates to the different components. In this work our main focus is the RF subsystem which is the main power consumer in the modem however, approaches towards the extension of the methodology to the whole modem will be taken. Our intention is to have predictions that do reflect realistic scenarios, for example uploading data while

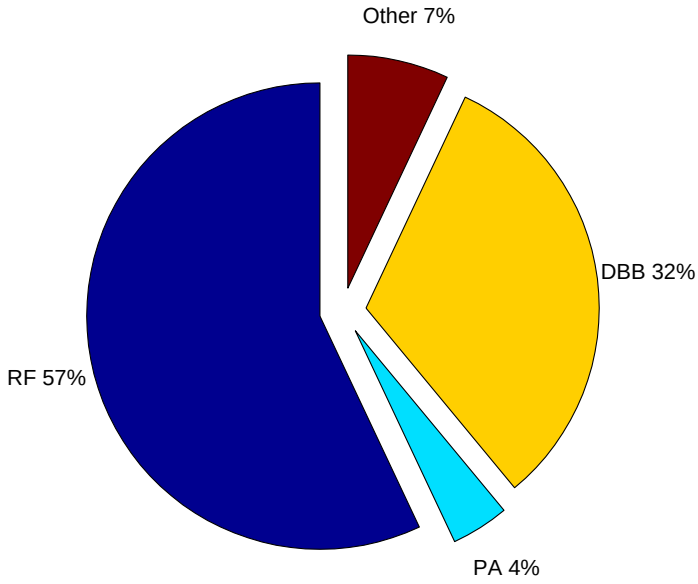

,

(a) Max throughput at 0 dBm

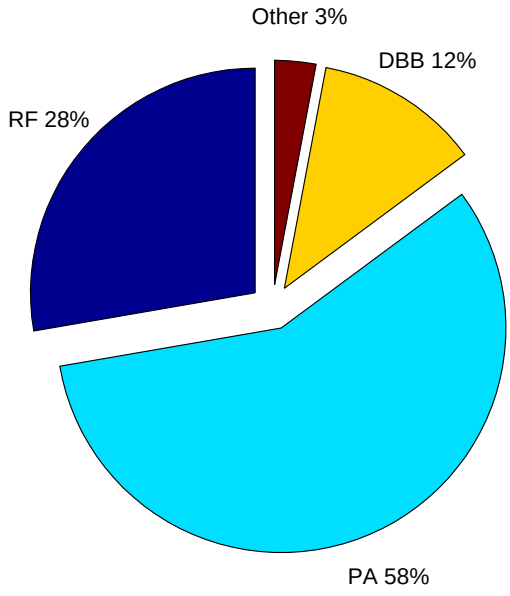

,

(b) Max throughput at 23 dBm

Figure 1.2: Modem power consumption distribution during a max throughput scenario at 0 and 23 dBm transmition powers of a Renesas Mobile Europe modem in development. The RF power constitutes the RF FEM and RFIC and PA is the power amplifier.

,

driving through a metropolitan area or while sitting in a fast moving train. Scenarios where the device is challenged by the highly alternating transmission power requests (from the base-station) and carrier frequencies as the device moves from/to various base-stations. According to Friis Transmission Equation [5],

$$\frac{P_r}{P_t} = \left(\frac{\lambda}{4\pi R}\right)^2 G_{0t} G_{0r}$$

where P_r and P_t are the received and transmitted powers, λ the wave length, R the distance between the transmitter and receiver, G_{0t} and G_{0r} are the maximum gains for transmitter and receiver antennas,

the transmitted power would at least be attenuated by $\frac{1}{R^2}$ for at distance R between the transmitting device and the base-station while not considering all the other interferences that do exist in the transmission path. The carrier frequencies will change as the device also pursues to connect to a stronger signal as it is driven through various cells. Hence, in the pursuit for designing power efficient devices, it's absolutely vital to be able to estimate the power consumption of the wireless modem in these worst case realistic scenarios.

A formal method for achieving this prediction is referred to as *emulation*. In contrast to simulation predictions, in the emulation approach some functional parts of the emulation system have to be carried out by the targeted real system [6]. Power emulation approaches for the digital circuits, as in the digital baseband in modem, have been publicized and commercialized at the *RTL (Register Transfer Level)* and gate levels. Extensive work has been published on the estimation of power consumption for *SoC (System-on-Chip)* systems at various levels of abstraction [7–10]. Figure 2.18 shows the levels of abstraction during the design of SoC systems. We can observe that the amount of information increases by an order of magnitude as the design maneuvers from system level to transistor level [11]. Consequently, the accuracy of power consumption estimation also increases as more knowledge is gained when the design transverses from the system level to the transistor level.

Approaches for power estimation at the RTL level of abstraction have been commercialized into power estimating tools [12–17]. The applicability of the PowerTheater [15], SpyGlass [13] and Cadance power estimation [12] tools were analyzed in a feasibility study conducted by Nokia [18] where it was verified that the power consumption of the digital baseband could be emulated with relative errors of 10% and 20% at gate and RTL levels respectively. These approaches are appropriate for digital circuits, as the digital baseband, with discrete signals as they take the discrete transitions as inputs to estimate the power consumption

of a given digital device.

Power estimation methodologies of analog circuits which are of most interest in this work, have been defined at the system level of abstraction [19–22]. At the system level of design, attributes like the architecture and technology are not known and this makes it impossible to conduct accurate power estimates. The power estimation methodologies of analog circuits are based on the notion that the estimated power value is the power consumed by a functional block when given relevant input specifications, including the target technology, without knowing the detailed implementation of the block (see overview).

In this work, we are focusing on power estimation by means of emulation where emulation models are computed from the first builds of wireless devices (prototypes) with physical layer functionality. In contrast to the existing power estimation methodologies for analog and digital circuits, the power emulation methodology introduced in this work does reflect the wireless device under development, under all realistic scenarios of interest. The new power emulation model takes the environmental, orientational and logical interface parameters as the carrier frequency, bandwidth and transmission power to compute the emulated power for each LTE sub-frame. The emulation system criteria of having some functional part of the emulation system performed by the target system is fulfilled in two ways:

- The emulation model is computed as a function of physical measurements conducted on the target modem platform;
- The inputs to the emulation system are to be extracted from the logical commands within the modem platform of the DUT.

Hence, in both ways linking the emulation system to the final target system.

During the transmission and reception operations of cellular devices, it is the electromagnetic waves that carry the information. Due to the fact that these devices, in most cases, are held on the ear during talk time, the interaction of the head and the electromagnetic field do cause heating effects in the head. This is the case, especially in the area around the ear as shown in Figure 1.3 or any body part in contact with the transmitting device. In the worst case, the overheating surpasses the thermoregulation process of the affected organs and body parts which can end with chronic health effects [23]. A quantity *SAR (Specific Absorption Rate)* was defined to quantify the rate at which energy is absorbed per unit of mass in an object exposed to an electromagnetic field [24]. It has been proven through experiments that a body exposed to an electromagnetic field producing a whole body SAR of 4 W/kg for 30 minutes, would have

a temperature increase of nearly 1^0C. The electromagnetic exposure to partial-body has been defined not to exceed a SAR of 1.6 W/kg averaged over 1g of tissue in the United States [25, 26] and 2 W/kg averaged over 10g of tissue in the European Union [1].

The RF signals used for wireless communication in the frequency range 300 MHz to several GHz at which significant local and nonuniform absorption occurs do belong to the non-ionizing class of radiation. Excessive exposure to these RF energy fields can be harmful [23]. Figure 1.3 shows the distribution of the electromagnetic radiation from a device attached to a head. The highest intensity is as expected on the area of contact between the transmitting device and the head.

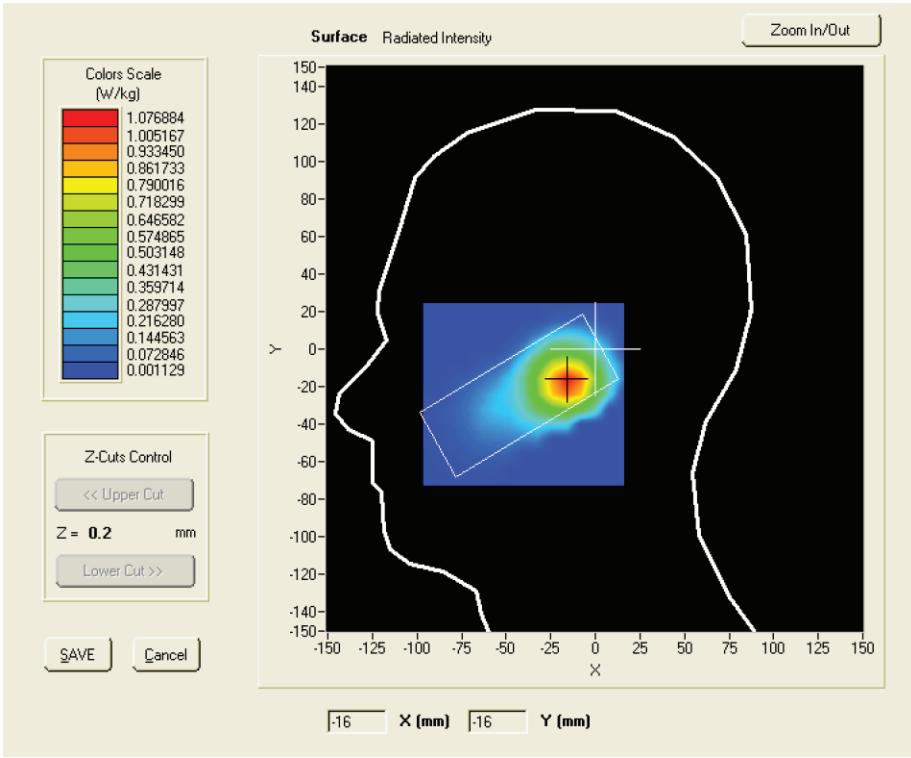

Figure 1.3: Visualization of SAR at in a cut-plane parallel to the surface of the phone device in cheek position. Taken from [27].

Given the significance of this fact, it is very vital to determine the SAR in the early phases of the design when there is still room for optimization. The SAR is dependent on the physical parameters of the final product (say a cell phone)

chasing and circuity making it very difficult to predict. However, the numerical approach for SAR simulation *finite-difference time-domain (FDTD)* [28–30] has proven to have a relative error of less than 10% given the dielectric properties of the final product. This is unfortunately short of the capability for emulating the SAR as a function of realistic scenarios. Moreover, for meeting a demand for an emulation system, some functional parts of the emulation system have to be carried out by the target system which cannot be achieved by the FDTD simulation approach. Thus, FDTD simulation can be performed earlier on, but they are not reliable before their validation against physical measurements. Consequently, we are in this work defining an emulation model that will be based on the earliest prototype sharing the same physical and dielectric properties as the final product.

1.0.1 Synopsis

The thesis is organized into introductory and overview chapters that introduce the concepts of the problematic of this research and reviews the status quo of the main concepts, RF architectures, power estimation/emulation and LTE technology. The results of the research work are presented in the subsequent chapters based on publications of this research. The overview of the chapters in this thesis:

- **Chapter 1** introduces the significance of estimating the power consumption of wireless modem chipsets during the design and development phase. The significance of estimating the SAR that can be absorbed while using the wireless devices containing these chipsets is also introduced.
- **Chapter 2** reviews the available architectures that can be used for transmitting the LTE signals and the LTE technology its self. The chapter also reviews the available methodologies for estimating the power consumption of electronic devices and the SAR concept along with ways of estimating and measuring it.
- **Chapter 3** presents the measurement approach applied in the research for measuring the power consumption of the RF subsystem when transmitting a LTE signal.
- **Chapter 4** examines multivariate modeling approaches for an approach that can model, with the highest accuracy, the 5-dimensional power consumption of the RF subsystem when transmitting an LTE signal.
- **Chapter 5** presents a new emulation methodology for the analog RF subsystem, focusing on the LTE transmitter.

- **Summary and Discussion** chapter sums up the motivation of this work, the conducted research, results and future research on this problem domain.
- **Appendix** contains the performances of the reviewed transmitters and details of the LTE technology.

Chapter 2

Overview

2.1 RF subsystem architecture overview

2.1.1 Introduction

The state of art and the evolution of the RF transmitters towards the LTE technology will be analyzed in this section. The RF transmitter architectures are to be scrutinized from their architectural design, power efficiency and integration level.

During the RF transmitter design, the choice of the RF architectures is contingent upon the desired *Peak to average power ratio (PAPR)*, bandwidth of both baseband and modulated RF signals, financial cost, *ACLR (Adjacent Channel leakage Ratio)*, *EVM (Error Vector Magnitude)* and area efficiency.

The RF transmitter modules are meant to mix, the data modulated baseband *In-phase Quadrature (IQ)* signals, with the carrier signal at the appropriate carrier frequency. These modules also do make the resultant signal compatible for the antenna for transmission. This is done through modulation, up-conversion and power amplification operations where the modulation and up-conversion operations are often combined. Moreover, the carrier signals referred to are

compatible with being transmitted through the air interface (e-UTRA *evolved UMTS Terrestrial Radio Access* for LTE) in a given frequency channel. The functional structure of a typical RF transmitter is showed in Figure 2.1.

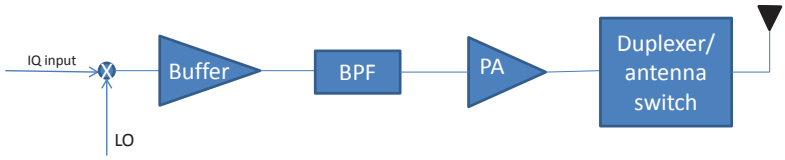

Figure 2.1: Typical RF topology.

The input signal is mixed with the carrier signal produced by the *local oscillator (LO)*. The RF signal, product of the input and the carrier signal is buffered to later be filtered by a *band pass filter (BPF)* to remove the harmonics and possible sidebands. The filtered signal is then amplified by the *power amplifier (PA)* to the specified signal levels. The amplified signal is sent to either the duplexer or antenna switch, according to the configuration used, that interfaces it to the antenna for transmission. Practically, RFIC's have both the duplexer and the antenna switch for *Frequency Division Duplex (FDD)* and *Time Division Duplex (TDD)* compatibility. There is though a 2-3dB and 0.5-1dB signal loss in the duplexer and antenna switch respectively [31]. Therefore, the antenna switch is most desirable in power conscious designs. The biggest drawback with the antenna switch is the coincidence of the TX and RX bands. The transmitter configuration with the duplexer should be desirable by cellular systems due to the fact that the TX and RX bands do not coincide with this configuration. In addition to the duplexer's power loss, this configuration also has a feed through problem between the transmitter and the receiver bands. The feed trough desensitizes the receiver and also raises the input noise of the receiver.

2.1.2 RF architectures

We have seen in the introduction section what are the influential parameters in the design of RF architectures. The RF architectures can be grouped into 2 categories; mixer based architectures and polar based architectures.

2.1.2.1 Mixer based architectures

Direct conversion:
This architecture based on direct conversion transmitter topology is much desired for its simplicity and high integration. The necessary number of external components desired is minimal, thus providing a low power consumption, small chip size and a low cost. The direct conversion transmitter architecture is depicted in Figure 2.2.

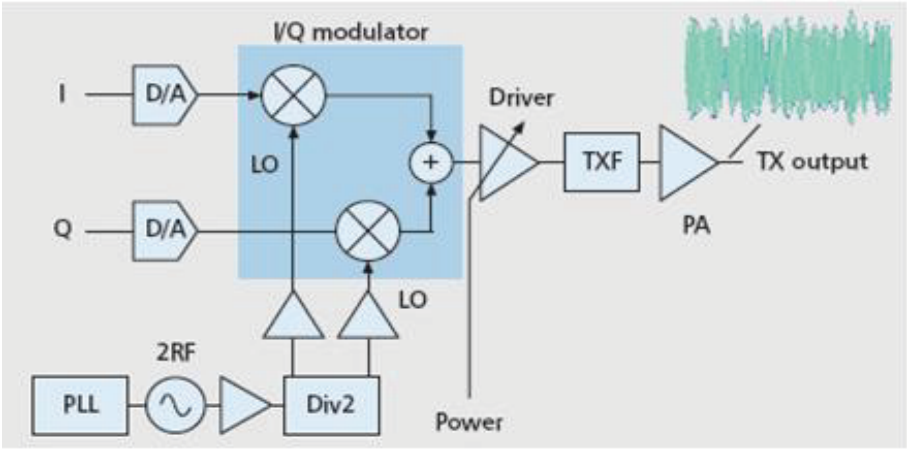

Figure 2.2: Direct up conversion topology (taken from [32]).

The direct conversion architecture (Figure 2.2) is characterized by 2 properties:

1. The output carrier frequency is equal to the *local oscillator (LO)* frequency;
2. Modulation and up conversion operations occur in the same circuit.

Though this architecture is largely desired for its simplicity, it does have a problem with the local oscillator distortion by the PA. This problem occurs when the output of the PA couples back to the oscillator. The oscillator tends to shift toward the frequency of this external stimulus because the PA output is a modulated waveform having a higher power and a spectrum centered around the frequency of the oscillator [31] . This phenomenon is referred to as injection pulling or injection locking. This problem can be alleviated if the spectrums of both the oscillators and the PA output are distant in the frequency-magnitude

domain. Here are 2 ways of circumventing this phenomenon by distantly separating the two spectrums :

1. Using offset local oscillators;
2. Using the 2 step architecture.

In Figure 2.3, we presented both the offset and two step architectures. In the offset architecture, the carrier signal is a mixture of 2 different oscillator frequencies. The resultant carrier signal after the filtering has a spectrum of the sum of the two frequencies of *VCO (Voltage Controlled Oscillator)* 1 and VCO 2. Thus, the carrier spectrum is far from the oscillator frequencies ω_1 and ω_2 as desired.

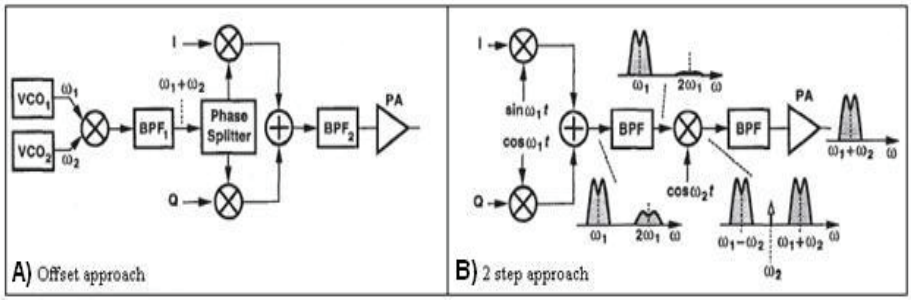

Figure 2.3: Offset and 2 step architectures (taken from [31]).

When using the two step approach to circumvent the PA output distortion problem, the carrier frequency is the sum of ω_1 and ω_2. The desired carrier frequency is obtained by up-converting the data signal two times. We can observe in Figure 2.3 that a band pass filter is utilized in both architectures to attenuate the harmonics and sidebands [31].

The inclusion of an extra VCO and band pass filters in 2.3 leads to more components hence an increased die size, a higher power consumption and cost.

Offset PLL (Phase Locked Loop) based architecture
This transmitter topology is best suited for systems using a constant geometric envelope modulation [33]. However, with same modifications, varying envelops can also be supported. This architecture was invented to meet the stringent GSM thermal noise specifications in the receiver band (see [31] for this topology and [33] for a GSM transceiver solution based on this topology). There are four

topologies of the offset PLL based architectures suiting different circumstances. These architectures are depicted in Figure 2.4 where the *PD(Phase Detector)*, *LPF(Low Pass Filter)* and VCO make-up the offset PLL.

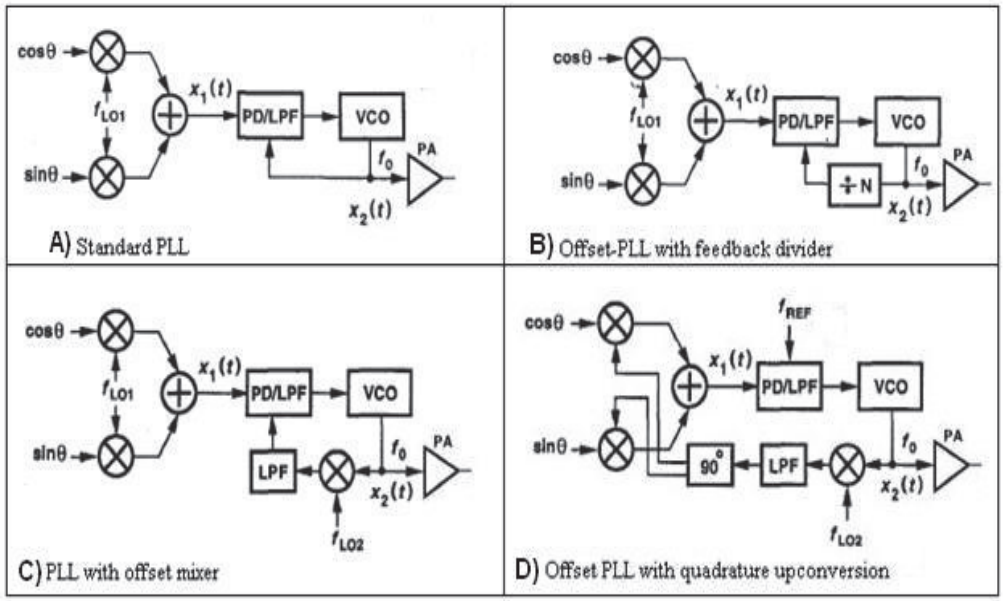

Figure 2.4: Offset PLL architecture designs (modified from [31]).

The standard PLL topology (Figure 2.4 (A)) is desired for its attenuation of VCO phase noise produced by other sources [31]. The PLL in this topology (A) operates as a narrow band filter centered on f_0, thus attenuating the out-of-band noise generated by the modulator. With an appropriate choice of the loop bandwidth, the phase information in $x_1(t)$ is directly transferred to x_2 while the output noise at large frequency offsets is determined by that of the VCO. It is however cumbersome [31] to operate the phase detector in the standard PLL (A) at high frequencies. For that case, a divider of factor N is inserted in the feedback loop to reduce the frequency accordingly. This topology is depicted in "PLL with feedback divider" in Figure 2.4 (B). The "finer" phase modulation requirement in $sin\theta$ and $cos\theta$ and the long settling times make this topology difficult to operate [31].

This brings to the justification of the "PLL with offset mixer" in Figure 2.4 (C) where an offset mixer driven by another oscillator is incorporated in order to lower the frequency presented to the phase detector. It is important to notice here that $sin\Theta$ and $cos\Theta$ are up converted to intermediate frequency signals

such that $f_{LO2} \pm f_{LO1} = f_0$. We could also choose to have the quadrature up-converter embedded inside the loop as shown in "offset PLL with quadrature up-conversion" in Figure 2.4 (D). This topology has a constant frequency, f_{REF}, hence minimizing the phase variation of $x_1(t)$ and hence modulating the phase of $x_2(t)$ according to the baseband waveforms.

LINC Transmitters:
The *LINC (Linear amplifier with Nonlinear Components)* transmitter architectures employ nonlinear components to form an efficient linear amplifier. The architecture depicted in Figure 2.5 is not commonly used in mobile devices due to the large number of components required.

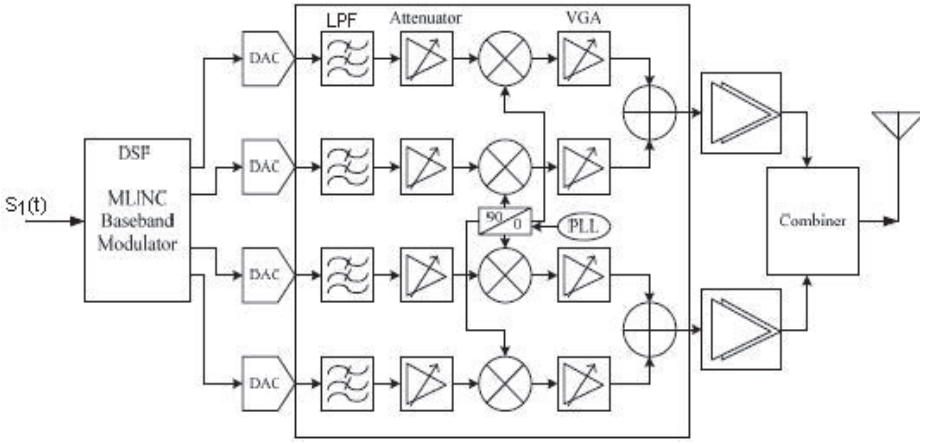

Figure 2.5: LINC architecture (modified from [34]).

The transmitter in Figure 2.5 is composed of a *DSP (Digital Signal Processor)* block and a Tx RF front-end was targeted for mobile *WiMAX (Worldwide Interoperability for Microwave Access)* applications [34]. The DSP block contains the *signal component separator (SCS)* which decomposes the incoming signal $S_1(t)$ into 2 constant amplitude signals whose rectangular representations $[I_1 Q_1 I_2 Q_2]$ are calculated and sent to the *digital to analog converters (DAC)*. The analog converted signals (rectangular representations) are low pass filtered, magnitude shaped and then mixed with the carrier signal. The mixed signals are amplified and then combined into a single RF signal. This architecture enables us to have nonlinear high efficiency PAs at a price of low integration and enlarged chip size. Compared with the direct conversion and polar transmitters, this architecture is impractical and highly costly.

2.1.2.2 Polar Based Transmitters

The polar architectures use the phase and magnitude information to form the complex transmitter signal in contrast to the mixer and PLL based architectures which employ rectangular modulation. Figure 2.6 depicts the concept of a polar transmitter where the *Phase Modulation (PM)* is differentiated (dt) into a frequency fed into the PLL. In Figure 2.7 a fractional-N PLL is used to apply the phase component. The amplitude component is applied by the PA.

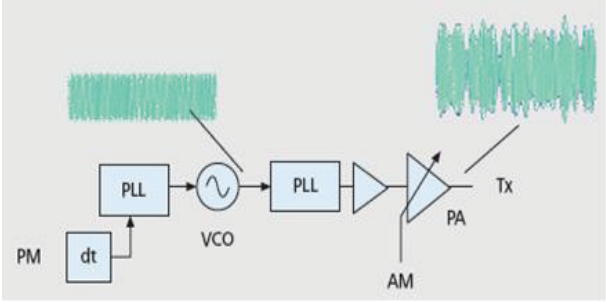

Figure 2.6: Polar transmitter (modified from [32]).

Notice the signals after the VCO and PA in Figure 2.6. The magnitude between the signals is meant to underline that it is the PA that does the amplitude modulation. Figure 2.7 depicts the polar transmitter where the fraction-N PLL is used to apply the phase component.

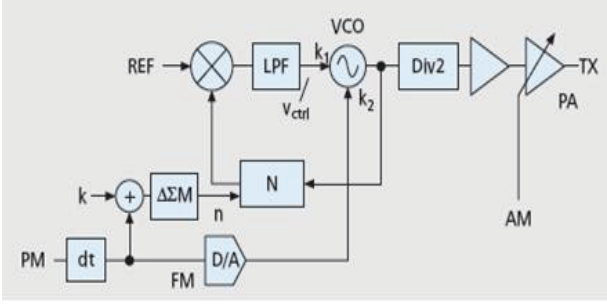

Figure 2.7: Polar transmitter with fractional-N PLL (modified from [32]).

The fractional-N PLL in 2.7 consists of the following components:

1. A phase/frequency detector (The *phase modulator (PM)* is differentiated

into the frequency used by the *Frequency Modulator(FM)*);

2. Loop filter;
3. VCO;
4. Feedback counter;
5. Delta-Sigma Modulator ($\Delta\Sigma M$) [35].

The PLL is used by the polar transmitter to apply phase modulation to the RF carrier.

There are two inputs to the polar transmitter, the phase modulation and the amplitude modulation. The amplitude modulation is fed directly to the PA that amplifies the carrier signal accordingly. This is very desirable for power consumption as it gives an opportunity of scaling the PA other than having a constant gain. On the other hand, the phase modulation is differentiated and converted to analog before being fed to the VCO. The possibility of varying the power levels of the PA suits LTE as this technology has varying geometric envelops. This architecture is however undesired due to its practical imperfections leading to spectral re-growth, increased *error vector magnitude (EVM)* and link performance loss [32]. These imperfections are scrutinized and illustrated in [20].

2.1.2.3 Evaluation of the architectures

The evaluation of the transmitter architectures is conducted in this section according to our perception. The architectural designs of the direct conversion, polar and LINC transmitters have been elaborated in the previous sections. In table A.3 where the power efficiency comparison between the 3 architectures targeted for WiMAX is presented, we can see that the direct conversion architecture has the least number of components required and the worst PA and system efficiency. The polar and LINC transmitters respectively require 50% and 100% more components than the direct upconversion transmitter. The polar transmitter has the best performance in terms of power efficiency. This efficiency can only be achieved if the strict matching, high sampling rate DAC and a good polar PA can be guaranteed.

In Table A.4 we present the overall architectural evaluation of the transmitter architectures based on the transmitter size, power consumption, system efficiency, PA efficiency and the complexity level. The polar transmitter (with offset loop including the PA) have the best performance but also the highest

complexity which makes it practically undisired. Practically, the most desirable design is the direct conversion architecture, as also preferred by most vendors and authors, due to its simplicity and a high level of integration. We have also seen the direct conversion architecture pulling problems and ways of mitigating them. The most efficient way of migrating this problem without increasing the component number dramatically is the generation of the LO signal with the frequency as twice as the channel frequency. This would merely require a divider in front of the mixers. Moreover, [36] states that the direct conversion transmitter is the de facto standard for both LTE and *WCDMA (Wideband Code Division Multiple Access.*

2.1.3 Current trends for LTE transmitters

Due to the fact that LTE is a relatively new technology, there have neither been produced nor published numerous transceivers as in comparison with its predecessor technologies as the WCDMA and WiMAX. The available WCDMA transceivers are mainly designed upon the homodyne and heterodyne architectures. A correlation between the chosen architecture and the used technology can be observed. The *Complementary Metal Oxide Semiconductor (CMOS)* technology [37], [38], [39] is used with the homodyne architectures as the *Silicon Germanium Bipolar CMOS (SiGe BiCMOS)* technology [40], [41], [42] is used with the heterodyne architecture. An intriguing factor of notice between the solutions of these two technologies is the die sizes. The CMOS solutions are 30% larger than their counterparts.

Performances of homodyne and heterodyne transmitters produced in both CMOS and SiGe BiCMOS for WCDMA are presented in tables A.1 and A.2 in the appendix. It can be observed that transmitters in both tables A.1 and A.2 do meet the WCDMA specifications. The parameters, cost and reproducibility are needed in order to make a conclusive distinction.

The technological and architectural trends of the CMOS and homodyne in WCMDA and WiMAX have been followed up to the LTE by the first vendors of the LTE transcievers. Infineon [43] and Altair Semiconductor [44] provided the first highly integrated LTE solutions of $5 \times 5mm^2$ and $4.4 \times 2.9mm^2$ respectively. Both these transmitters are produced in 130nm CMOS technology using the homodyne architecture. These are good solutions in terms of power as they are a technology node lower than the existing solutions for WCDMA (see appendix). The relationship between the technology nodes and the current consumption where the positive correlation between the technology nodes and the current consumption was demonstrated in [45].

2.1.4 Future trends

The review of the research in the RF transceivers reveals the desire of striving to extend the digital part of the RF transmitters as close as possible to the analog part of the RF transmitters and the antenna. This is much desired due to the significant development in *digital signal processing (DSP)* where IQ mismatches, phase noise and other RF imperfections [46] can be nearly perfectly compensated using DSP algorithms. This trend fits best with the CMOS technology as it is most compatible with digital signals. As mentioned earlier, as the homodyne architectures are developed in CMOS technology, this combination would yield highly integrated and low cost solutions. There are digital transmitters solutions in CMOS targeted for GSM and EDGE [47] [48]. These solutions were used in cellular phones though they had a reproducibility issue. If the lessons learnt from the mentioned solutions are taken up, we would definitely expect the digital trend to continue more into practice (as seen in [43] and [49]) towards the new technologies as the LTE. We have an emerging technology, in infant stages, called *Software defined radio (SDR)* [50], [51] which is intended to implement a broader range of capabilities through elements that are software configurable in the *micro-level communication objects (MCO)*. For the mean time, the conventional hardware defined radios are many factors cheaper and practical compared to the complicated SDRs. The US military is the driving force behind this technology. A *Software Communication Architecture (SCA)* that enables the integration of hardware and software components from different vendors into seamless products has been designed. For daily users, we could be able to have cellular phones that could operate with all commercial providers across the world. As the cellular phones emerged from the military, it can be hard to rule out that the SDRs might not be in public use within a decade or less.

2.1.5 Summary

We have seen the state of art of the RF transmitters, their corresponding technologies and evolution towards the LTE technology. The available LTE transmitter solutions [43], [49] and [44] are produced in 130nm CMOS technology using the direct conversion architecture though [49] also offers a polar solution. The CMOS technology is currently undesired because it needs lots of calibrations due to its high tolerance values. But it is understandable that the existing solutions choose this technology due to the low production cost.

Based on the review of the available RF transmitter solutions and publications, the most efficient, low cost and high integration transmitter solution for the LTE

would be the direct conversion architecture with a digital front end produced preferably in CMOS technology. In order to have a conclusive decision, an analytical analysis towards LTE, as in table A.3 for WiMAX, would be needed to support this observation.

The choice of the transmitter architecture and technology solution is also contingent on the performance of the corresponding receiver solutions as in practical terms, the transmitter and receiver do share the same RFIC.

In the next section, we are reviewing the LTE telecommunication technology which is the target technology of this work.

2.2 LTE Review

2.2.1 Introduction

The *LTE(Long Term Evolution)* technology is the next generation of cellular phone technology and is intended to reach high peak data rates of 100 Mbps down link and 50 Mbps uplink (Release 8), low latency, high radio efficiency, low cost and high mobility characteristics.

The cellular phone technology has grown rapidly as the demand for more advanced and sophisticated features increases. The cellular phones that were once solely used for vocal and text communication via *short message services (SMS)* have evolved into multimedia gadgets demanding data rates of broadband capacity for optimal operation. The LTE technology is a way forward towards cellular broadband data rates [52]. This review is based on LTE release 8 [52] and we will also peep at the features to expect in releases 9 and 10.

2.2.1.1 The LTE targets

The LTE technology is supposed to meet the following specifications:

- High performance;
  - A peak data rate of 100 Mbps and 50 Mbps in downlink and uplink respectively for *User Equipment (UE)* category 3. For UE category 5, 300 Mbps and 75Mbps for downlink and uplink respectively are expected;

  - 1Gps in downlink and 500Mbps in uplink for advanced LTE;
  - Faster cell edge performance;
  - Reduced *RAN(Radio Access Network)* latency for better user experience;
  - Improved spectrum efficiency (2 to 4 times compared to HSPA Release 6);
  - Scalable bandwidth of [20 15 10 5 3 1.4] MHz;
  - Improved broadcasting;
  - IP optimized (focuses on services in the packet switched domain).

- Backward compatibility;
  - Compatibility with the existing GSM/EDGE/UMTS systems;
  - Ability to utilize the existing 2G and 3G spectrum;
  - Support hand-over and roaming to the existing mobile networks.

- Wide application;
  - TDD (unpaired) and FDD (paired) spectrum modes;
  - Mobility up to 350kph;
  - Large range of terminals (phones and PCs to cameras).

2.2.2 The LTE structure

The relevant part of the LTE structure, LTE E-UTRAN architecture [53], for this work is presented in Figure 2.8. The extensive structure of the whole LTE system can be seen in Figure A.3 in the appendix.

- **User Equipment (UE)**
  The UE is the device used by the end user for communication. This is in most cases a hand held device in form of a cellular phone or a laptop. This device is equipped with a *Universal Subscriber Identity Model (USIM)* for its identification and authorization. LTE UEs in form of *USB (Universal Serial Bus)* dongles are now deployed around the world. We are interested in the performance of this device in terms of power consumption and the emitted electromagnetic energy produced during the transmission of the LTE signal to the eNB;

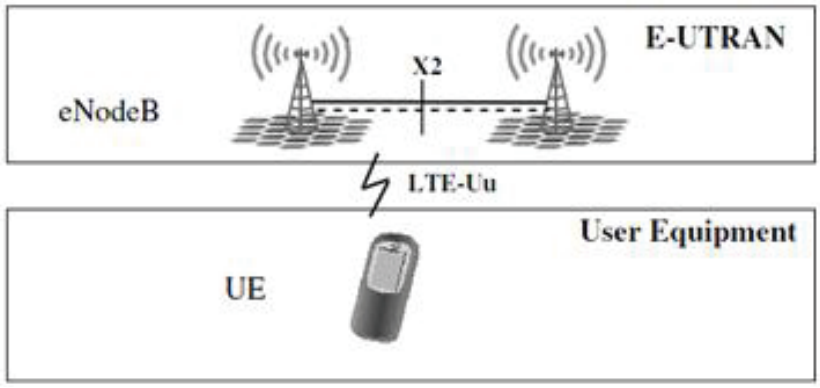

Figure 2.8: The LTE E-UTRAN structure made up of the UE and base station (eNB or eNodeB). This structure maintains the UE on the network via the radio link (LTE-Uu) (taken from [53]).

- **Evolved Base Station(eNB)**
  The eNB is the radio base-station that is in control of all radio related functions in the fixed part of the system. The functions of the eNB are listed below:
  - The eNB acts as a layer 2 bridge between the UE and the *Evolved-Packet Core (EPC)* by being the terminal point of all the radio protocols towards the UE and relaying data between the radio connection and the corresponding IP based connectivity towards EPC. In this role as the terminal point, the eNB performs ciphering/deciphering of the uplink data and also IP header compression/decompression;
  - The eNB also performs the following control plane functions;
    - Radio Resource Management which involves controlling the usage of the radio interface;
      - Allocating resources based on requests;
      - Prioritizing and scheduling traffic according to required Quality of Service;
      - Constant monitoring of the resource usage situation;
    - Mobility Management;
      - handovers;

  The eNB, as a static element with the UEs in its vicinity as the dynamic elements, is very influential on the amount of power and electromagnetic radiation used for transmission from the UEs. The UE power consumption/electromagnetic energy used to reach the eNB is (among other fac-

tors) a function of the distance and terrain from the UE to eNB. The eNB dictates the transmission power of the UE by sending ramp up/down messages whenever necessary.

For the relevance of transmitter power consumption and the emitted electromagnetic radiation, it is the air interface (in the uplink direction) in the E-utran structure that is of interest. In this technology, for any transmission to occur, there must be allocated resources in form of resource blocks as we will see in the LTE technology section. Resource blocks are two dimensional time-frequency elements of 7 $OFDMsymbols(0.5ms) \times$ 12 $subcarriers$. The LTE air interface defines a 10ms radio frame comprising of ten 1ms subframes of two 0.5ms slots. There can be 6 or 7 (control or data) symbols in a single slot depending on the used cyclic prefix(see OFDM transmission section). Hence, for power consumption and radiation measurements, the analysis of the contiguous $2 \times 0.5ms$ slots (subframes) would form a basis for the calculation of the power consumption and radiation emissions of the UE scenarios.

2.2.3 Emulation realization of the LTE structure

In this work, we wish to emulate the power consumption and the emitted electromagnetic energy during the transmission of the LTE signal. The goal is to be able to emulate these values very early in the design phase, when the first prototypes with physical layer functionality are available. At this stage, the prototypes are neither capable nor allowed to connect to an E-UTRAN network. Moreover, even if we are capable of connecting to the E-UTRAN network, measurements conducted would not be repeatable to due to the unpredictability of the air interface. Hence, we would have to emulate the E-UTRAN architecture in the laboratory environment. This would take a one-two cell protocol tester with LTE compatibility. The prototype would be connected to the protocol tester via the antenna port using a coaxial cable. When connected, the prototype is invoked to search for a cell until its connected to the protocol tester. We have in this work used the AT4 wireless and Anritsu MD8430A protocol testers.

2.2.4 The LTE technologies

The LTE evolution was motivated by the high data rate demand where a combination of radio resource effective methodologies of modulating and transporting data were applied.

The LTE technology is made up of 3 fundamental technologies:

1. The *Orthogonal Frequency Division Multiple Access (OFDMA)* used for downlink;
2. The *Single Carrier- Frequency Division Multiple Access (SC-FDMA)* used for uplink;
3. The *Multiple input Multiple output (MIMO)* used for both downlink and uplink.

2.2.4.1 The OFDMA

This section describes the OFDMA principles used in the LTE technology in the downlink direction.

Introduction: OFDMA is a technology that has evolved from *Frequency Division Multiplexing (FDM)* and *Orthogonal Frequency Division Multiplexing (OFDM)* with the inclusion of *Time Division Multiplex Access (TDMA)*principles. The FDM technology was the first multicarrier technology and it is widely used in the television transmitters. The main drawback of this technology was its spectral inefficiency due to the requirement of guard bands between the carriers as seen in Figure 2.9. Consequently, the OFDM technology was proposed which

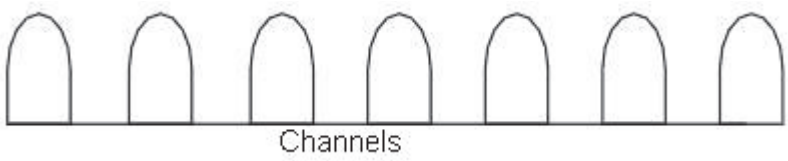

Figure 2.9: The FDM modulation requires guard bands between channels which makes it very spectrum inefficient.

was also based on the multi-carrier principles but eradicated the necessity of the guard bands by utilizing the orthogonal sub channels as shown in Figure 2.10.

Given the same resources as in Figure 2.9, we can observe the amount of spectrum that can be saved by using orthogonal sub-channels in Figure 2.10. The orthogonality is achieved by choosing the spacing between the sub-carriers such that at the sampling point of the individual sub-carriers, the other sub-carriers have 0 values. This feature is illustrated by Figure A.1 in the appendix. In Figure A.1, the spacing of 15KHz makes it possible to have all the other signals at 0 value at the sampling point of the desired one. The orthogonality of

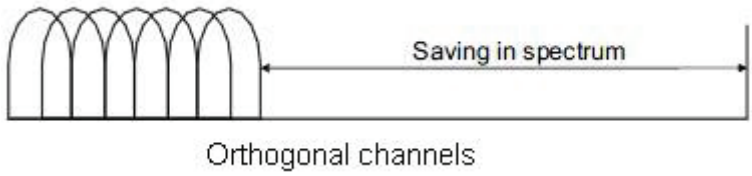

Figure 2.10: The OFDM modulation applying orthogonality to differentiate between channels. The orthogonality eliminates the use of guard bands yielding spectrum efficiency.

OFDM depends on the condition that the transmitter and receiver do operate with exactly the same frequency reference. The utilization of cheap components in UEs do make this problem severe as these oscillators do have large tolerances. The automatic frequency control in the UEs helps make sure that the frequency offsets never get out the bound set by the specification. Thus, the orthogonality in OFDM is still intact also given these impairments.

The OFDM technology solely allows a single user on a channel at any given time. For a system using OFDM modulation to accommodate multiple users on the same channel, TDMA has to be applied so that each user can have a share of the channel for a given TDMA slot. This is illustrated in Figure 2.11

Figure 2.11: OFDM employing TDMA to enable the sharing of channels between different users. Each user, represented by a colour, is allocated a slot on the channel.

The colors in Figure 2.11 represent the different users. Thus, each user occupies the channel for a given amount of time. This is very inefficient considering the possibility that the user might not need the full capacity of the channel in the

allocated time. In order to fully utilize the capacity of the channel, the diversification of the channel in time and frequency domain is applied. This results into the division of the channel; see Figure 2.13, where each column(channel) is divided among different users for a specified duration, hence increasing the capacity of the channel. This diversification of the OFDM channels into a frequency-time grid, is what is referred to as the OFDMA technology.

Thus, the 2 LTE technologies OFDM and OFDMA differ in principle that OFDM is a modulation scheme and OFDMA is the access scheme used to effectively diversify the resources (OFDM channels) among different users according to their bandwidth necessities.

In the LTE technology, in the downlink direction, the users are assigned resources in form of resource blocks comprising of 12 subcarriers over a duration of a half millisecond. Practically, the allocation resolution of 1ms is used in time domain.

OFDM transmission: Figure 2.12 depicts the OFDM transmitter where a serial bit stream of data in frequency domain is parallel transformed into the vector $\underline{\mathbf{S}}$ whose dimension spans the available number of subcarriers. Each element of the vector $\underline{\mathbf{S}}$ is individually modulated into the complex vector $\underline{\mathbf{X}}$ that is IFFT'ed to produce the time domain samples. Here, it is important to notice that $N \geq M$ as the IFFT demands a power of 2 inputs. Zero padding is used for $N - M$ samples. Due to the problems that might arise because of the Inter Symbol Interference (ISI) when the length of the channel is longer than anticipated, assurances must be provided to mitigate this. This assurance in the LTE technology is provided inform of cyclic prefices as shown between the IFFT and P/S in Figure 2.12.

The cyclic prefix principle implies the copying of a chunk (of specified length) of the ending of the symbol to the beginning of the symbol as illustrated in Figure 2.12 with the samples $[X_k[N-G]...X_k[N-1]]$ being appended the input of the P/S. The cyclic prefix has 2 possible lengths depending on the type used according to the 3GPP specification [52]. There is short and extended cyclic prefices of durations $4.7\mu s$ and $16.7\mu s$ respectively that can be applied. The type of cyclic prefix applied do affect the number of symbols in the 0.5ms slot. Here with the short cyclic prefix, we do have 7 symbols and 6 symbols with the extended cyclic prefix. Thus, we do have a data payload reduction when the extended cyclic prefix is used and it is therefore infrequently used. The trade off between using a short cyclic prefix with seven symbols is greater than the possible degradation from inter-symbol interference due to channel delay spread longer than the cyclic prefix. Thus, the extended cyclic prefix is seldom used. This does also gain power consumption and radiation minimization as we are able to send more information data with the short prefixes. The output of the

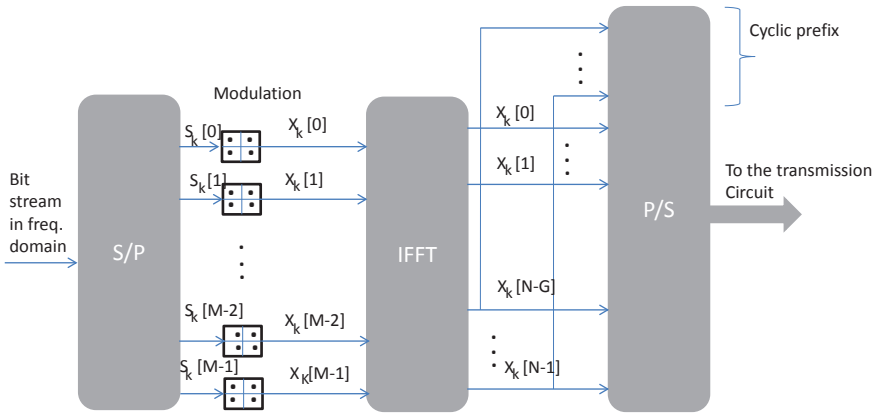

Figure 2.12: OFDM transmitter.

P/S in Figure 2.12 is analog converted for transmission. In the LTE technology, it is the eNB that does the operations depicted in 2.12 and transmits the output analog signal to the appropriate user equipment. For the transmission from the eNB to take place, resources have to be allocated inform of resource blocks as mentioned earlier. Thus, providing a group of subcarriers to a specific UE for a given period of time as depicted in Figure 2.13.

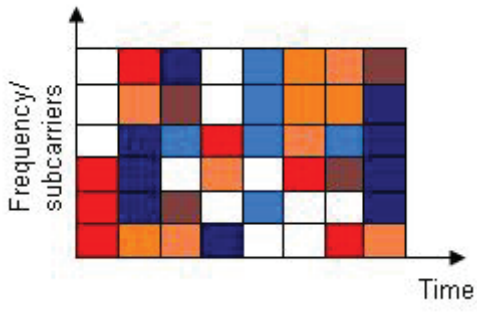

Figure 2.13: OFDMA allocation providing the possibility of allocations in both time and frequency domains.

2.2.4.2 SC-FDMA

In the uplink direction of the LTE system, the SC-FDMA technology is used in contrast to the OFDMA technology used in the downlink direction. The OFDMA would have been very practical to have in both directions. However, due to OFDMA's high requirement of *Peak-to-Average Power Ratio (PAPR)* and the demand for power efficient handheld devices, OFDMA is to be used in the base station where we do not have limited resources in terms of power. The SC-FDMA utilizes the desirable characteristics of the OFDM and the low PAPR of single-carrier transmission schemes to make an efficient LTE uplink. The OFDM characteristic of main interest here is the division of the transmission bandwidth into orthogonal parallel subcarriers where the orthogonality is achieved by:

- Employment of the cyclic prefixes that are longer than the channel delay spread;
- Synchronization of the received signal in time and frequency;
- Users occupying different sets of sub-carriers.

The SC-FDMA signals can be made in both time and frequency domains where the resultant SC-FDMA signals are equivalent. There is though a difference in the bandwidth efficiency where the time domain procedure is less bandwidth efficient due to the time domain filtering and filter ramp up/down time requirements. Let us start with the time domain implementation of the SC-FDMA shown in Figure 2.14.

The incoming bit stream is serial to parallel converted and then modulated by either QAM or QPSK modulation schemes. The modulated bits can be direct-sequence spread to spread the signal energy over a wider band but this is optional. The repetition block following the spreading is also optional. The QPSK or QAM modulated bits after the optional processing is translated to the desired frequency within the available bandwidth. This data is finally cyclic prefixed, pulse shaped and transmitted. The frequency domain generation of the SC-FDMA signal distributes the modulated signals to sub-carriers using the *Discrete Fourier Transform (DFT)*. This transmission scheme is depicted in Figure 2.15.

The frequency domain transmission scheme maps the QPSK/QAM modulated symbols into the subcarriers m by the DFT operation. The m subcarriers must be a factor of $2^n \times 2^k \times 5^l$ according to the specification. This was meant for the feasibility of the DFT. The subcarriers are then mapped to an N-IFFT

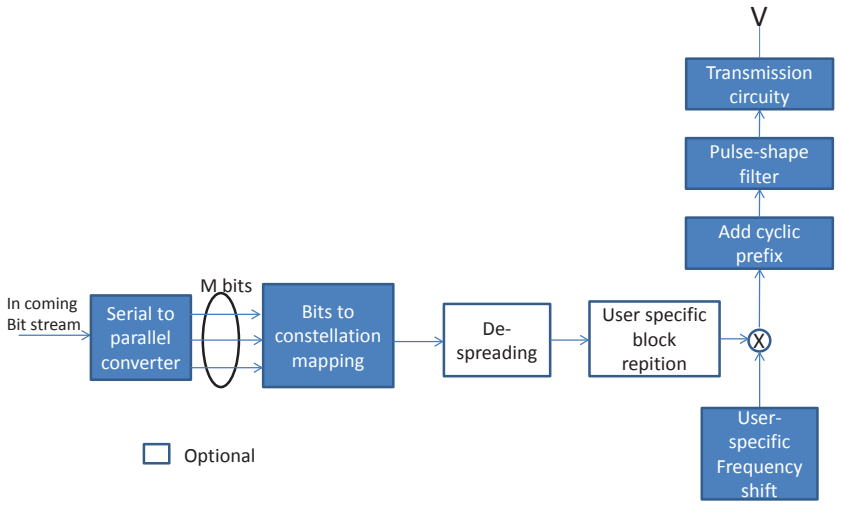

Figure 2.14: TDD (Time-Division Duplex) generation of of the SC-FDMA uplink signal.

and notice here that given the restrictions on both m and N, they are never equivalent. Thus, also in this case as in the OFDM, the non-used sub-carriers are zero padded.

2.2.4.3 Multiple Input Multiple Output

Multiple Input Multiple Output (MIMO) uses spatial multiplexing [55], beam forming [56] and pre-coding [57] principles where different TX's are sent from different antennas with different data streams in the transmitter at the same time. On the receiver side, the data streams are detected by signal processing means utilizing the propagation channel characteristics. To illustrate how the transmitted signals are detected in the receiver, let us assume that we have a 4×4 system depicted in Figure 2.16:

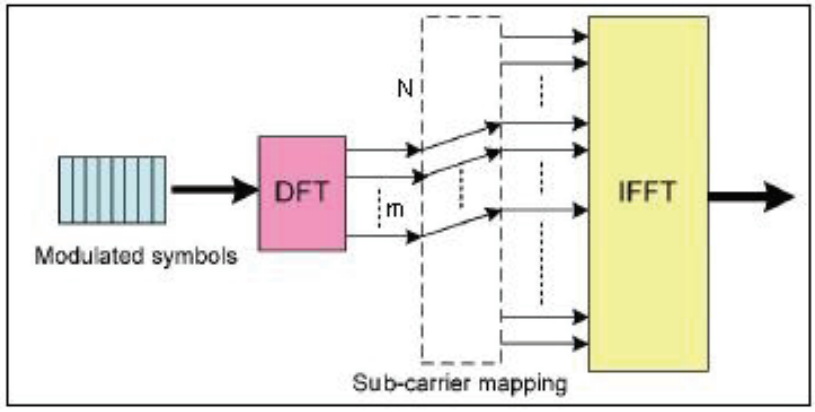

Figure 2.15: FDD generation of the SC-FDMA uplink signal (Taken from [54]).

Transmitters	Channels	Signal at the receiver
Tx_1	$h_{00}...h_{03}$	$Rx_1 = Tx_1 \times h_{00} + Tx_2 \times h_{10} + Tx_3 \times h_{20} + Tx_4 \times h_{30} + W_1$
Tx_2	$h_{10}...h_{13}$	$Rx_2 = Tx_1 \times h_{01} + Tx_2 \times h_{11} + Tx_3 \times h_{21} + Tx_4 \times h_{31} + W_2$
Tx_3	$h_{20}...h_{23}$	$Rx_3 = Tx_1 \times h_{02} + Tx_2 \times h_{12} + Tx_3 \times h_{22} + Tx_4 \times h_{32} + W_3$
Tx_4	$h_{30}...h_{33}$	$Rx_1 = Tx_1 \times h_{03} + Tx_2 \times h_{13} + Tx_3 \times h_{23} + Tx_4 \times h_{33} + W_4$

At the mobile terminal in Figure 2.16, we can see that we have 4 equations with 4 unknowns which can be mathematically solved. The noise ($W_1...W_4$) makes the detection process very difficult. However, by using the reference signals, the channel propagation can be estimated and the transmitted signals can be separated.

The application of this technology should in principle enhance the peak data rate by a factor 2 using a 2 by 2 antenna configuration or a factor 4 using a 4 by 4 antenna configuration. However, when you move to higher data rates by packing more data in the same amount of time, the bit error rate usually increases. This leads to a demand of higher coding rates. Thus, for the same amount of signal-noise-ratio, the information data rate increases slightly less than factor 2 or 4 for 2 by 2 and 4 by 4 respectively. The MIMO technology is

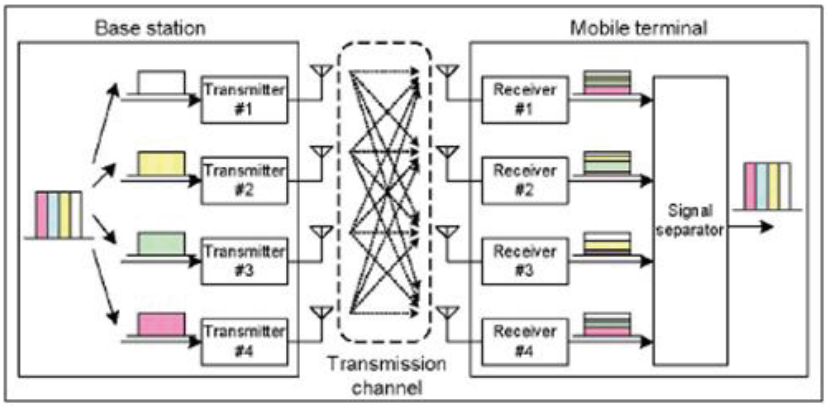

Figure 2.16: MIMO (taken from [54]).

illustrated in 2.16 where the transmit diversity principle can be observed as the same signal is sent from different transmitters in the base station and received on all receivers in the mobile terminal in order to exploit the gains from the independent fadings' between the antennas. The system in 2.16 is meant for illustration purpose as the number of antennas (per now in LTE release 8) in the UEs is set to 2 [58]. We can however have 2, 4 and 8 antennas at the eNB and [58] shows that the antenna array of 2×8 is the best inform of sector and edge throughput. This comes at a 50% increase in cost and complexity compared to the 2×2 configuration.

2.2.5 LTE future trends

LTE-A (release 10) is currently under definition. This release is supposed to provide downlink and uplink data peak rates of around 1 Gbps and 0.5 Gbps respectively with a spectrum efficiency of 30bps/Hz and 15bps/Hz in downlink and uplink. LTE-A will provide a 83% increase in spectrum efficiency compared to the LTE technology available on the market (release 8). The LTE-A is intended to utilize the carrier aggregation methodology to increase the available bandwidth to 100MHz. Moreover, the MIMO diversity is to be further exploited where there are plans to use the 4×4 and 8×8 MIMO configurations. With the anticipated backward compatibility between LTE/LTE-A, we can thus expect a LTE/LTE-A technology that meets the *IMT (International Mobile Telecommunication)* advanced 4G requirements before the end of this decade.

2.2.6 LTE structural and technological influence on radiation and power consumption

Having seen the structure and the technologies behind LTE in the previous sections, let us take a look at how the structure and technologies of the LTE would influence the emitted radiation and dispensed power. It is well known that the LTE technology was developed to meet the high data rate demand of the wireless handsets. LTE is targeted to provide 100Mbit/s and 50Mbit/s for downlink and uplink respectively for category 3 and slightly higher for category 5 as mentioned earlier. It is the radiation and power consumption during uplink transmission that is of interest here. Thus, watts consumed and w/Kg absorbed in a body per throughput bit.

In frequency domain, the OFDMA transmission consists of several parallel subcarriers where the time domain equivalent is a sum of these subcarriers (sinusoids). The geometrical envelop of the time domain waveform representation tends to vary strongly leading to a very high PAPR. The PAPR of this magnitude leads to a large back-off requirement in the design of the PAs and this is the reason that OFDMA is only to be used in basestations in the LTE technology. On the other hand, the usage of SC-FDMA in the uplink is a very good choice in terms of PAPR and PA efficiency as the resultant waveform of SC-FDMA behaves as a single sinusoid with low PAPR. Hence, a very good PA efficiency for the uplink which is very desired as UEs run on batteries. See Figure A.2 in the appendix which depicts the relationship between the geometric envelop and the PA back-off requirement. *Crest factor reduction (CRF)* schemes have been proposed as in [59] to reduce the OFDM PAPR though they have not been applied in the LTE yet.

The LTE technology "MIMO" and the signal processing techniques "beam forming" and "pre-processing" are very beneficial for power consumption and emitted radiation. With the MIMO technology, we do have a data rate increase of some factors depending on the MIMO configuration. Therefore, the necessary coding is also reduced as the different received signals are used to estimate the transmitted signal. Hence, the more data we are capable of transmitting in the same amount of time and power, the more power and radiation we are saving. However, the increased number of transmitters make the user more exposed to the electromagnetic energy. A beam forming technique which ensures directional transmission is also employed in LTE. With the directional transmission, the necessary transmission power can be reduced also yielding a reduced power consumption and emitted radiation.

In the telecommunication forecasts [60], it is fore-casted that a subscriber in a European country would have a daily traffic of 495Mb between 2010 and 2020.

This value does though not differentiate between uplink and downlink data. As we are interested in the uplink data and for that case the performance of UEs, it would be of best interest to get statistics of the ratio between the uplink and downlink in order to estimate the fraction of 495Mbits that is uplink. These statistics are rather very confidential for service providers and not easy to get. The daily uplink data usage for an average person would give an insight in the amount of power that can be saved by optimizing and reducing the necessary power per uplink bit. The proposed LTE advanced release 10 which among other methodologies is to utilize carrier aggregation to provide data rates of 1Gps in downlink and 500Mbps in uplink would sufficiently handle the projected daily user traffic of 495Mb with an anticipated lower power and emitted radiation per bit.

2.2.7 Summary

This preview has discussed the LTE structure, the applied technologies and the LTE's structural and technological influence on radiation and power consumption. We have seen the PAPR issue that rendered the LTE from having a technological (OFDMA) symmetry between uplink and downlink. Based on the projected data usage and the targeted data rates for LTE and LTE advanced technology, we can be certain that the technology will satisfy the data hungry users. An intriguing factor of curiosity is the efficiency of the LTE technology in terms of power (watts) and absorbed SAR per bit.

In the next section, the available power estimation methodologies are presented.

2.3 Power consumption estimation overview

Extensive work has been published on the estimation of power consumption at various levels of abstraction [7–10]. Figure 2.18 shows the levels of abstraction during the design of *SoC (System-on-Chip)* systems. We can observe that the amount of information increases by order of magnitude as the design maneuvers from system level to transistor level [11]. Consequently, the accuracy of power consumption estimation also increases as more knowledge is gained when the design transverses from the system level to the transistor level.

Approaches for power estimation at different levels of abstraction have been commercialized into power estimating tools [12–17]. The applicability of the PowerTheater [15], SpyGlass [13] and Cadance power estimation/emulation [12]

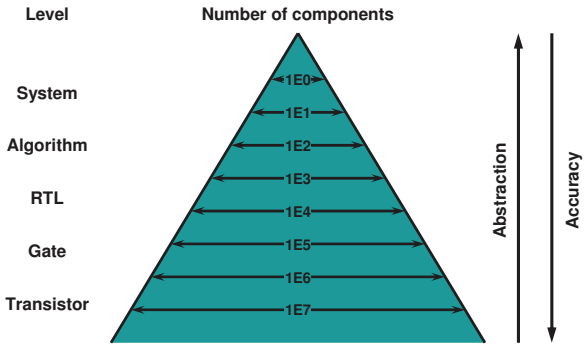

Figure 2.17: SOC design levels of abstraction (taken from [61]) showing that the abstraction decreases, as more knowledge is gained about the SOC. Thus, the power estimation approach after the transistor level presented in this work should be more accurate than the status quo approaches at the system, RTL and gate levels of abstraction.

tools was analyzed in a feasibility study conducted by Nokia [18]. These approaches are appropriate for digital circuits with discrete signals as they take the discrete transitions and technology libraries as inputs to estimate the power consumption of a given digital device.

Power estimation methodologies of analog circuits which are of interest in this work, have been defined at the system level of abstraction [19–22, 62]. These methodologies are based on the notion that the estimated power value is the power consumed by a functional block when given relevant input specifications, such as the target technology, without knowing the detailed implementation of the block. It is very difficult to achieve accurate power estimations at this level of design because all architectural decisions and relevant details as circuit implementations are not defined yet [20]. Power estimation of analog circuits is usually based on spreadsheets and experiences/expertise of system architects. In this way, relatively good power estimations can be produced because in most cases the new designs are based on old designs with minimal modifications.

Power estimation (status quo) of analog circuits at system level takes either an analytical or empirical methodology where a top-down or bottom-up approach is applied. However, the analog power estimators are always a blend of the two approaches with emphasis on one. In analytical methods, power consumption is modeled as a mathematical function derived from known schematics of the topol-

ogy of a component while in empirical methods measured power consumption is associated with each state/transtion of a component. The bottom-up and top-down approaches for developing power estimators for analog circuits [19, 20, 22]:

- The bottom-up approach, in analytical terms, requires a certain topology to be chosen from which exactly known schematic equations are derived, thereby modeling the behavioral model of the analog block. The requirement of the topology is a disadvantage for this approach as it is not the case in architectural system exploration. However, this increases the accuracy of the approach. In empirical terms [20], the power consumption of each component is measured or extracted from transistor level simulation for the different states. Here, parameters that influence the power consumption of the component for all operation states and transitions between two states are varied within their operational range and the power consumption per state computed/measured. This results into power consumption lookup tables for each operational state of each component. However, it is rather ambiguous on how measurements and transistor level simulations can be conducted at the system level of abstraction;

- The top-down approach suites the system level approaches better as no topology assumptions are required. Herein, the power behaviors of the complete system are modeled. However, this comes at a cost of the accuracy as the accuracy of models is difficult to achieve because of the typical nature of analog designs where one transistor can have a great impact on the behavior and specification of the design. Meanwhile, the use of fitting parameters typically compensates this constraint towards different topological implementations of the same analog block.

2.3.1 Analytical power consumption estimating methodology

The available analytical power estimators for analog power consumption take input specifications as target technologies to compute the power estimate of a functional block [19]. These estimators are constrained by two requirements [63]:

- Should only take high level block parameters as inputs in order to speed up the exploration of new designs;

- The accuracy of the estimation should be within a first order range.

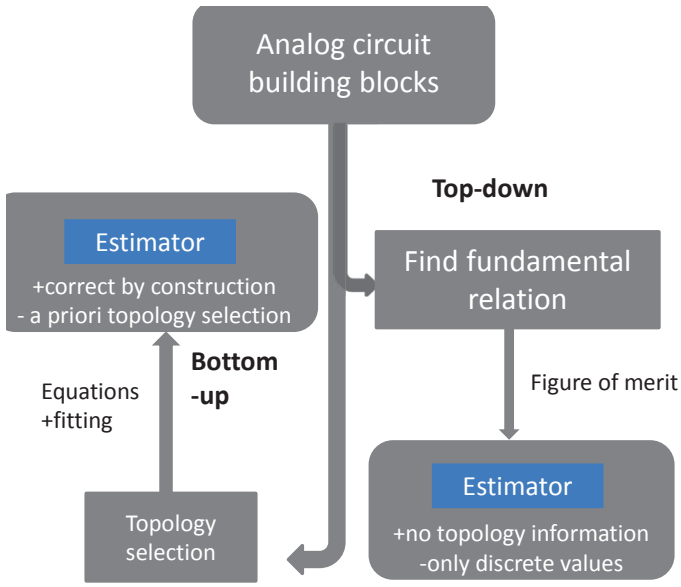

Figure 2.18: The top-down and bottom-up approaches for analog-power estimation and their corresponding attributes.

A blend of the bottom-up and top-down approaches was used to make a power estimator of an *Analog to Digital Converter (ADC)* made in *Complementary Metal-Oxide-Semiconductor (CMOS)* technology [19]. The development of this estimator based the emphasis on the top-down approach as the power estimator was derived from:

$$P = V_{dd} \cdot f \cdot Charge$$

where V_{dd} is the supply voltage and f the frequency. The high-speed ADC has two parts, the comparators and pre-processing circuity, which are clocked at $Fsample$ and the input signal frequency respectively. Therefore, the power P has to be split into comparator and processing circuit parts. We do have the charges stored on internal capacities, hence for both parts of the power estimator we do have:

$$P = V_{dd} \cdot freq \cdot (\text{Voltage}) \cdot C.$$

as the voltage swing for comparators is the full-supply voltage and approximately V_{dd} for the rest of the ADC circuity the power of each part of the ADC becomes:

$$P = V_{dd}^2 \cdot C \cdot freq.$$

To this point, the power estimator of the ADC has been based on the top-down approach. However, the capacitances are topology and technology dependent which is part of the bottom-up approach hence a blend of the two approaches to achieve the total power estimator:

$$P \propto V_{dd}^2 \cdot L_{min} \cdot (F_{sample} + F_{signal})$$

where the equality is replaced by the proportionality as the capacitance is taken proportional to the technology's minimal channel length L_{min}. The accuracy of the power estimator must also be included in the computation of the power estimator as the accuracy can be varied through the size of the device [64] where larger devices do produce higher accuracies at a cost of increased total capacitance leading to limited speed and increased power consumption. The accuracy *ENOB (effective number of bits)* is a function of *SNDR (signal-to-noise-and-distortion ratio)* defined as [65]:

$$ENOB = \frac{20 \cdot log(SNDR) - 1.76}{6.02}$$

The investigation based on a 75 data points for the correlation between accuracy, device size and power resulted in a regression relation [19]:

$$log\left(\frac{V_{dd}^2 \cdot L_{min} \cdot (F_{sample} + F_{signal})}{Power}\right) = -0.1525 \cdot ENOB + 4.8381$$

And thus, the final-power estimator valid for the complete class of CMOS Nyquist-rate high speed ADCs is [19]:

$$P = \left(\frac{V_{dd}^2 \cdot L_{min} \cdot (F_{sample} + F_{signal})}{10^{-0.1525 \cdot ENOB + 4.8381}}\right).$$

Power estimator models for each of the components in the analog signal chain of a transceiver were presented in [62] also using an analytical approach blending the top-down and bottom-up approaches. The practicality of the analytical approaches [19,62] can be questioned as they lack the validation against realistic scenarios. For an RF subsystem of interest in this work, it would be impractical to define an analytical model for each and every component. Thus, in this work we are proposing a methodology that considers the RF subsystem as a single component but to our knowledge, there is no analytical model that defines the power consumption of a RF subsystem.

2.3.2 Empirical power consumption estimating methodology

Empirical methods for modeling the power consumption of the analog circuits with the intent of power estimation and optimization are presented in [20,22]. In

the power estimation approach in [20], a state-based power estimation methodology at system level for integrated RF Front-ends is presented. Here, power state machines which are usually applied in power models of digital microelectronics were modified for analog components. The approach also follows the blend in the middle paradigm to compute the power models. In this approach, components are described by a power model made up of the *power (PSM)* and *functional (FUSM)* state machines, shown in Figure 2.19, which interact with each other.

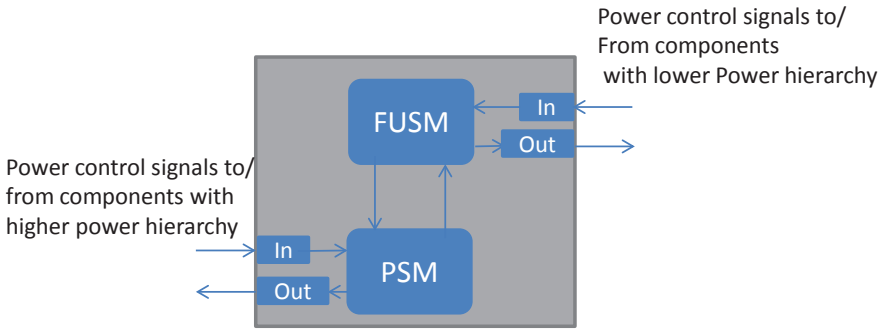

Figure 2.19: The system level power model of a component of an RF front-end is made up of PSM and FSUM state machines. The PSM models the power behavior of the component and the FSUM models power related control behaviors.

The PSM module is implemented by the power profiles, of the component of interest, obtained from the bottom-up approach. This module computes the estimated power of a component as a function of the power control signals, as OFF, Ready and ON, to/from components with higher power hierarchy and the power states from the FSUM module. The RF device is a passive device that operates on the control mechanisms or commands from the RF control or DigRF interface, hence, these mechanisms and commands are relevant for power consumption. The FSUM models these control mechanisms/commands which are regarded as the power states of the components with lower hierarchy. A case study of this approach was performed for a zero-IF receiver where it is stated that the operational states of a receiver are entirely determined by the baseband. Herein, the power commands from the baseband are sent to the PSM of the RF front-end's DigRF interface. The PSM of the DigRF interface controls the states of its corresponding FUSM. The FUSM of the DigRF interface is responsible for interchanging power commands with the PSM of the RF control hence the

RF control has a lower power hierarchy. This approach assigns a power value to each state of a component in a look-up table which would work perfectly fine given a limited number of states a component can find its self in and this approach could be applied at any level of abstraction of a design. However, the impracticality of this approach arises due to the size of the lookup table that will be required for technologies like the LTE. Here, you find parameters as Tx power, signal bandwidth and carrier frequency on the DigRF interface between the baseband and the RF device (subsystem) which would require thousands of elements in a look-up table. Thus, in this work, we do abstract away the state machines but do the characterization of a component as illustrated in the bottom-up approach. In order to avoid the complexity of mapping the power with the various states, we do a mathematical mapping that maps the low level parameters to the power consumption of the device. Thus, when given a combination of low level parameters, the estimated power would be a mathematical mapping between the model and the low level parameters.

Another empirical method based on neural networks for analog power modeling was presented in [22]. In this approach, power measurements are conducted for a specific analog component at various states and the power consumption is modeled with a continuous function obtained via a neural network. This continuous function is integrated into the analog component functional model so that the online instantaneous power consumption is computed during the functional simulation. The final power of the analog system is the summation of all the power consumptions of the individual components. Figure 2.20 shows the

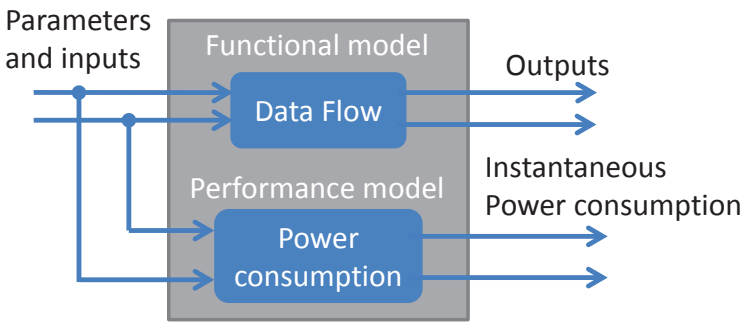

Figure 2.20: The analog component model optimized with a power consumption model.

analog component model optimized with a performance model for the power

consumption computation. This component model is capable of simultaneously performing a functional simulation alongside the instantaneous power estimation. This approach is the most viable approach for analog power estimation among the status quo approaches for estimating the power consumption of analog devices. However, the practicality of making an analog component model for each of the components in such a heterogeneous system as a RF subsystem seems not to be feasible. In this work, we are considering the RF subsystem as a single component whose mathematical model is evaluated mathematically without the need of making a functional model. In this approach, the online instantaneous power is achieved by sharing the inputs of the functional model. This makes the accuracy of the power estimation also dependent on the accuracy of the functional model. Since the RF subsystem is fully controlled by the baseband, we are in this work extracting the inputs of the RF subsystem power estimation model directly from the logical interface between the baseband and RF subsystem.

2.3.3 Power consumption emulation

In this work, we are focusing on power consumption estimation by means of emulation when the first builds of wireless devices (prototypes) with physical layer functionality become available. In contrast to the existing power estimation methodologies for analog circuits, this RF power consumption emulation methodology realistically reflects the wireless device under development, under all scenarios of interest.

Power emulation as a form of power estimation for digital circuits at the RTL level was introduced in [66, 67]. At the RTL level, design parameters as technology and topology are known. In this method, illustrated in Fig.3, each RTL component is characterized by a power coefficient C_x which describes the power (in watts) required to charge or discharge the component. These coefficients are given by the specific technology. The power emulated by the model in Fig.3 can be expressed by Equation 2.1 [66]

$$Power = \sum_{x=1}^{N} XOR(i_x, Q) \times C_x \tag{2.1}$$

where N is the number of inputs/outputs of the component of interest, i_x is the $x'th$ input/output of the component of interest, Q is the last clocked value of the flip-flop and C_x is the power coefficient of the $x'th$ transition.

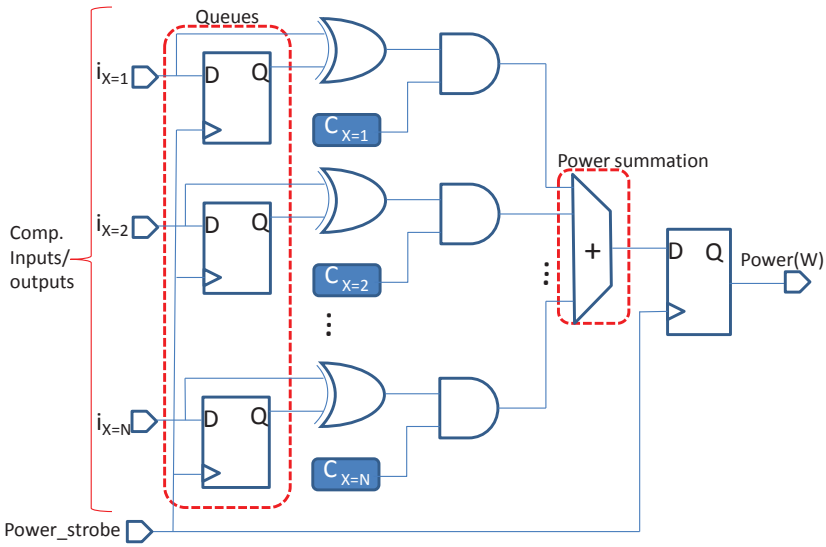

Figure 2.21: The power model used for power emulation of digital circuits at the RTL level of abstraction. For a component (RTL gate) of interest, i_x is the value of its input/output. The D and Q values of the flip-flops are the current and previous values of a component's input/output. For each clocking of the power_strobe, the D and Q values are XOR'ed and the product multiplied with the power coefficient C_x to produce the power consumption. The power(W) is the sum of all computed powers for each input/output of the component(s) [66].

To the best of our knowledge, no such emulation models exist for analog circuits. Power estimations for analog circuits have been defined at the system level of abstraction [19] and are based on the notion that the estimated power is the power consumed by a functional block under some specifications such as the specific technology, but without knowing the detailed implementation of the block. The new contributions of the work presented are at a lower level of abstraction, in Figure 2.18 at the transistor level when the device has been manufactured and a prototype with some minimal physical-layer functionality is available. Therefore, the estimation of power is more precise and reflects the actual hardware properties under various realistic scenarios of interest, for analog RF subsystems in a handset.

2.3.4 Summary

In summary, the state of art power estimation methodologies of the RF subsystem are at the system level of abstraction where there can be no link to the final product which can make the estimation very inaccurate. The available methodologies are based on analytical and empirical methodologies which apply the bottom-up or top-down approaches or a blend of the two. The analytical method would require a mathematical model or schematic equation for the RF subsystem which is not practical due to the homogeneousness of the RF subsystem. The empirical methods are going to be applied in this work, where the power consumption of the RF subsystem is associated to its states. The novelties related to the RF subsystem power emulation in this work are:

- The definition of the parameters affecting the power consumption of the RF subsystem and their online extraction during real life scenarios;
- Definition of the RF subsystem model at prototype level which reflects the final product;
- The computation of the instantaneous power during realistic scenarios;
- The reduction of the number of necessary measurements by up to 67%.

The concept of electromagnetic radiation and SAR that can be induced in a human body while using a wireless device is introduced in the next section.

2.4 Electromagnetic radiation

2.4.1 SAR and MPE

There are 2 accepted quantities, $SAR\left(\frac{W}{kg}\right)$ and $MPE\left(\frac{mW}{cm^2}\right)$, for measuring the electromagnetic radiation in order to ensure compliance with regulatory standards for maximum user exposure to non-ionizing electromagnetic fields in portable and mobile devices (see [1, 25] for all this section). Tables 2.1 and 2.2 show the enforced rates for SAR and MPE for general population in the United States:

The requirement to measure either of the 2 depends on classification of the wireless device:

Whole-body	Partial-body	Hands, Wrists Feet, Ankles
0.08	1.6	4.0

Table 2.1: SAR (taken from [1])

Frequency range f(MHz)	Power Density (mW/cm^2)	Averaging time(min)
300 - 1500	f/1500	30
1500 - 100.000	1.00	30

Table 2.2: MPE (taken from [1])

- SAR required devices;
  - Portable devices that are designed to be within 20cm of the body;
- MPE required devices:
  - Mobile devices that are mounted on vehicles;
  - And fixed devices as base-stations which are designed to not be carried on a body or being in a proximity of less than 20cm from a body.

MPE is computed as the function of the transmitter output power P_{out}, the antenna gain G and the distance R (in cm) from the body to the transmitter.

$$MPE = \frac{P_{out}G}{4\pi R^2} \quad [mW/cm^2] \tag{2.2}$$

The SAR is computed, in equation 2.3, from the electric field induced in a phantom of a given tissue conductivity and density:

$$SAR = \frac{\sigma E_{max}^2}{2\rho} \quad [W/kg] \tag{2.3}$$

where σ is the conductivity of the tissue-emulating material (in Siemens/m), E is the total RMS field strength (in Volts/m), and ρ is the mass density of tissue-emulating material (in kg/m3).

SAR simulations have proven to be very accurate [27, 68, 69] (see Table 2.3) since simulated SAR for some devices have been accepted by electromagnetic

Source	Frequency (MHZ)	Measured SAR (W/kg)	Simulated SAR (W/kg)	diff (%)
[68]	835	4.02	3.90	2.9
[68]	1900	1.48	1.47	0.7
[27]	1747.4	1.023	1.099	6.9

Table 2.3: Simulated Vs. measured SAR

exposure regulatory bodies [70]. However, SAR measurements are definitely still inevitable. The SAR measurements are conducted in tissue equivalent liquids using electric probes as illustrated below [24, 27]. The preliminary procedures include:

1. The dielectric properties of the tissue equivalent liquids are measured at a constant temperature;
2. A performance check is conducted using a setup where the generated signal comes from a dipole antenna;
3. The output power and frequency are controlled by a base-station simulator.

There are 2 defined recommended positions for the handset to be tested against the head phantom, the "cheek" and "tilt" position, as shown in Figure 2.22.

For each of these positions, a radio connection with the base-station emulator is established at maximum DUT power. The peak SAR averaged values are computed as a function of:

- SAR measured values on a grid of equidistant points on the exterior surface situated at constant distance from the inner phantom surface;
- SAR values recorded at equidistant points into a cube.

The SAR is measured for each operation mode at the channel that is closest to the center of the transmit frequency band. However, if the bandwidth of the transmission frequency band exceeds 1% of its center frequency, the lower and higher bounds of the transmit band should also be tested. For extreme cases when the transmission frequency band exceeds 10%, the number of channels to be tested is defined in [24].

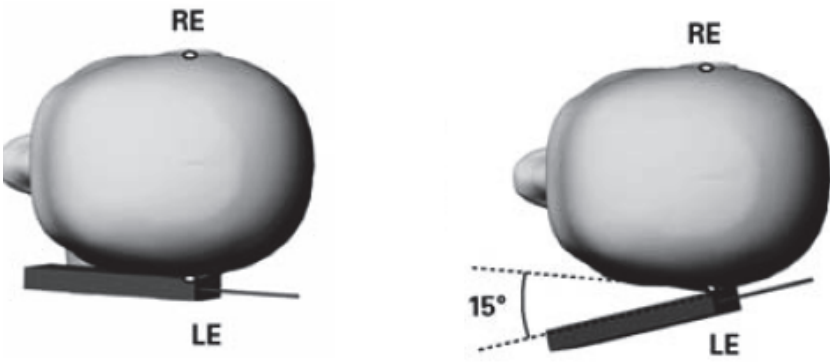

Figure 2.22: The handset is held with a robot arm at the, cheek and tilt, positions of the phantom head (taken from [27]) for the SAR measurements.

2.5 Summary

This chapter has presented an overview of the RF architectures applied in cellular devices and introduced the LTE technology and electromagnetic radiation. The available power estimation and emulation methodologies have also been presented. In the next chapter, the approach for measuring the power consumption of the RF subsystem is presented.

Chapter 3

RF subsystem power measurements

3.1 Introduction

During the design and production of wireless hand-held devices, it is very important to have an accurate methodology for measuring the physical power consumption. This enables the SW and HW designers to evaluate the power efficiency of the devices. And most importantly to make sure that the power consumption is within the defined target. However, the earlier (in the design phase when amendments can still be done) measurements can be obtained, the more useful they are to the designers. This section describes the benchmark for performing physical power consumption measurements on the RF subsystem of a wireless handset. This benchmark can be adapted to any module in a wireless device.

3.2 The power measurement Setup and procedure

This section describes the measurement setup and the procedures taken to perform the power measurements.

3.2.1 The Hardware

The configuration of the physical power consumption measurements setup is shown in Figure 3.1.
The setup is made up of the following components:

- Data acquisition device in form of the NI USB 6351;
- Work station with 2 SW tools;
  - The tracing tool from which Tx and RX operations are scheduled;
  - The data logging tool that interfaces to the data acquisition device;
- The resistor R [0.1Ω $5W$], that is inserted in the power supply line of the module of interest. The voltage difference over this resistor is used to calculate the power consumption of the module of interest;
- The trace box, that retrieves modem traces from the XTI port of the modem platform;
- The signal and spectrum analyzer connected to the antenna port of the DUT to measure the power of the outputted RF signal.

3.2.1.1 The configuration

A trace is cut on the power supply line of the RF subsystem and a 0.1Ω resistor inserted. A wire from each side of the resistor is connected to a measurement channel of the NI USB instrument which is connected to the work station via a USB port. The workstation is connected to the trace box via TCP/IP or USB. A XTI cable connects the trace box and DUT. The signal and spectrum analyzer is connected to the DUT by a coaxial cable. The triggering signal is routed from the modem platform GPIO *General Purpose Input Output* to NI USB and signal analyzer.

NI USB (mV)	Ampere meter (mA)	Calibrated R (Ω)	Div. %
9.3787	98.1	0.0956	4.4
103.599	104.1	0.0995	0.48
9.4	98.1	0.0958	4.17

Table 3.1: The calibration of the measurement resistor. The calibrated resistance is $R = V/I$ where the V is the voltage difference and I the current measured on the NI USB and ampere meter respectively.

3.2.2 Instruments calibration

The calibration validity of the signal analyzer, power supply and NI USB has to be verified by checking the calibration stickers. The resistor R has to be calibrated and the attenuation associated with the coaxial cable connecting the DUT and the signal analyzer has to be defined. The resistor is calibrated using the setup in Figure 3.2. An ampere-meter is inserted in the path of the current flow. Three measurements were conducted where the measured current and voltage difference and the calibrated resistance are tabulated in Table 3.1.

The maximum divergence from the factory resistance of 0.1Ω is 4.4% which is within the 10% tolerance of the resistor. The attenuation associated with the coaxial cable is measured by a power sensor and a signal generator in the following steps:

1. Generate an RF signal at frequency of interest at a reasonable power level;
2. Take 2 measurements, one when the power sensor is connected directly to the output of the signal generator and the other when the coaxial cable is connecting the power sensor and signal generator;
3. Compute the difference between the two measurements. The difference indicates the attenuation associated with the coaxial cable.

3.2.3 SW configuration

In order to guarantee synchronous measurements, a trigger is used to start the logging of power consumption and RF signal power. A triggering signal at the start of the Tx scheduling operation is assigned to a GPIO on the modem platform. This signal is connected to both the NI USB instrument and the signal analyzer. These instruments are configured to start logging when ever the trigger signal is high.

3.2.4 Measurement procedure

Preliminary procedures:

1. Warm up,
   The power supply and signal analyzer are required to be warm up for 30 minutes. The NI USB only requires 15 minutes thus, the measurement setup is left to warm for 30 minutes after power up;
2. Allow the phone to warm up by turning the transmitter to maximum power for 5 minutes. This is in correspondence with the warm-up used prior to conducting the TRP *(Total Radiated Power)* test [71].

The measurements:
The power consumption of the RF subsystem is measured through the following procedures:

1. Parameter selection,
   the GUI, Figure 3.3, is used to select the parameters of interest. The parameters of interest in this work are boxed in red. The Tx button is invoked to start a tx operation;
2. Data acquisitions
   the triggering signal initiates the logging of the RF signal power (Tx power) and power consumption. Both the signal analyzer and Labview are set to average over 1000 subframes (1000 milliseconds).

However, this procedure is applicable for a limited number of measurements due to the work load associated with conducting these measurements. In case of a full characterization, an automated approach is applied. This setup is shown in Figure 3.4 where:

- The chamber control engine provides access and ability to set the chamber to the desired ambient temperatures, the chamber returns the time to when the desired temperature is reached;
- In the desired ambient temperature, phocom provides access to the DUT where commands can be sent to the UE, and for commands where power consumption is desired;
  1. The FSV control allows the reading and reporting of the signal characteristics at the antenna port;
  2. The NI executable is called for measuring the power when desired.

3.2.5 Power consumption uncertainty/precision

The measurement system is affected by the systematic and random errors arising during the measurement process [72]. The systematic errors are referred to as measurement/instrumental uncertainties and are provided in the manufacturer's specifications for the devices in Figure 3.1 as:

- Voltage supply device (0.05% + 10mV) [73];
- Measurement resistors (10% and 1%);
- NI USB 6351 (reading × gain error + 10 × offset error + noise uncertainty) [74];
- Signal analyzer (0.39dB) [75].

The instrumental uncertainties above are modeled using intervals [76]. The resultant RF subsystem power consumption is thus represented in form of intervals specified by lower and higher bounds:

$$[\underline{P}\ \overline{P}] = [\underline{V}\ \overline{V}] \times [\underline{V_d}\ \overline{V_d}] \times [\frac{1}{\overline{R}}\ \frac{1}{\underline{R}}] \tag{3.1}$$

where V is the voltage of the source, V_d the voltage measured across the resistor R and the underlines and overlines as in $\underline{V}\&\overline{V}$ indicate the lower and higher bounds of the variable V.

The random errors caused by unpredictable variations in the measurement system are eliminated by having the same starting point (trigger) of the measurements and averaging over 1000 subframes for each power consumption measurement.

In practical terms, the system and random errors impact the spread known in statistics and referred to as the precision/uncertainty in this work. The theoretical explanation of precision/uncertainty is depicted in Figure 3.5.

Due to the fact that the calculated precisions do not take into account the physical environmental variables as the ambient and junction temperatures which do have an effect on the measurement process, these precisions may not reflect the reality of the measurement process. Consequently, the DUT was invoked to transmit 100 LTE sub-frames 1000 times using a 20 MHz bandwidth at a 23 dBm transmission power. This was conducted for ambient temperatures of -10^0C, 22^0C and 55^0C. The histograms, shown in Figure 3.5, for each of the ambient temperatures represent the spread or precision to be expected at the respective ambient temperatures.

3.2.6 Evaluation of the measurement system and methodology

In order to verify the measurement methodology, three independent data sets of the RF subsystem power consumption measurements with the same operational parameters (bandwidth, modulation and carrier frequency) as a function of Tx power where conducted. Each set of measurements created a buffer zone or offset whose offset parameter corresponds to the absolute value of the measurement uncertainties as shown in Figure 3.6 (only last box is shown here). Given the three buffer zones, of independent measurement uncertainties in Figure 3.6, we do have a union and an intersection of the measurements. The Hausdorff distance [77] is used verify how the two sets (union and intersection) differ from each other. The Hausdorff distance measures the similarity of two non-empty compact sets in respect to their position in the metric space. This distance indicates the extent to which each point in the union set is located relative to the points in the intersection set [77]. For a perfect match between measurements, the Hausdorff distance is 0 which would only occur in an ideal setup.

The Hausdorff distance

$$d_{\mathrm{H}}(\cup_{I^n_{j=1}}, \cap_{I^n_{j=1}}) = \max\{ \sup_{x\in\cup} \inf_{y\in\cap} d(x,y), \sup_{y\in\cap} \inf_{x\in\cup} d(x,y) \},$$

where sup is the supremum and inf the infimum, between the intersection $\cap$ and union $\cup$ of the measurement uncertainty boxes is depicted in Figure 3.6. The Hausdorff distance is the length of the straight line segment joining the union and intersection interval boxes at the top right of Figure 3.6 and is found to be 0.31. The value is acceptable for our purposes but can be reduced in several ways. The simplest and least expensive is to replace the resistor in Figure 3.1 by one with tighter tolerance.

3.3 Summary

This chapter has presented the measurement approach applied in the research for measuring the power consumption of the RF subsystem when transmitting a LTE signal. The precision/uncertainty in the measurement system has also been presented at a room and extreme temperatures. The next chapter analyzes approaches for modeling the power consumption of the RF subsystem.

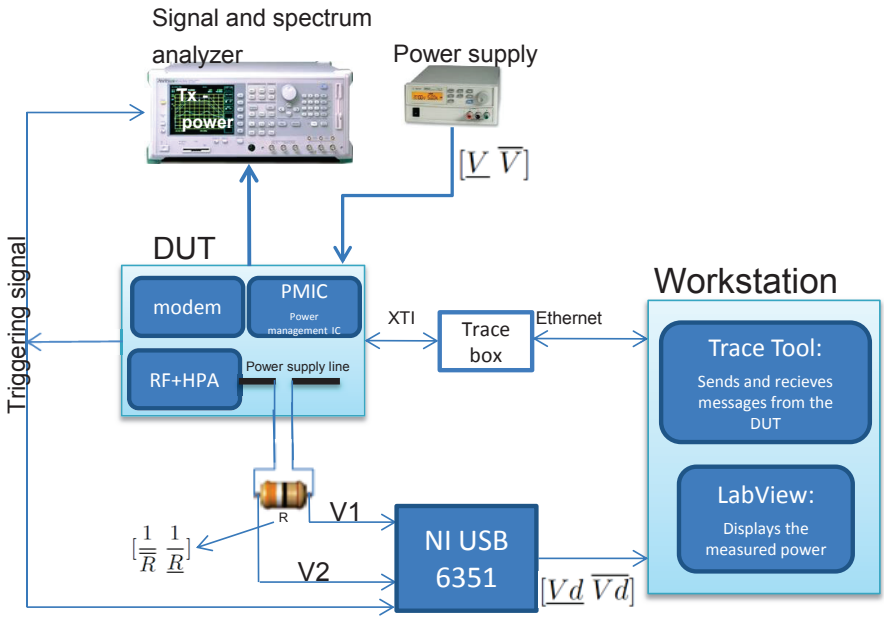

Figure 3.1: Power measurement setup used for the measurements in this work. The workstation forces the DUT into a specific mode of operation. During the operation, the DUT power consumption is measured by NI USB and displayed in LabView. The signal analyzer measures the output Tx power at the antenna port.

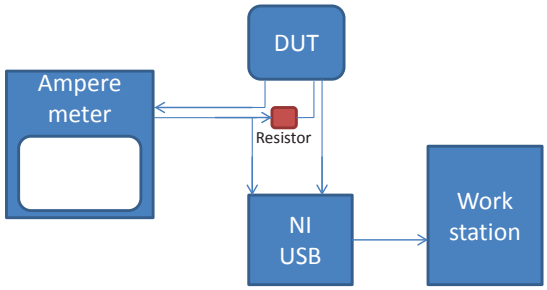

Figure 3.2: The setup used for the calibration of the measurement resistor. The ampere meter measures the current drawn and the NI USB measures the voltage.

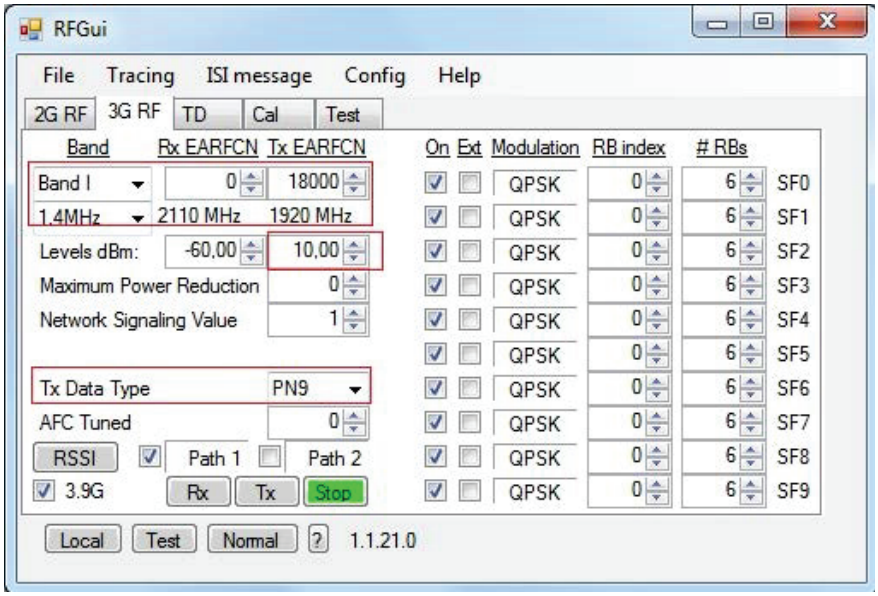

Figure 3.3: The interface "RF GUI" from which the desired RF subsystem - baseband logical interface parameters are selected. When the Tx button is invoked, the DUT continuously transmits a signal generated using the selected logical interface parameters.

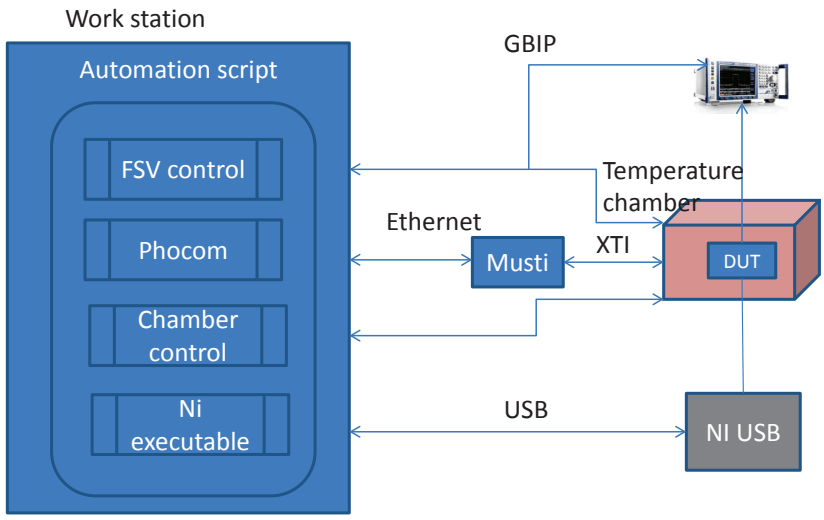

Figure 3.4: The setup for automated power measurements. The FSV, DUT, temperature chamber and NI USB are controlled from the work station.

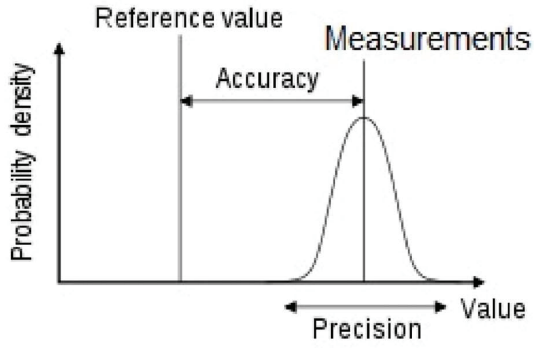

Figure 3.5: The precision in the measurement process.

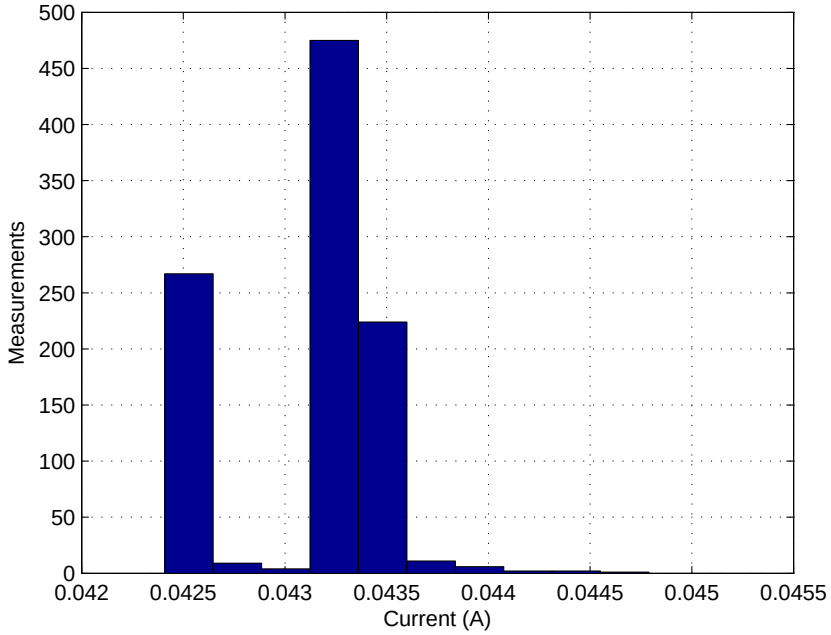

(a) The distribution of the power consumption at the ambient temperature of -10^0C.

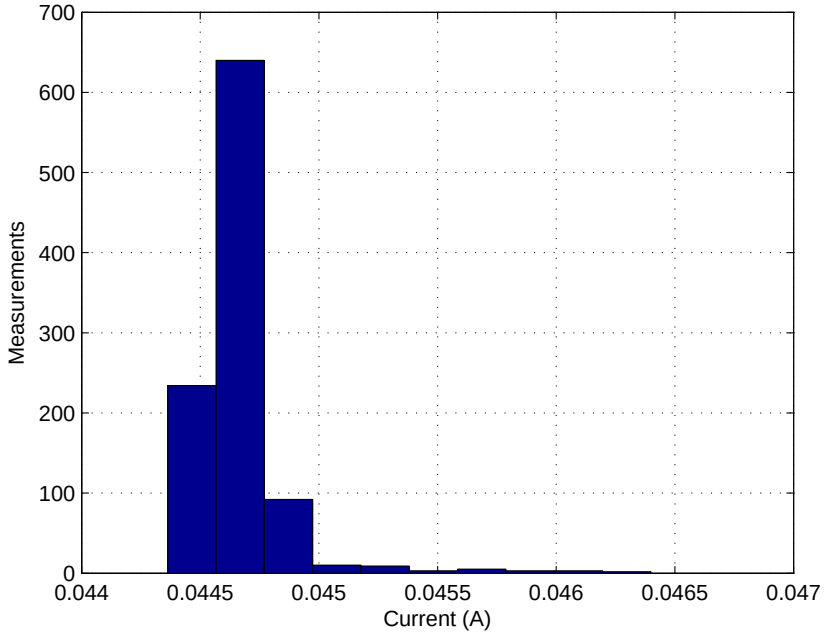

(b) The distribution of the power consumption at the ambient temperature of 22^0C (laboratory temperature).

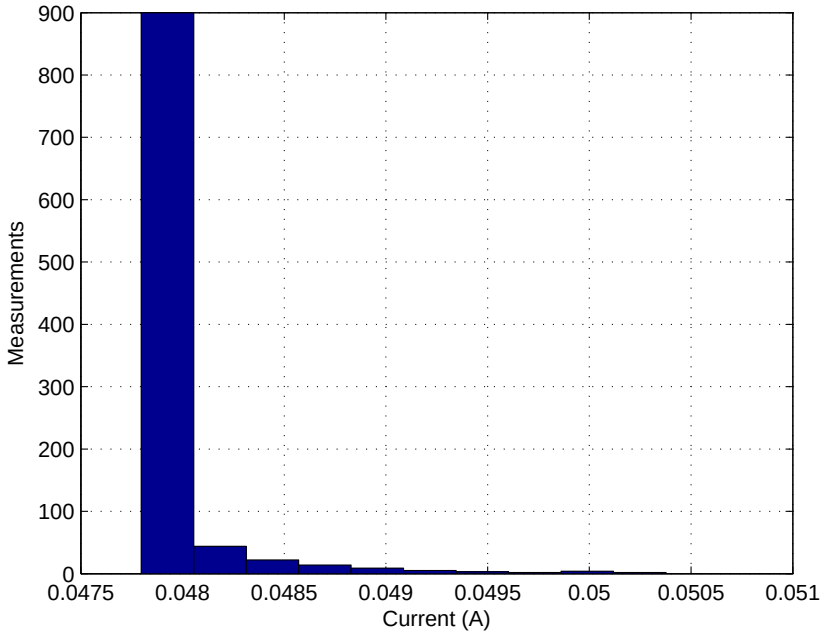

,

(c) The distribution of the power consumption at the ambient temperature of 55^0C.

Figure 3.5: The distributions of power consumption at ambient temperatures of -10^0C, 22^0C and 55^0C. The precisions, in terms of relative differences, for each of the ambient temperatures are 5.5%, 4.5% and 5.4% respectively.

,

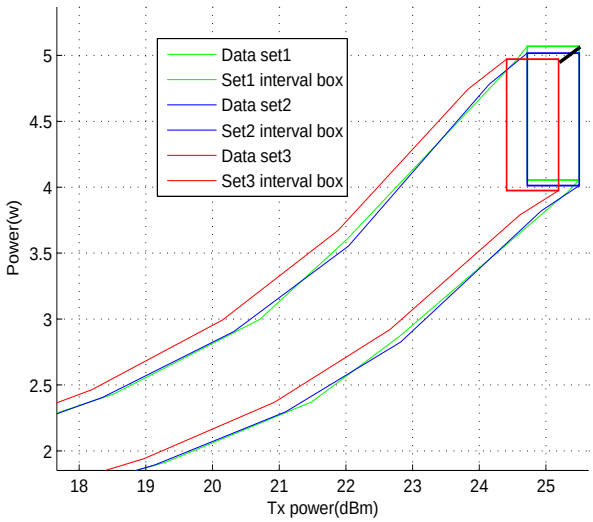

Figure 3.6: The buffer zones of three independent measurements used to calculate the Hausdorff distance.

Chapter 4

LTE RF subsystem power consumption modeling

4.1 Introduction

A power consumption analysis of a smartphone [4], the Openmoko Neo Freerunner, showed that the GSM modem consumes 80.6% of the total smartphone power consumption (excluding the blacklight) for a GSM phone call. In this work, transmission mode power measurements on a LTE (Long Term Evolution) modem have shown that the RF subsystem, in the worst case, consumes 68% of the total smart phone power.

Consequently, the estimation of the RF subsystem power consumption before the mass production of wireless devices is absolutely vital. We presented an approach for estimating the power consumption of the RF subsystem by the means of emulation with a precision of 11% for a specific scenario [78]. The emulation model in this approach only took the logical interface parameter (between the baseband and RF subsystem), Tx power, into account. It has been proven in this work, through power measurements, that other logical interface parameters (bandwidth and carrier frequency) and a physical environmental parameter (temperature) also do have an impact on power consumption (see Table 4.1).

Therefore, in this work, a new RF subsystem mathematical model that models the power consumption for all possible scenarios at any ambient temperature between -10^0C and 55^0C is presented. The possible scenarios are combinations of the logical interface parameter values. The main originality in this work is the extension of the previous power emulation methodology [78] from two-dimensional space (one variable: Tx power) to fifth-dimensional space (logical interface parameters and temperature) keeping the uncertainty of the power emulation within the uncertainty of the validation measurements.

4.2 Overview

4.2.1 RF subsystem power consumption emulation

A RF subsystem power consumption emulation methodology has been presented in our published work [78] for a specific scenario where only a single RF subsystem power consumption affecting parameter (Tx power) was considered. The methodology retrieves the logical interface parameters between the *DBB (Digital Baseband)* and the RF subsystem from the *XTI (X/Open Transport Interface))* port of the modem platform. The emulation model was computed as a polynomial interpolation using polynomial basis functions. This work analyzes modeling approaches towards the most optimal approach capable of modeling the RF subsystem power consumption as a function of all the relevant high level and physical environmental parameters.

The *FLPA (Functional Level Power Analysis)* methodology was presented [79–81] for modeling the power consumption of the *Systems-On-Chip (SoC)*. The FLPA methodology consists of four steps:

1. A primary functional analysis describing the system as a grey box with high-level parameters having an effective impact on power consumption;

2. The device power profiling step, where power measurements are conducted for the entire range of the defined parameters in order to determine the extent of the influence of the parameters on power consumption. This provides the basis for the definition of the power relevant parameters. However, instead of conducting power measurements for the entire ranges of the defined parameters, in this work, we choose to define the lower and higher bounds of these parameters in terms of power consumption. The influence of each parameters is computed as the relative difference of the power consumption as a function of the parameters' higher and lower

bounds. This is much more effective than conducting measurements for the entire ranges of the defined parameters;

3. The modeling of power consumption as a function of the relevant parameters;
4. And finally the determination of the accuracy of the model.

The FLPA approach is adopted in this work for finding the power consumption model of the RF subsystem. In this work, we are not only considering the high-level parameters but also a physical environmental variable (temperature). The four steps of the FLPA approach are analyzed with respect to the RF subsystem power consumption in the following sections.

4.3 FLPA analysis of the RF subsystem

In this section, we are applying a modified version of the FLPA analysis for finding the most optimal approach for modeling the power consumption of the RF subsystem while transmitting a LTE signal.

4.3.1 Primary Functional Analysis

The primary functional analysis of the RF subsystem as a grey box with high-level parameters having an effective impact on power consumption was conducted and published in our previous work [78]. The major power consumptions of wireless devices are largely functions of sequences of protocol/logical activities [78, 82, 83]. Hence, the power consumption of the RF subsystem is a function of the logical interface parameters between the RF subsystem and the DBB. However, the physical environmental parameter, temperature, do also affect the performance of the circuits and their effect is also investigated in this work. Heat emissions and temperature control on an electronic devices is known to be highly correlated to power consumption [84]. The defined extreme temperature conditions -10^0 C and $+55^0$ C for the LTE technology [85] are considered in this work. The logical interface [86] parameters from the LTE technological point of view are:

- Signal bandwidth $\in \{1.4, 3, 5, 10, 15, 20\}$MHz;
- Modulation schemes *QPSK (Quadrature Phase Shift Keying)*, 16 and 64 *QAM (Quadrature amplitude modulation)*;

- TX power $\in [-40, 23]$ dBm;
- Carrier frequency (depends on the supported LTE bands).

The RF subsystem power consumption is also dependent on the circumstances surrounding the near-field of the DUT (Device Under Test). Any near-field setup would have a different impedance between the antenna and PA (Power Amplifier) [87]. Each impedance is associated with a different reflection coefficient [88] and thus also a corresponding power consumption. In this work, the transmitter is terminated in a $50\,\Omega$ load. The effect of the near-field on the power consumption of the RF subsystem is to be investigated in our proceeding work.

4.3.2 Device power profiling

In our previous work [80], it was proven that the power consumption of an LTE RF subsystem is technologically dependent on the carrier frequency, signal bandwidth and transmission power (Tx power). For a comprehensive evaluation, we are also evaluating the influence of the ambient temperature. Thus, for the power profiling of the RF subsystem, the individual influence for each of the technological high level and environmental parameters on the power consumption of the RF subsystem is examined in this section.

For carrier frequency, a single band (LTE band 7) covering 2500-2570 MHz was considered. Our analysis of the carrier frequency is focused on the channel edges which are defined as the lowest and highest frequencies of the carrier separated by the channel bandwidth as in $FC \pm \frac{BWChannel}{2}$ where $FC \in \{2500\ 2570\}$ MHz and $BWChannel = 20$ MHz [85].

We are not evaluating the power consumption for the full ranges of the defined power affecting parameters as indicated in the FLPA approach. It is more efficient to define the lower and higher bounds of the parameters in power consumption terms, as shown in Table 4.1, and analyze the influence of the parameters in terms of the relative difference taken between the power at the lower and higher bounds.

The lower and higher bounds of the carrier frequency do attract scrutiny. For the LTE bands used in this work, numerically the lower and higher bounds would be 2510 MHz and 2560 MHz. However, practically the lower and higher bounds depend on the tuning of the modules in the RF subsystem. Therefore, for an appropriate definition of the carrier frequency bounds, the evaluation of the power consumption within the bandwidth of each band is necessary. This

Parameter	Lower bound	Higher bound
Carrier Frequency	2560MHz	2510 MHz
Bandwidth (BW)	1.4 MHz	20 MHz
Tx power	-40	23
Temperature (ambient)	-10^0 C	55^0 C

Table 4.1: Parameters lower and higher bounds

is accomplished by sweeping through each band with 1.4 MHz bandwidth as depicted in Figure 4.1 for bands 7 and 3.

The fact that the consumed power has such a non-monotonic behavior as a function of the transmitted power precludes using the transmitted power as homotopy parameter in convex homotopies (such as linear homotopies).

The device power profiling assessment is achieved through the following three steps:

1. Measurements when the four high level parameters and the ambient temperature are set to their respective lower bound values (see first combination in Figure 4.2);
2. Measurements when the four high level parameters and the ambient temperature are set to their respective higher bounds (see second to last combination in Figure 4.2);
3. Lastly, the influence of each parameter combination is computed by the relative difference between the measurements in 1 and 2. The results of the HW power profiling are presented in Table 4.2.

Parameter	**Relative difference** (%)
Tx power	75
Bandwidth	3 (For 2560 MHz)
Carrier frequency	4
Temperature	20.2

Table 4.2: The device power profiling summary showing that Tx power has the most influence on the RF subsystem power consumption followed by the ambient temperature bandwidth and carrier frequency.

The influence of each of the parameters in Table 4.2 is depicted in Figures 4.3a, 4.3b, 4.3c and 4.4. Figure 4.3a shows the significance of temperature on power consumption especially for Tx powers greater than 5 dBm. Nevertheless, the

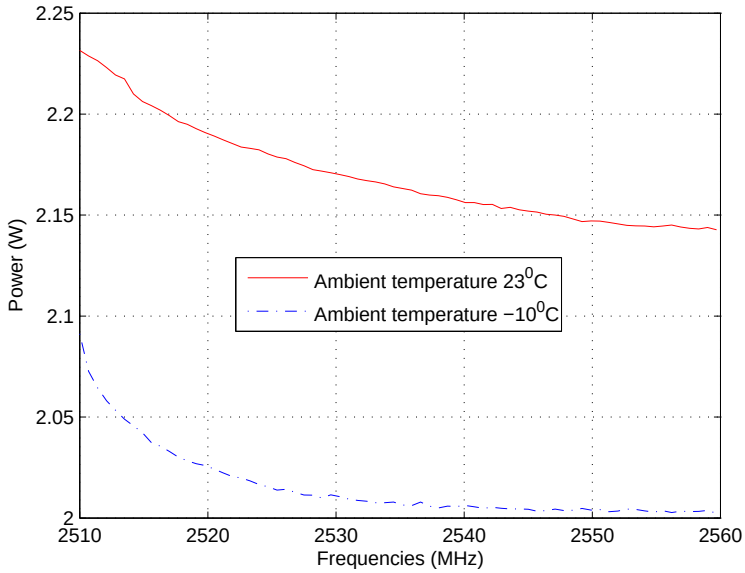

(a) Band 7 power consumption sweep.

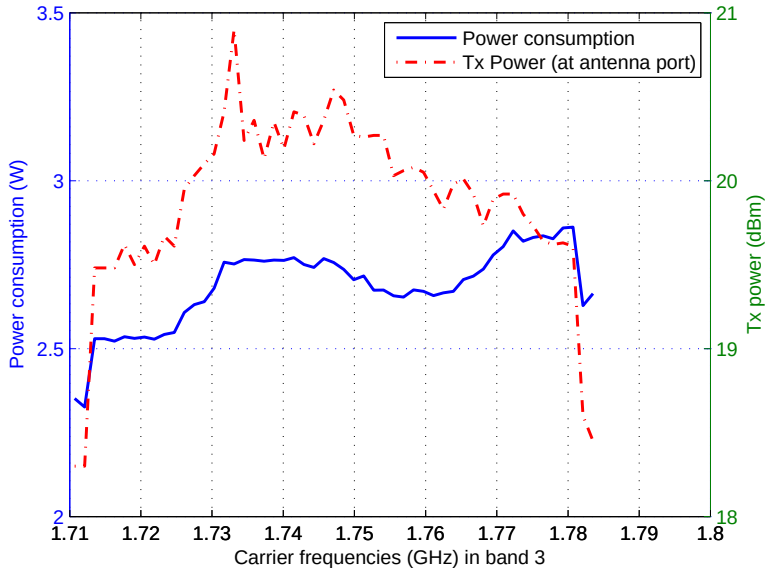

(b) Band 3 power consumption sweep.

Figure 4.1: The RF subsystem power consumption as a function of carrier frequency swept with a bandwidth of 1.4 MHz in LTE bands 7 and 3. Figure 4.1a shows a power consumption sweeping of band 7 at temperatures -10^0 and 23^0 C. Figure 4.1b shows a power consumption sweep of band 3 along with the measured Tx power at the antenna port. These plots illustrate that the power consumption within the different bands can behave very differently.

Legend				
Low bound (LB)				
High bound (HB)				
Parameters	**LB**	**HB**		
Frequency	2560	2510	MHz	
Tx power	-40	23	dBm	
Bandwidth	10	20	MHz	
Temperature	-10	55	C	
characterization combinations:				
Frequency		Frequency		Frequency
Tx power		Tx power		Tx power
Bandwidth		Bandwidth		Bandwidth
Temperature		Temperature		Temperature
Frequency		Frequency		
Tx power		Tx power		
Bandwidth		Bandwidth		
Temperature		Temperature		

Figure 4.2: The combinations for logical and environmental parameters used for device profiling.

temperature is not correlated to the bandwidth as shown in Figures 4.3b and 4.3c. In regards to the carrier frequency, the power consumption can behave differently from band to band as shown in Figure 4.1. Figure 4.4 shows the relationship between carrier frequency and temperature. It can be observed that the temperature effect on power consumption is homogeneous over the carrier frequency bands.

4.3.2.1 Training and validation sets

Table 4.2 shows that the Tx power has the biggest impact on the RF subsystem power consumption. Thus, the training and validation sets were conducted as a function of Tx power. The training sets consists of the power consumption for each combination of the lower and higher bounds of the ambient temperature, carrier frequency and signal bandwidth as a function of Tx power taken at 1 dBm resolution. The validation set was conducted as a function of the parameters:

- Four carrier frequencies in band 7 (2510, 2528, 2548 and 2560 MHz);
- Ambient temperatures -10^0, 25^0 and 55^0C;
- Signal bandwidths (1.4, 5, 10, 15, 20 MHz);
- Carefully chosen Tx power (-20, -10, 1, 5, 9, 13, 17, 21dBm).

The measurements are conducted by an automated setup (Figure 4.5) and the procedure is as follows:

1. 3 training and validation sets in room temperature (25^0C). The DUT is cooled down for 10 minutes between each measurement set. It has been verified through our own experiments that the DUT takes 10 minutes to acclimatize to room temperature and 30 minutes to get to the extreme temperatures;
2. The temperature chamber is set to -10^0C. The chamber returns the estimated time to reach the set temperature and the measurements are started after this time plus 30 minutes for acclimatization. Here, 3 training and validation sets of measurements are conducted;
3. The chamber is cooled down in 30 minutes and the procedure in 2 is conducted for 55^0C.

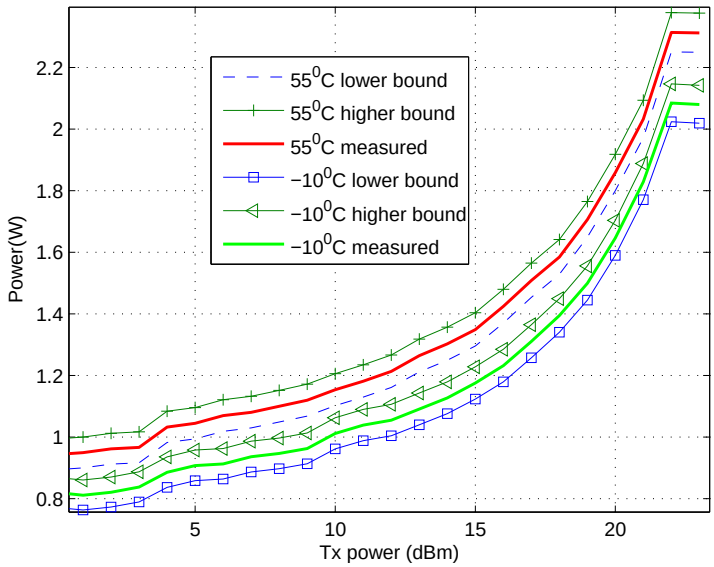

(a) Power consumption as a function of ambient temperatures of 55^0 C and -10^0 C ,
while transmitting a 20 MHz bandwidth LTE signal.

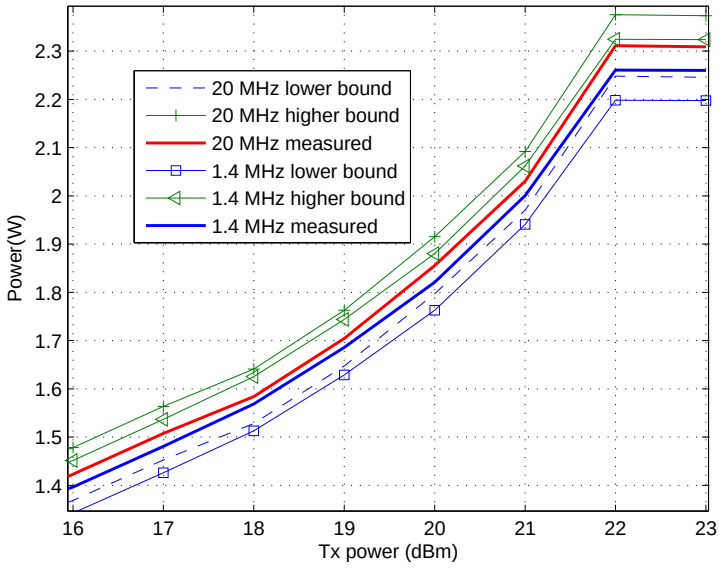

(b) Power consumption as a function of the LTE signal bandwidth at an ambient ,
temperature of $55^0 C$.

Figure 4.3: Power consumption as function of temperature continued on the next page...

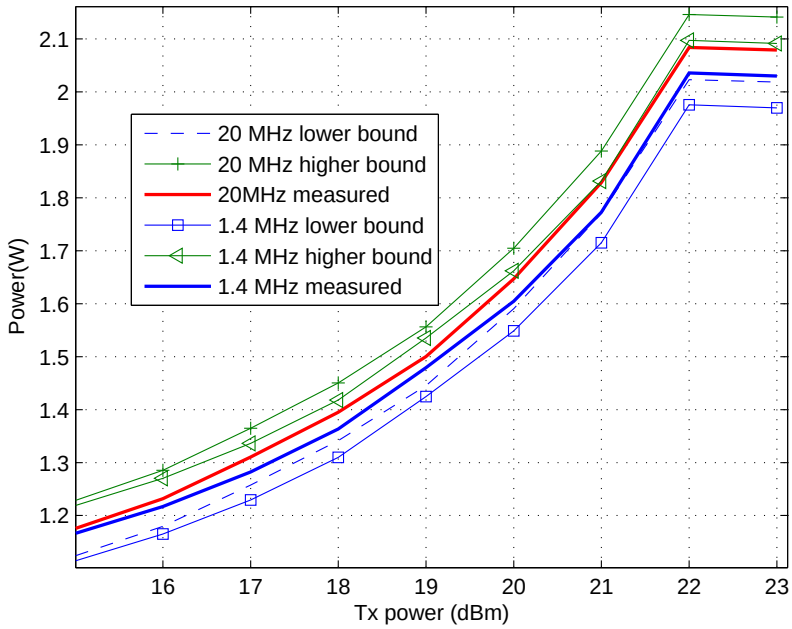

(c) Power consumption as function signal bandwidth at $-10^0 C$.

Figure 4.3: The influence of temperature on power consumption for signal bandwidths 1.4 and 20 MHz is depicted. Measurements in Figures 4.3a, 4.3b and 4.3c are measured at a carrier frequency of 2560 MHz. The Tx power range is chosen for better visibility but measurements were conducted for the full Tx power range [-40 23] dBm (this regards all corresponding figures plotted as a function of Tx power).

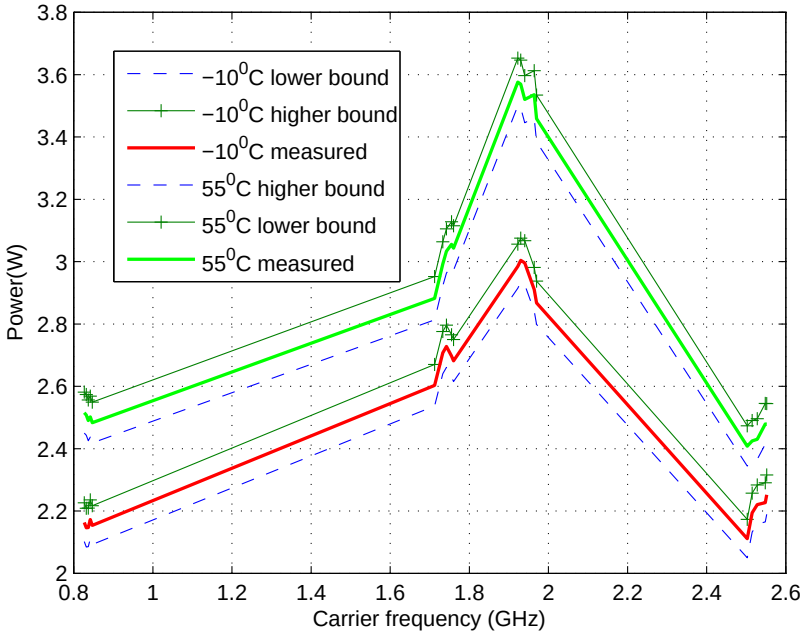

Figure 4.4: Power consumption as a function of frequency measured at ambient temperatures of -10^0C and 55^0C while transmitting a 20 MHz signal at 23 dBm.

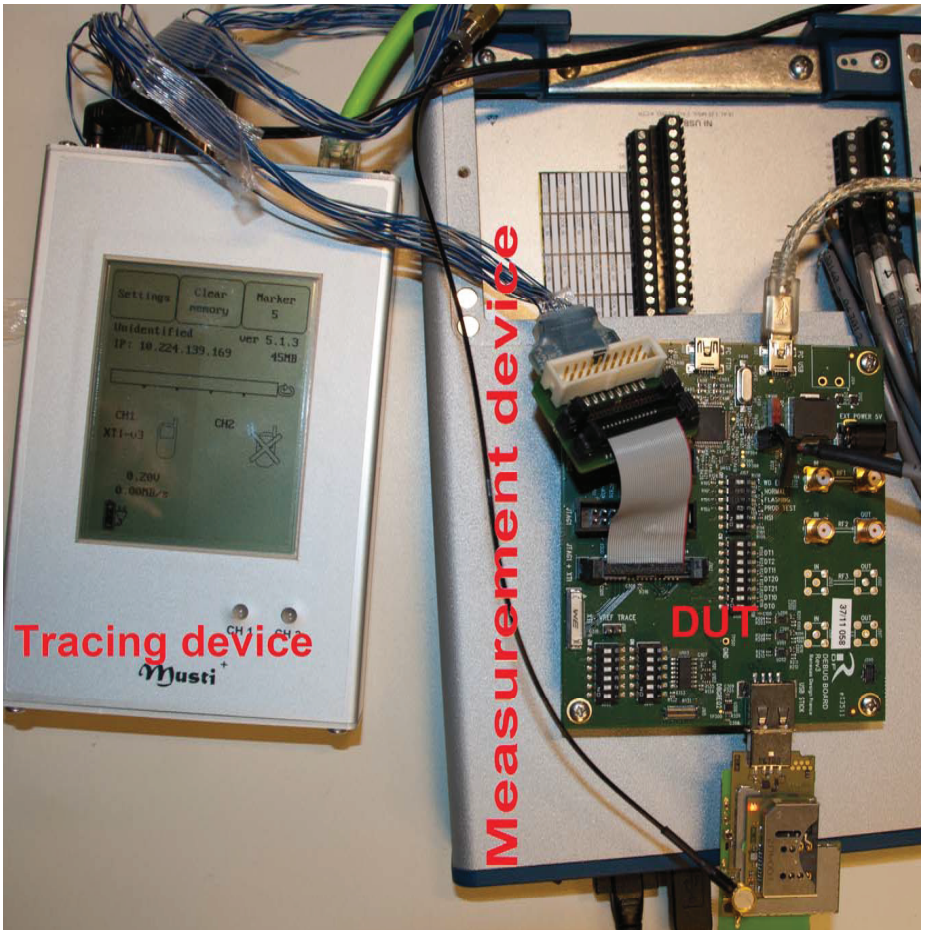

Figure 4.5: These devices are cabled to the work station that automatically conducts power measurements. The DUT is controlled via the tracing device to perform transmitting operations. For each operation, a NI *National Instruments* Labview executable is called that records the consumed current.

4.3.3 The power consumption modeling

In this section, the multivariate modeling approaches below are introduced and applied for modeling the power consumption of the RF subsystem:

- Multivariate polynomial fitting;
- Neural Networks;
- Homotopy continuation .

4.3.3.1 Multivariate polynomial fitting

The RF subsystem power measurements as a function of the Tx power increases exponentially for each of the power relevant logical interface parameters, bandwidth and carrier frequency, as shown in Figure 4.3. The power consumption as the function of the logical interface parameters is therefore a multivariate polynomial surface known at the measured points. A function $f(w_1, ..., w_m, c_0, ..., c_{p-1}) = \sum_{k=0}^{p-1} c_k \phi_k(w_1, w_2, ..., w_m)$ that models the power consumption can be constructed [89, 90] where p is the number of elements in the polynomial of m variables, w the function variables and c the polynomial coefficients. Without loss of generality, for a second-order bivariate polynomial model [91], $f(\cdot)$ becomes:

$$\begin{aligned} f(\boldsymbol{w}, \boldsymbol{c}) &= \boldsymbol{c}^T \phi(\boldsymbol{w}) \\ \boldsymbol{c} &= [c_1, c_2, ..., c_6]^T \\ \phi(w) &= [1 \; w_1 \; w_2 \; w_1^2 \; w_2^2 \; w_1 w_2] \end{aligned} \tag{4.1}$$

Given $m > K$ data points from a training data set P where K is the number of elements in $f(\boldsymbol{w}, \boldsymbol{c})$, the coefficients $\boldsymbol{c}$ can be computed as $\boldsymbol{c} = (\Phi^T \Phi)^{-1} \Phi^T P$ where $\Phi \in \mathcal{R}^{m \times K}$ is the Jacobian matrix of $\phi(x)$ [91]:

$$\Phi = \begin{pmatrix} 1 & w_{1,1} & w_{2,1} & w_{1,1}^2 & w_{1,1} w_{2,1} & w_{2,1}^2 \\ \vdots & \vdots & \vdots & \vdots & \vdots & \vdots \\ 1 & w_{1,m} & w_{2,m} & w_{1,m}^2 & w_{1,m} w_{2,m} & w_{2,m}^2 \end{pmatrix}$$

However, the m variables, Tx power, signal bandwidth and carrier frequency, affecting the RF subsystem power consumption are of different lengths and the Jacobian matrix of $\Phi(x)$ cannot be used for the computation of the coefficients

$\boldsymbol{c}$. Thus, for a second-order bivariate polynomial of variables of lengths M and N, $\Phi' \in \mathcal{R}^{(M\times N)\times K}$ for the variables bandwidth $B_{1,\dots M}$ and Tx power $T_{1,\dots,N}$ is constructed as:

$$\Phi' = \begin{pmatrix} B_1^d & \cdots & B_1 & B_1T_1 & T_1^d & \cdots & T_1 & 1 \\ B_2^d & \cdots & B_2 & B_2T_1 & T_1^d & \cdots & T_1 & 1 \\ \vdots & \vdots & \vdots & \vdots & \vdots & \vdots & \vdots & 1 \\ B_M^d & \cdots & B_M & B_MT_1 & T_1^d & \cdots & T_1 & 1 \\ B_1^d & \cdots & B_1 & B_1T_2 & T_2^d & \cdots & T_2 & 1 \\ \vdots & \vdots & \vdots & \vdots & \vdots & \vdots & \vdots & 1 \\ B_M^d & \cdots & B_M & B_MT_2 & T_2^d & \cdots & T_2 & 1 \\ \vdots & \vdots & \vdots & \vdots & \vdots & \vdots & \vdots & 1 \\ B_M^d & \cdots & B_M & B_MT_N & T_N^d & \cdots & T_N & 1 \end{pmatrix}$$

.

In polynomial fitting, the optimization finds the degree d for Φ' that satisfies the targeted accuracy. For the scenario where the RF power consumption is a function of the Tx power and bandwidth, the multivariate polynomial model would be obtained as:

1. Construction of a multivariate matrix Φ' of degree d. Start with d = 1;
2. Least squares fit to find the model $\mathbf{c} = (\Phi'^T\Phi')^{-1}\Phi'^T P$ [89, 90];
3. Evaluation of the model against an independent set of data P_t. If the desired precision is not met, the degree d is increased and iterate from step 1. The desired precision must be less than or equal to the uncertainty in the measurement setup.

4.3.3.2 Neural networks

The accuracy of an approximation depends on the density of the observation points in the input space [92]. The curse of dimensionality [93] makes the accuracy of an approximation in high-dimensional spaces to require the sample size to grow exponentially with the input dimension. With the neural networks, this is solved by not having the dimension visible in the convergence rate but hidden in a functional class [92]. Herein, continuous functions on $[0\ 1]^d$ are represented as additive superpositions of continuous one-dimension functions.

For a compactly supported function f with $supp(f) \subseteq [0\ 1]^d$, define a functional class by [92]:

$$C_f = \int_{\mathcal{R}^d} |\omega|\ |\hat{f}(\omega)| d\omega < \infty$$

where $|\hat{f}(\omega)|$ denotes the Fourier transform of f. We have an approximation

$$f_n(x) = \sum_{i=1}^{n} c_i \sigma(a_i^T x + t_i) + c_0$$

of the compactly supported function f such that

$$||(f_n - f)1_{[0,1]^d}||_2 \leq 2\sqrt{d}\ C_f\ n^{-1/2}$$

where $\sigma(\cdot)$ is the nonlinear sigmoid function whereby $\sigma(x) \to 1$ as $x \to \infty$ and $\sigma(x) \to 0$ as $x \to -\infty$.

The neural networks have been utilized for modeling the RF subsystem power consumption at the system level of abstraction [22]. In this section, we examine the performance of the neural networks at prototype level. In the transmission mode of the RF subsystem, we do have a continuous power consumption function $P(t)$, as a function of Tx power, signal bandwidth, carrier frequency and ambient temperature. The functional form of P can be defined as a $4 \times 5 \times 1$ neural network [94] shown in Figure 4.6 with one hidden layer.

Given an independently measured data set $P_t(t)$, the coefficients $W^{(1)}$ and $W^{(2)}$ can be optimized towards a minimal error between $P_t(t)$ and $P_m(t)$. The output $P_m(t)$ of the neural network is defined as:

$$P_m(t) = \sum_{j=0}^{M} W_j^{(2)} Z_j, \qquad M = 1...5, Z_0 \equiv 1 \tag{4.2}$$

$$Z_j = \sigma\left(\sum_{i=0}^{d} W_{ji}^{(1)} input_i(t) \right), \quad d = 1...4, input_0 \equiv 1 \tag{4.3}$$

where $input_i$ is the combination of the logical interface parameters at time t. The bias terms ($input_0$ for the hidden and Z_0 for output units) play an important role in ensuring that the network can represent general non-linear mappings [95]. The pivotal task in the neural networks is the optimization of the hidden units weights $W^{(1)}$ and the output weights $W^{(2)}$. The optimization is achieved through the minimization of the quadratic cost function (sum-of-squared errors function in Equation 4.4) between the data set P_t and the modeled power P_m.

$$E(W^{(1)}, W^{(2)}) = \frac{1}{2} \sum_{n=1}^{N} \{P_m(input_n, W^{(1)}, W^{(2)}) - P_{t_n}\}^2 \tag{4.4}$$

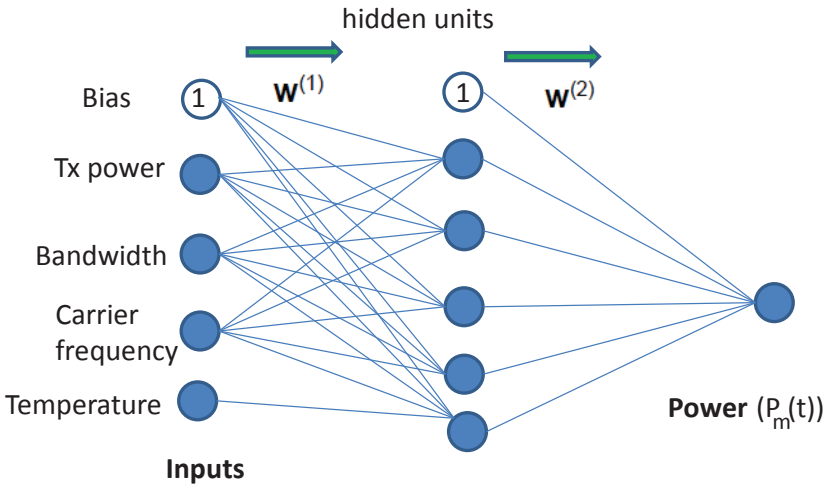

Figure 4.6: Network diagram for the two layer neural network used for modeling the power consumption of the RF subsystem. The input, hidden and power variables are denoted by nodes and the weight parameters are denoted by links between nodes. The arrows show the direction of the information flow through the network during forward propagation. The output of the network is the modeled power $P_m(t)$.

Iterative schemes taking steps in the weight space that minimize the sum-of-squared error function are utilized for finding the optimum weights. In this work, we have evaluated the following non-linear optimization algorithms towards an algorithm with the least sum of squared errors:

- Gradient descent [94];
- Pseudo-Gauss-Newton [96];
- Conjugate gradient algorithms [97, 98];
  - Hestenes-Stiefel;
  - Fletcher-Reeves [99, 100];
  - Polak-Ribiere.

It is worth noticing that the principal disadvantages of neural networks in modeling stem from the requirement of a suitable set of example data for network

training, and the potential problems which can arise if a network is required to extrapolate to new regions of the input space which are significantly different from those corresponding to the training data [95]. This means that for any of the parameters affecting the power consumption of RF subsystem, characterization for each combination should be conducted with the highest possible resolution. Hence, 64 transmission powers, 7 signal bandwidths and 20 carrier frequencies(assuming 5 supportable bands), $64 \times 7 \times 20$ measurements.

4.3.3.3 Numerical methods using homotopy and interval analysis

An homotopy is a continuous deformation of geometric figures or paths or more generally functions: a function (or a path, or a geometric figure) is continuously deformed into another one [101]. Such functions or paths are then considered equivalent: i.e., homotopic. Originally, homotopy was used as a tool to decide weather two paths with same end-points would lead to the same result of integration. The use of homotopies can be tracked back to works of Poincaré (1881-1886), Klein (1882-1883), and Berstein (1910) [101].

A homotopy is defined as a continuous map between two continuous functions in a topological space. A homotopy can, therefore, be viewed as a *continuous deformation*. The use of deformations to solve non-linear systems of equations may be traced back at least to Lahaye (1934) [101].

A homotopy between two continuous functions f_0 and f_1 from a topological space $\mathcal{X}$ to a topological space $\mathcal{Y}$ is defined as a continuous map $\mathcal{H} : \mathcal{X} \times [0,1] \rightarrow \mathcal{Y}$ from the Cartesian product of the topological space $\mathcal{X}$ with the unit interval $[0,1]$ to $\mathcal{Y}$ such that

$$\mathcal{H}(\mathbf{x}, 0) = f_0, \text{ and} \tag{4.5}$$

$$\mathcal{H}(\mathbf{x}, 1) = f_1, \tag{4.6}$$

where $\mathbf{x} \in \mathcal{X}$. The second parameter of $\mathcal{H}$, also called the *homotopy parameter*, allows for a continuous deformation of f_0 to f_1 [101].

Two continuous functions f_0 and f_1 are said to be *homotopic*, denoted by $f_0 \simeq f_1$, if, and only if, there is a homotopy $\mathcal{H}$ taking f_0 to f_1. Being homotopic is an equivalence relation on the set $\mathrm{C}(\mathcal{X}, \mathcal{Y})$ of all continuous functions from $\mathcal{X}$ to $\mathcal{Y}$.

We use homotopies in order to reconstruct the unknown function of the consumed power of several power influencing variables (logical interface parameters and the physical environmental variables) from the measured values obtained

by fixing one variable (that will be used as homotopy parameter) and varying another variable (or possibly several other variables). In this way, we study the projections of the graph of that function of the consumed power on lower dimensional spaces (usually two dimensional spaces) corresponding to limit values of the range of the RF subsystem power influencing variable used as homotopy parameter (e.g. carrier frequency or temperature). The homotopies are specifically very strong in the modeling of continuous variables in our case the physical environmental variable temperature. In the case of the temperature, a continuous map $\mathcal{H} : \mathcal{X} \times [0, 1] \rightarrow \mathcal{Y}$ can be used to model the power consumption as a function of temperature in the defined temperature range (-10^0C to $+55^0C$) [85]. The homotopy parameter λ would be set as $\lambda = 0$ and $\lambda = 1$ for the power consumptions at temperatures -10^0C and $+55^0C$ respectively and all the power consumptions in this range are on the homotopy curve as λ goes from 0 to 1.

Interval analysis is a well-known method for computing bounds of a function, being given bounds on the variables of that function [76]. The basic mathematical object in interval analysis is the interval instead of the variable. The operators need to be redefined to operate on intervals instead of real variables. This leads to an interval arithmetic. In the same way, most usual mathematical functions are redefined by an interval equivalent. Interval analysis allows one to certify computations on intervals by providing bounds on the results. The uncertainty of each measure can be represented using an interval defined either by a lower bound and higher bound or a midpoint value and a radius. The uncertainty of the consumed power as a function of a variable (say bandwidth) can be represented by higher bound plot and a lower bound plot. The consumed power in between the measured points can be interpolated linearly or by using cubic splines. The theoretical assumption that the consumed power is monotonically increasing with respect to the defined power influencing variables is tested by computing the intersection of the areas between the lower bound plots and the higher bound plots corresponding to the limit values of the homotopy parameter. Types of homotopies:

1. Linear:
$$H_1 = (1 - \lambda)f_1 + \lambda f_2$$
2. Non Linear:
$$H = (1 - \lambda)^\alpha f_1 + \lambda^\alpha f_2$$
   (a) Linearly varying non-linear homotopy:
$$H = (1 - \lambda)^\alpha f_1 + \lambda^\alpha f_2$$
   where $\alpha = a\lambda + b$, where a and b are real constants;

(b) Quadratically varying non-linear homotopy:

$$H = (1-\lambda)^{\alpha} f_1 + \lambda^{\alpha} f_2$$

where $\alpha = a\lambda^2 + b\lambda + c$, where a, b and c are real constants.

In the device profiling section, we found out that we have 4 influencing parameters; Carrier frequency ($fb7$), Tx power (txp), temperature (T) and signal bandwidth (BW). Given that the Tx power has the most significant influence on the RF subsystem power consumption, the Tx power has to be the running variable for each of the homotopies of the other parameters. Numerically, it's always the input parameter with the widest range that is chosen as the running variable but in our case, we also have to consider the practicality of the input parameters. Our target is the homotopy $H_7(txp, \lambda_{bw}, \lambda_{fb7}, \lambda_T)$, explained below, that computes the power consumption of the RF subsystem for any given Tx power, signal bandwidth, carrier frequency and temperature. This is achieved through a combination of homotopies for each of the power influencing parameters as illustrated here:

The homotopy continuation based computation of power consumption as a function of Tx power and signal bandwidth at the lower bound of the carrier frequency and temperature.

$$\left.\begin{aligned} f_1(txp) &= \underset{\overline{BW},\underline{fb7},\underline{T}}{P_1(txp)}, \\ f_2(txp) &= \underset{\underline{BW},\underline{fb7},\underline{T}}{P_2(txp)}, \end{aligned}\right\} \quad \underset{\underline{fb7},\ \underline{T}}{H_1(txp, \lambda_{bw})} = (1-\lambda_{bw})^{\alpha} f_1(txp) + \lambda_{bw}^{\alpha} f_2(txp)$$

The homotopy continuation based computation of power consumption as a function of Tx power and signal bandwidth at the higher bound of the carrier frequency and lower bound of temperature.

$$\left.\begin{aligned} f_3(txp) &= \underset{\overline{BW},\overline{fb7},\underline{T}}{P_3(txp)}, \\ f_4(txp) &= \underset{\underline{BW},\overline{fb7},\underline{T}}{P_4(txp)}, \end{aligned}\right\} \quad \underset{\overline{fb7},\ \underline{T}}{H_2(txp, \lambda_{bw})} = (1-\lambda_{bw})^{\alpha} f_3(txp) + \lambda_{bw}^{\alpha} f_4(txp)$$

The homotopy continuation based computation of power consumption as a function of Tx power and signal bandwidth at the lower bound of the carrier frequency and higher bound of temperature.

$$\left.\begin{aligned} f_5(txp) &= \underset{\overline{BW},\underline{fb7},\overline{T}}{P_1(txp)}, \\ f_6(txp) &= \underset{\underline{BW},\underline{fb7},\overline{T}}{P_2(txp)}, \end{aligned}\right\} \quad \underset{\underline{fb7},\ \overline{T}}{H_4(txp, \lambda_{bw})} = (1-\lambda_{bw})^{\alpha} f_5(txp) + \lambda_{bw}^{\alpha} f_6(txp)$$

The homotopy continuation based computation of power consumption as a function of Tx power and signal bandwidth at the higher bound of the carrier frequency and temperature.

$$\left.\begin{aligned} f_7(txp) &= \underset{\overline{BW},\overline{fb7},\overline{T}}{P_3(txp)}, \\ f_8(txp) &= \underset{\underline{BW},\overline{fb7},\overline{T}}{P_4(txp)}, \end{aligned}\right\} \quad H_5(txp,\lambda_{bw}) = (1-\lambda_{bw})^{\alpha} f_7(txp) + \lambda_{bw}^{\alpha} f_8(txp)$$
$$\underline{fb7},\ \overline{T}$$

$$\left.\begin{aligned} H_3(txp,\lambda_{BW},\lambda_{fb7}) &= (1-\lambda_{fb7})^{\alpha} H_1(txp,\lambda_{bw}) + \lambda_{fb7}^{\alpha} H_2(txp,\lambda_{bw}) \\ H_6(txp,\lambda_{BW},\lambda_{fb7}) &= (1-\lambda_{fb7})^{\alpha} H_4(txp,\lambda_{bw}) + \lambda_{fb7}^{\alpha} H_5(txp,\lambda_{bw}), \end{aligned}\right\} \quad H_7$$
$$\underline{T}$$
$$\overline{T}$$

$$H_7(txp,\lambda_{bw},\lambda_{fb7},\lambda_T) = (1-\lambda_T)^{\alpha} H_3(txp,\lambda_{BW},\lambda_{fb7}) + \lambda_T^{\alpha} H_6(txp,\lambda_{BW},\lambda_{fb7})$$

Where:

$$\lambda_{BW} = \frac{BW - 1.4}{20 - 1.4} \tag{4.7}$$

$$\lambda_{fb7} = \frac{fb7 - 2510}{2560 - 2510} \tag{4.8}$$

$$\lambda_T = \frac{T + 10}{55 + 10} \tag{4.9}$$

$$\alpha = 1 \tag{4.10}$$

4.3.4 Evaluation of the RF subsystem Power modeling approaches

This section evaluates multivariate modeling approaches towards an approach with the highest mathematical approximation accuracy [102, 103]. The evaluation was conducted in Matlab using a floating-point relative accuracy of 2.2204×10^{-16} [104]. The mathematical approximation accuracy is the closeness of agreement between the modeled and measured power consumption [72, 105].

The accuracy is computed in terms of the relative error e_r which is between the measured power P (validation data set) and the modeled power $\hat{P}$ i.e.

$$e_r = \frac{\|P - \hat{P}\|_{\infty}}{\|P\|_{\infty}} \tag{4.11}$$

$$accuracy = 1 - e_r \tag{4.12}$$

In interval analysis, each interval can be defined by a midpoint and a range. The midpoint being the most likely value of the real variable if nothing else is known or assumed about the spatial distribution of the measures. Then, the uncertainty is the range divided by 2 and the relative uncertainty is half of the range of the interval divided by the midpoint value [106–108].

The absolute modeling target is to have the relative error e_r of the modeling approaches to be less than or equal to the uncertainty/precision of the measurements [106]. The DUT was set to transmit 100 sub-frames 1000 times at 23 dBm using 20 MHz signal bandwidth at three temperatures -10^0C, 25^0C and 55^0C. The precisions 5.5%, 4.5% and 5.4% where obtained as the relative difference in each of the measurements for ambient temperatures -10^0C, 25^0C and 55^0C.

The modeling approach(es) that will prove to have the modeling errors within the measurement uncertainties will subsequently be tried on a "validation" prototype. This prototype is made up of the same platform as the prior but with different RF subsystem design. The major difference is that the RF subsystem of the device used in the evaluation has a different power amplifier for Lower frequency bands as band 5, high frequency bands as band 3 and 1 and band 7. Meanwhile the device to be used for validation has a single power amplifier for all bands which means that this device should have different power consumption behaviors compared to the prior as it has to be tuned for all the frequency bands.

4.3.4.1 Multivariate polynomial performance

The evaluation of the power modeling capabilities of this approach started in 3-dimensions for the RF subsystem power consumption as a function of signal bandwidth and Tx power. The intention was to increase the dimension if the performance proved to be within our targets. However, the evaluation of the multivariate polynomial fitting in Figure 4.7 shows that this methodology can reach a minimum sum-of-squared errors of 0.19 corresponding to a relative error of 5.9% before the Φ' matrix got too close to becoming singular (hence determinant close to 0 making the Φ' matrix invertible).

Thus given this performance, we can rule out the application of the multivariate polynomial fitting for the modeling of the power consumption of the RF subsystem.

Finally, we have compared the relative error obtained using smoothing spline curves, thin-plate spline surfaces and piecewise linear and cubic spline surfaces

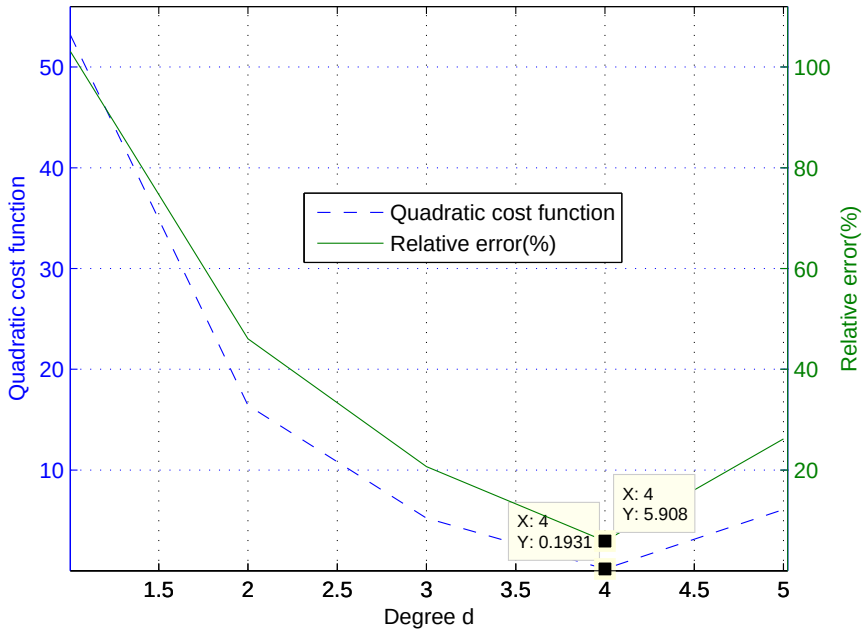

Figure 4.7: The performance of multivariate polynomial fitting showing that this approach cannot get better than a quadratic cost function value of 0.1931.

with our requirement of 4.5%. While the relative error obtained using smoothing spline curves (3,12%) and piecewise linear and cubic spline surfaces (2,78% for both of them) are acceptable, the relative error obtained using thin plate spline surfaces is not acceptable (7,76%). Even the most precise local polynomial interpolation methods are outperformed by homotopy continuation (see below).

4.3.4.2 Neural network performance

The evaluation of this approach was initiated in 4-dimensions for modeling the power consumption as a function of Tx power, signal bandwidth and frequency (only the lower and higher bounds of LTE band 7 were considered). As this approach is based on taking iterative steps in the weight space towards the optimal weights, the performance of the non-linear optimization algorithms for the training of the network in Figure 4.6 is depicted in Figure 4.8. The Pseudo-Gauss-Newton algorithm has the best optimization followed by Fletcher-Reeves, Polak-

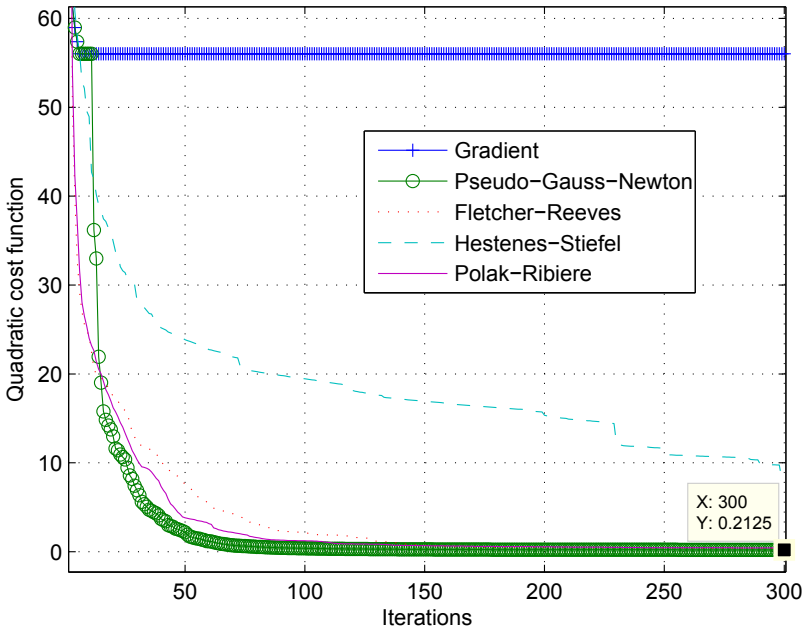

Figure 4.8: The convergence of non-linear optimization algorithms towards the minimum error between P_t and P_m. The Pseudo-Gauss-Newton algorithm converges towards the least error of 0.21 after 300 iterations.

Ribiere with the final sum-of-squared errors 0.21, 0.30 and 0.42 respectively. This experiment was conducted for the power consumption in 4-dimensions $\mathcal{P}^4$.

However, in the training of the neural network the weights $W^{(1)}$ and $W^{(2)}$, are initialized with pseudo-random values drawn from the standard uniform distribution. Hence, for the evaluation of the performance of this approach, the training in Figure 4.8 was conducted 1000 times yielding the following average relative errors for each of the optimization algorithms (see Table 4.3).

The results in the table above do show that the performance of the Neural Networks does't fall within the uncertainty in the measurements. And this is observed while considering only two carrier frequencies in band 7 and also without taking the temperature into account. Thus, to the best of our knowledge and understanding of the Neural networks modeling, the approach do not meet our targeted modeling error.

Parameter	**Relative error** (%)
Gradient	[51.8879, 77.5622]
Pseudo-Gauss-Newton	[6.2167, 11.8051]
Fletcher-Reeves	[6.8736, 15.5786]
Hestenes-Stiefel	[26.5198, 40.2193]
Polak-Ribiere	[8.2287, 9.8113]

Table 4.3: The average of the validation error for the optimization algorithms taken over 1000 trials.

4.3.4.3 Homotopy continuation performance

The evaluation of the performance of the homotopy continuation mapping approach initiated with 4-dimensional linear homotopy ($H_3(txp, \lambda_{BW}, \lambda_{fb7}, \underline{T})$ and $H_6(txp, \lambda_{BW}, \lambda_{fb7}, , \overline{T})$) with the intention of applying other types of homotopies accordingly in order to meet our target of the modeling error within the measurement uncertainty.

The validation parameters for homotopies H_3 and H_6 are:

- Tx powers 1, 9 and 17 dBm;
- Carrier frequencies 2528 and 2548 MHz;
- And signal bandwidths of 5 and 10 MHz.

The evaluation of the homotopies H_3 and H_6 against the validation measurements proved a maximum modeling error of 1.4% and 2.5% for the two homotopies respectively.

Upon the successful modeling in 4-dimensions $\mathcal{P}^4$, we moved to 5-dimensions $\mathcal{P}^5$ for modeling the power consumption for any given Tx power, signal bandwidth, carrier frequency (here only band 7 considered) and ambient temperature in $H_7(txp, \lambda_{bw}, \lambda_{fb7}, \lambda_T)$. H_7 was evaluated against a validation set of measurements at carrier frequencies 2528 and 2548 MHz, signal bandwidths 5 and 10 MHz and all Tx powers with 1 dBm resolution. **The maximum relative (equation 4.11) error between the modeled power consumption and the validation set is 3% which is within our measurement uncertainty** . For visualization, Figures 4.9a and 4.9b show the homotopy continuation based modeling of the power consumption for signal bandwidths between 1.4 MHz and 20 MHz and temperatures between -10^0C and $+55^0C$. The temperature modeling of the power consumption for ambient temperature 25^0C while transmitting

at a carrier frequency of 2560 MHz with the signal bandwidth of 20 MHz is shown in Figure 4.9c along with the corresponding measured power. Also shown are the lower and higher bounds of the measured power at 25^0C and the measured powers at -10^0C and 55^0C to prove that the modeled power consumption is within the uncertainties of the measured power. Finally, Figures 4.10a and 4.10b show the plot of two bivariate homotopy functions and their intermediate trivariate homotopy continuation interpolation at the midpoint of the homotopy parameter and a zoom of the previous plot as a function of Temperature, signal bandwidth and Tx power. Lastly, the homotopy modeling of the power consumption as a function of Tx powers while operating at a signal bandwidth of 10 MHz at a carrier frequency of 2548 MHz in an ambient temperature of 25^0C is shown in Figure 4.9d along with the lower and higher bounds of the measured power also proving that the modeled power is within the measurement uncertainties.

4.3.4.4 Modeling evaluation with a validation device

The numerical approach based on homotopy continuation has proven to have a modeling error within our measurement uncertainty. This approach was thus also put to task to model the power consumption of another design with a different RF subsystem design. For a one to one evaluation between the two devices, a test corresponding to Figure 4.9d, where power consumption was modeled as a function Tx power operating at a signal bandwidth of 10 MHz at a carrier frequency of 2548 MHz, was conducted. The performance of the homotopy $(H_7(txp, \lambda_{bw}, \lambda_{fb7}, \lambda_T))$ approach on a device with a different RF subsystem design is shown in Figure 4.11 with a modeling error of 2%.

4.3.4.5 RF subsystem power model

The overall target in this work is to find the most accurate and efficient RF subsystem power consumption model to be applied in the power emulator of the RF subsystem power emulation methodology introduced in [78]. In the evaluation of modeling approaches, the numerical approach homotopy continuation proved as the only one to have a modeling error within the measurement uncertainty of the 5-dimensional $\mathcal{P}^5$ power consumption function. Even-though in our case, linear homotopy has been sufficient for both devices used in this work, there can be cases where the modeling error can appear to be out of the uncertainty bounds of the measurements. In such cases, one would upgrade to nonlinear homotopy and subsequently linearly varying nonlinear homotopy and quadratically varying nonlinear homotopy if the prior also fails. In terms of performance,

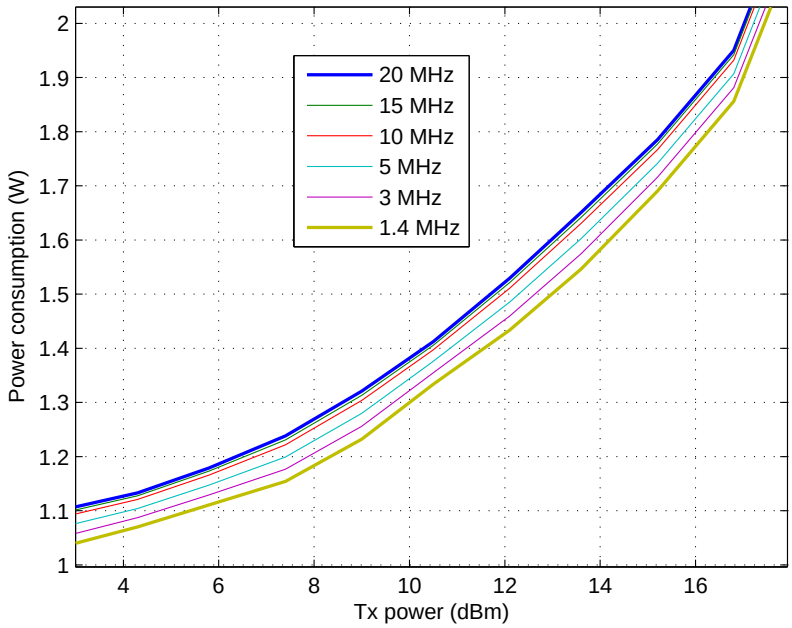

(a) Homotopy based modeling of the power consumption for signal bandwidths between 1.4 MHz and 20 MHz.

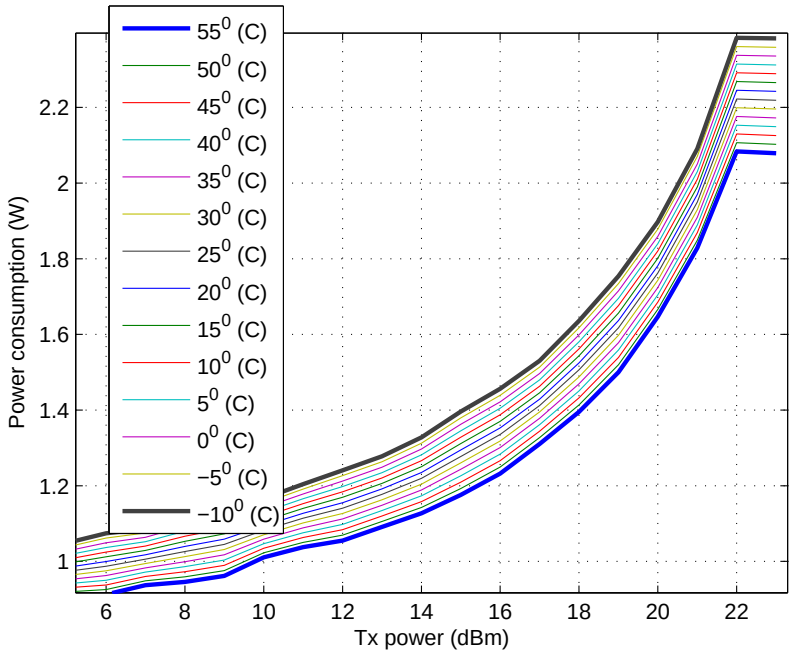

(b) Homotopy based modeling of the power consumption for ambient temperatures between -10^0C and $+55^0C$ when transmitting a 20 MHz LTE signal as a function of Tx power.

Figure 4.9: Homotopy based modeling continued on next page...

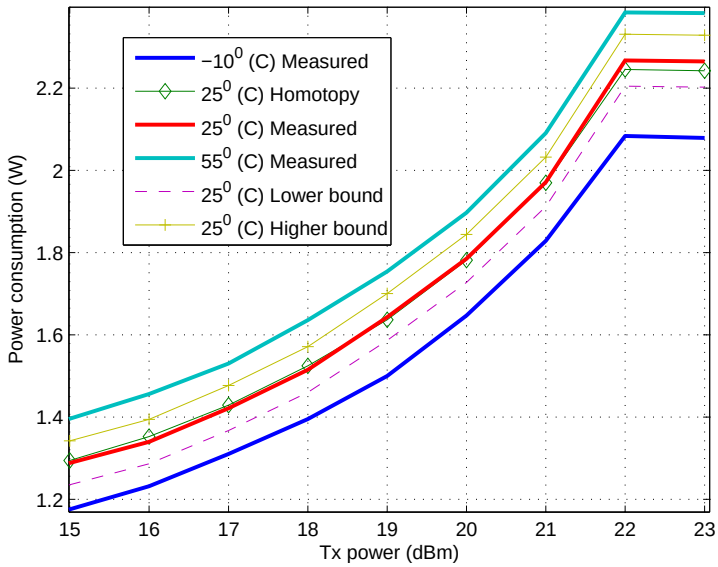

(c) Homotopy based modeling of the power consumption as a function of Tx power at signal bandwidth 20 MHz for the ambient temperature of 25^0C along with the measured power with its lower and higher bounds. Also shown are the power consumptions for ambient temperatures -10^0C and $+55^0C$.

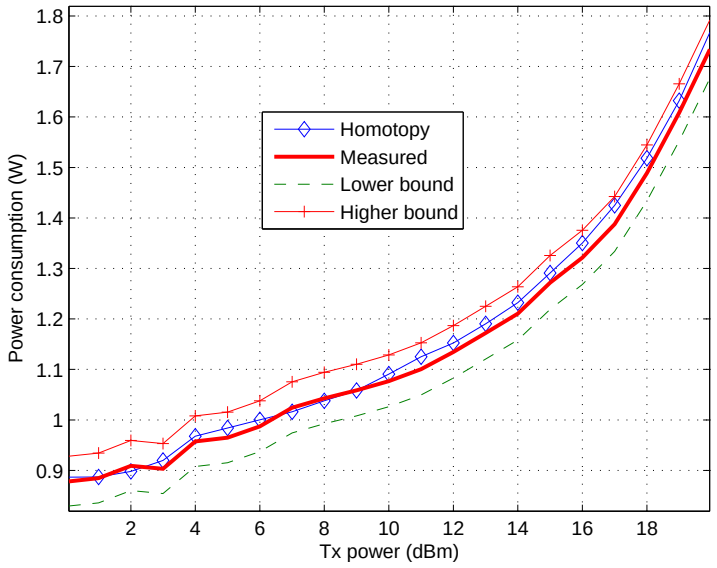

(d) The 5-dimensional homotopy modeling of bandwidth, frequency, temperature and Tx power

Figure 4.9: The homotopy based modeling of the power consumption as a function of bandwidth (Fig. 4.9a), ambient temperature (Fig. 4.9b and Fig. 4.9d) and the 5-dimensional modeling for bandwidth, frequency, temperature and Tx power in Fig. 4.9d.

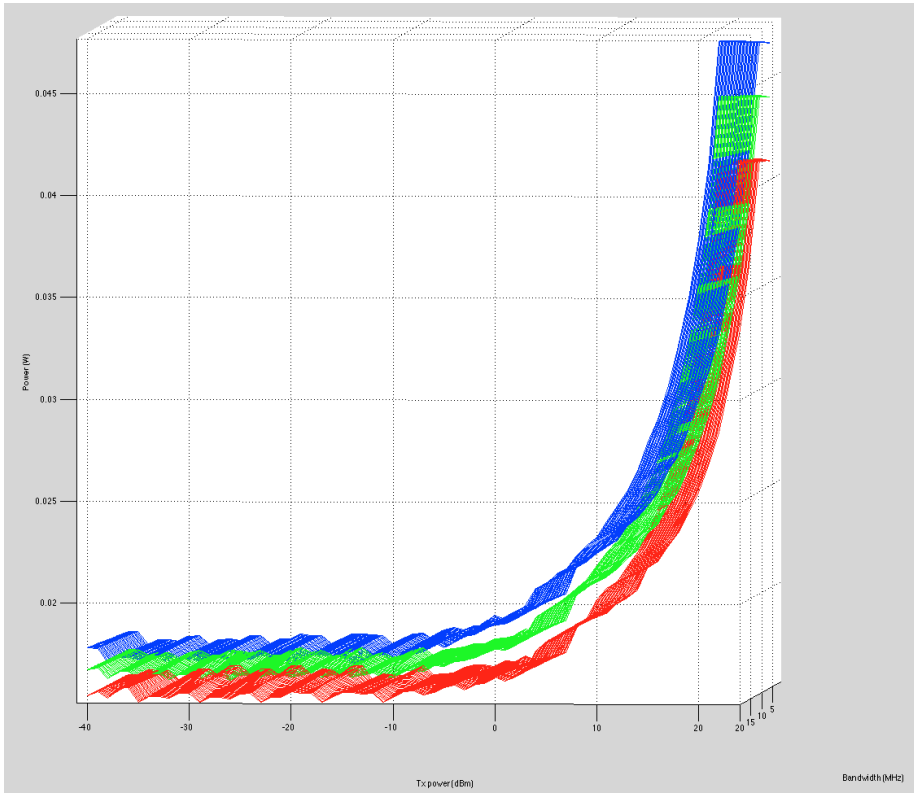

(a) Plots of two bivariate homotopy functions and their intermediate trivariate homotopy continuation interpolation at the midpoint of the homotopy parameter.

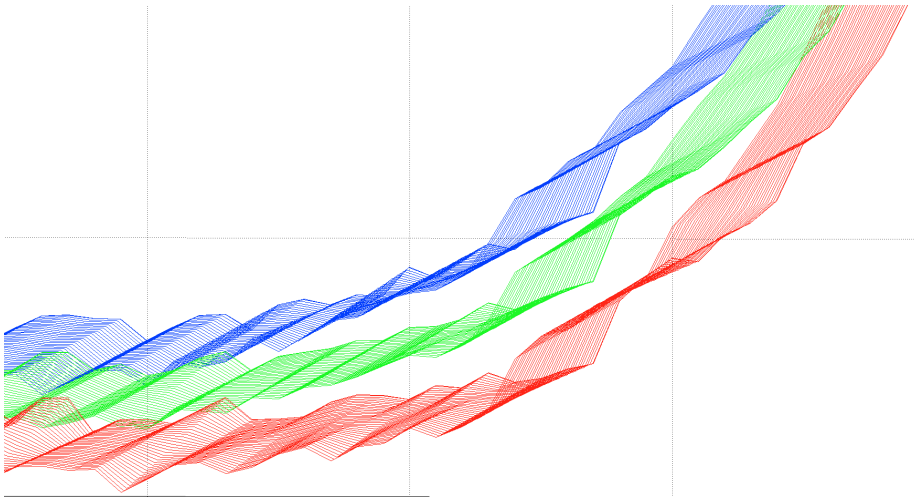

(b) Zoom of the preceding plot.

Figure 4.10: Bivariate homotopy functions.

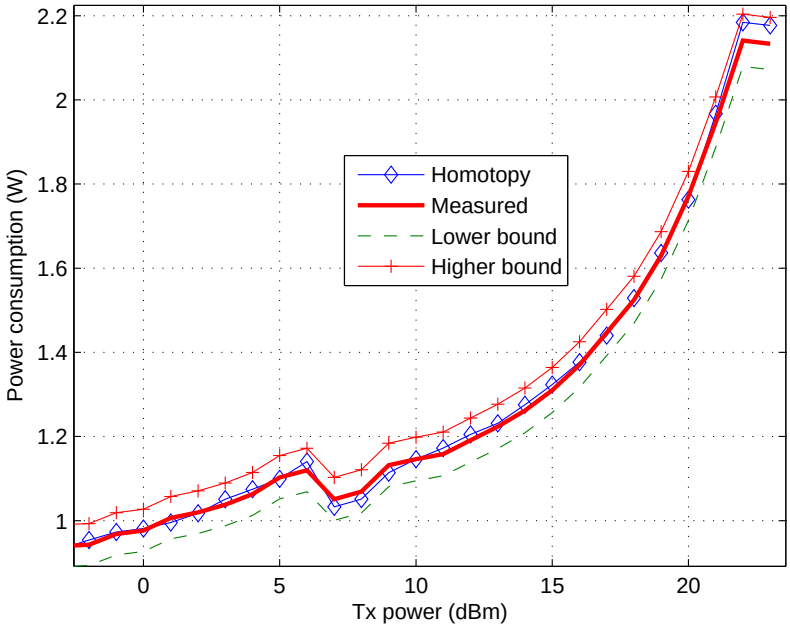

Figure 4.11: Evaluation of the homotopy approach on a device with a different RF subsystem design.

this approach has proven to have an accuracy of atleast 97% ± 2.75% (considering the worst uncertainty for the ambient temperatures) evaluated over two different RF subsystem designs. For training, the approach requires eight sets of measurements $f_1 \ldots f_8$ (presented in section 4.3.3.3) as a function of Tx power taken at a 1 dBm resolution (64 Tx power powers). For validation, a set of measurements for each ambient temperature,-10^0C, 25^0C and 55^0C is conducted. The measurements are conducted for four carefully chosen carrier frequencies (2510, 2528, 2548 and 2560 MHz in this case) for all the five operational signal bandwidths as as a function of eight carefully chosen Tx powers. Thus, 992 measurements are required for the training and validation of the homotopy approach.

4.4 Discussion

This work has focused on the modeling of the power consumption of an analog circuit, the RF subsystem, for power emulation. The power emulation methodology was introduced for digital circuits at the RTL level [66] and was proved in a feasibility study [18] to have a precision of 10%. However, the power emulation at the RTL level cannot be conducted for realistic scenarios as for the case with the RF subsystem emulated at prototype level. Secondly, the accuracy of the emulated power at prototype level is only constrained by the accuracy of the mathematical approximation. Therefore, it is only advantageous for power analysis to also have a power emulation model of the digital circuits at prototype level. The FLPA approach would also be utilized for the computation of the emulation model of the DBB.

4.5 Summary

We have in this work examined multivariate modeling approaches for an approach that can model the 5-dimensional power consumption of the RF subsystem when transmitting an LTE signal. The RF subsystem power consumption has proven to be a function of the logical interface parameters Tx power, carrier frequency and bandwidth and the ambient temperature. The numerical approach based on homotopy continuation has proven to optimally conduct the functional mapping between the RF subsystem power consumption and the logical interface between the baseband and the RF subsystem for the ambient temperatures between the defined extreme cases. This modeling approach provided a mathematical function approximation accuracy of 97% $\pm$ 2.75%. The approach was also tried on a device with a different RF subsystem design where its power consumption was modeled with an accuracy of 98% $\pm$ 2.75%.

The emulation model obtained in this chapter is utilized in the next chapter to emulate the power consumption of the RF subsystem.

Chapter 5

LTE handset RF power consumption emulation

5.1 Introduction

The methodology for emulating the power consumption of the analog part (only Tx) of the wireless modem, RF subsystem, when transmitting a LTE signal is presented in this section. The architecture of the methodology is depicted in Figure 5.1. As mentioned in Chapter 4, the power consumption of RF subsystem is a function of logical and protocol related commands, the methodology listens the logical interface between the DBB and RF system for these commands. The "parameter extractor" module extracts the carrier frequency, signal bandwidth and Tx power and forwards them to the "RF power emulator" that computes the emulated power using a predefined mathematical model.

The emulated power is a product of a mathematical mapping between the logical and protocol related commands and a predefined mathematical model. The mathematical model for any given RF subsystem design is obtained through the steps shown in the flow chart in Figure 5.2. The FPLA analysis is applied on each RF subsystem design for the computation of the mathematical model. This was conducted in Chapter 4 where the homotopy continuation numerical approach proved to meet our requirements for a power model. In this Chapter,

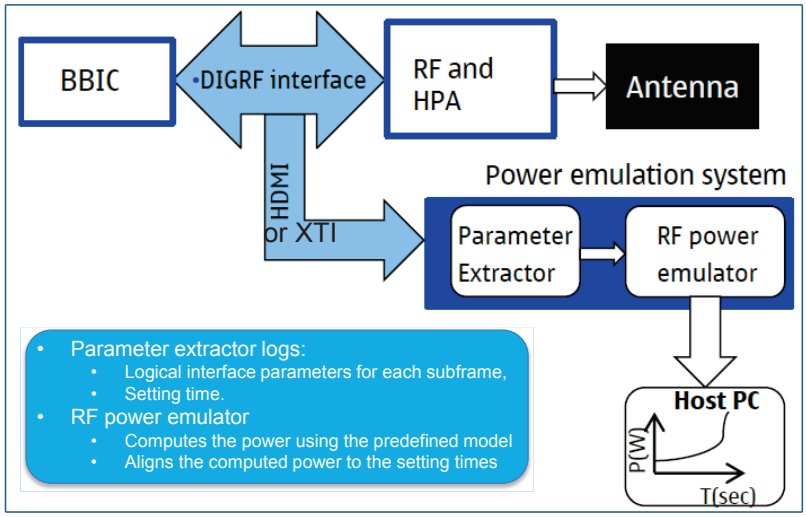

Figure 5.1: The RF subsystem power emulation system, monitors the stream of the logical commands over the DIGRF interface, extracts the RF subsystem power dependent parameters in the "Parameter extractor" module and computes the emulated power in the "RF power emulator" module.

the obtained model is put to task for emulating the power consumption of a real life scenario though still in conducted mode. The real life scenario here is the active connection while transmitting data. The power consumption of the real life scenario is to be measured along with the logical and protocol commands used for emulation. The measured and emulated powers are to be compared for real life scenario validation of the model.

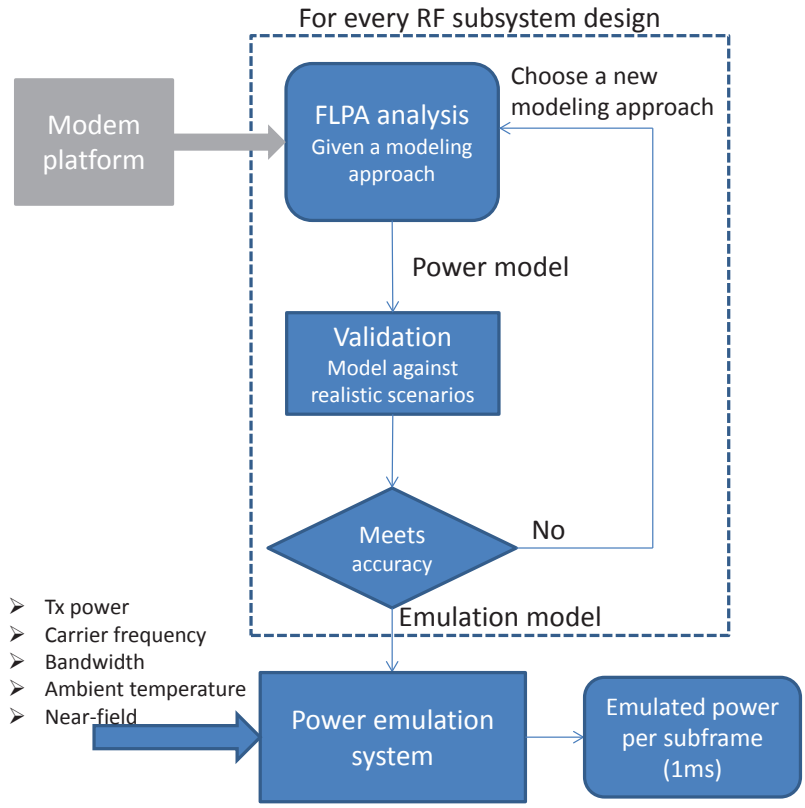

Figure 5.2: Emulation flow showing the process through which the emulation model of a RF subsystem is obtained.

5.2 Power emulation model

The evaluation of the multivariate algorithms proved the homotopy continuation numerical approach to have a modeling error within the measurement uncertainty of the data in the training sets. The approach also proved to be the least complex in terms of the number of mips and also requires the least number of measurements for training. This approach takes the power consumptions of the lower and higher bounds of signal bandwidth, carrier frequency and ambient temperature and maps the power consumption for all combinations of these parameters as a function of Tx power. Thus, power consumption of each scenario is computed during the training phase and stored. Hence, a data matrix of dimensions $14 \times 4 \times 64 \times 6$ has the power consumptions of the RF subsystem for all combinations of the logical interface parameters signal bandwidth (6), carrier frequency (4), Tx power (64) and ambient temperatures (14). Here for the temperature, 14 temperatures were chosen between the extreme conditions, $[-10^0C\ 55^0C]$, whose power consumptions had an interval larger than the measurement uncertainty. Thus, the modeling of the power consumption for any given combination of logical/protocal parameters and temperature is an indexing task. Say, the RF subsystem power consumption when transmitting at a carrier frequency 2528MHz, using a signal bandwidth of 10 MHz at a Tx power of 13 dBm in a room of 25^0C is $H_7(8, 2, 54, 3)$ where H_7 is the homotopy function obtained in Chapter 4.

5.2.1 RF subsystem Power consumption emulation

The power consumption emulation system that takes the logical interface parameters between baseband and RF subsystems, via *XTI (X/Open Transport Interface)*, as inputs to compute the LTE sub-frame average power consumption of a specific RF subsystem is depicted in Figure 5.1.

During runtime, modem SW traces containing the logical interface parameters for each sub-frame are written to the XTI port in the Tx scheduling function of the modem SW. The trace box, connected to the DUT via the XTI port, forwards the modem software traces to the work station (see Figure 5.3). The optimal emulation system would compute the emulated RF subsystem power consumption for each sub-frame in the modem SW and trace it out to the XTI port.

We have in this work chosen to work off-line where the modem SW traces are processed on the workstation for the extraction of the relevant logical interface parameters and then used for the computation of the emulated power. In order

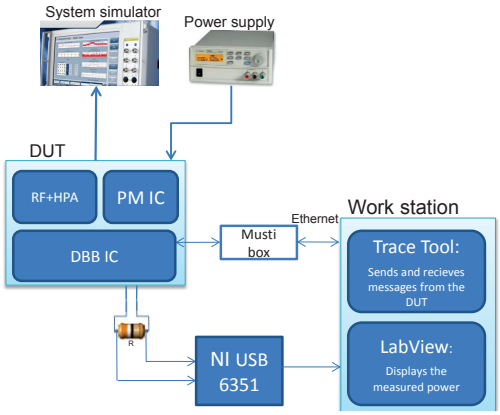

Figure 5.3: The power emulation validation setup using a system simulator.

to illustrate the computation of the emulated power in a semi-realistic scenario, the DUT is connected to a system (eNOB) simulator (see Figure 5.3). The scenario in this experiment is referred to as semi-realistic because the DUT is connected to the system simulator in conducted mode rather than the realistic radiated mode. The system simulator simulates the base-station (eNOB) which informs the DUT, among other items, which technological parameters to use for transmissions (Hence, the carrier frequency, signal bandwidth, modulation scheme, Tx power and more). However, for our experiment, we defined the technological parameters in the system simulator that were invoked in the DUT. Here during the transmission of a LTE signal on carrier frequency 2528 MHz using a signal bandwidth of 10 MHz, the following Tx powers (plotted in Figure 5.4) were observed/measured:

- **Requested Tx power:** The Tx power requested in both local and normal modes (semi-realistic scenario) of operations. In local mode, the requested power is invoked in the trace tool and in normal mode it is invoked in the system simulator;
- **Logical Tx power:** The Tx power from the logical parameters extracted during normal mode;
- **Measured Tx power in normal mode:** The measured Tx power at the antenna port during the execution of the semi-realistic scenario;
- **Measured Tx power in local mode:** The measured Tx power at the antenna port during the training of the model in Local mode.

Figure 5.4 depicts the requested Tx power, logical Tx power and the Tx power measured both in local and normal mode. The assumption in this work was that the Tx power measured at the antenna port would be in agreement for both local and normal modes of operations. However, in our case here, we do have a relative difference of 9% between the measured power in the two modes. This difference does also affect power consumption as the Tx power is the biggest contributor to the RF subsystem power consumption. The Tx power measured in local mode is on average 1.5 dBm lower than the requested power but still within the defined ±2 dB tolerance [52]. The difference in the Tx powers in these two modes is related to the fact that in normal mode of operation, there is a closed loop power control that pushes the UE to meet the requested power (if possible).

As indicated earlier that the modeling of the power consumption using the homotopy approach is an indexing task, as the carrier frequency and the signal bandwidth are constant in this scenario, the emulated power is extracted as $H_7(8, 2, x, 3)$ where x is the logical interface parameter Tx power. However, since the homotopy is computed at 1 dBm resolution, we do interpolate linearly ($f(x+y) = f(x) + y \times (f(x+1) - f(x))$, $0 < y < 1$) between the integer values for double logical interface parameter values.

The resultant emulated power along with the measured power, for validation, is depicted in Figure 5.5. The first intriguing point is the offset between the measured and the emulated power. This is due to the fact that the emulation model is trained in local mode where only the physical layers are active contrary to normal mode when the entire modem is active.

It was expected that as it is only the Tx power that is changing in this scenario, the power consumption steps, from one Tx power level to another, in both the emulated and measured power consumption should be relatively the same. The evaluation of power consumption between the lowest and highest Tx power, in Figure 5.5, yielded a relative difference of 16% between the emulated and measured power consumption. This difference, which was expected to be within the measurement precision of 4.5%, is definitely due to the fact that there is on average a 1.5 dBm difference between the Tx powers measured, in local and normal modes, at the antenna port.

The accuracy of the emulation system is dependent on the closeness of the emulated power to the measured power consumption hence 84% ± 2.75% in our case. The emulation model applied has an accuracy of 97% ± 2.75% and the emulation system accuracy was expected to also be around this accuracy but definitely not out of the range of the measurement precision. However, due to the fact that we do have a Tx power tolerance of ±2 dBm and also given the open loop power control during training in local mode, the measured power

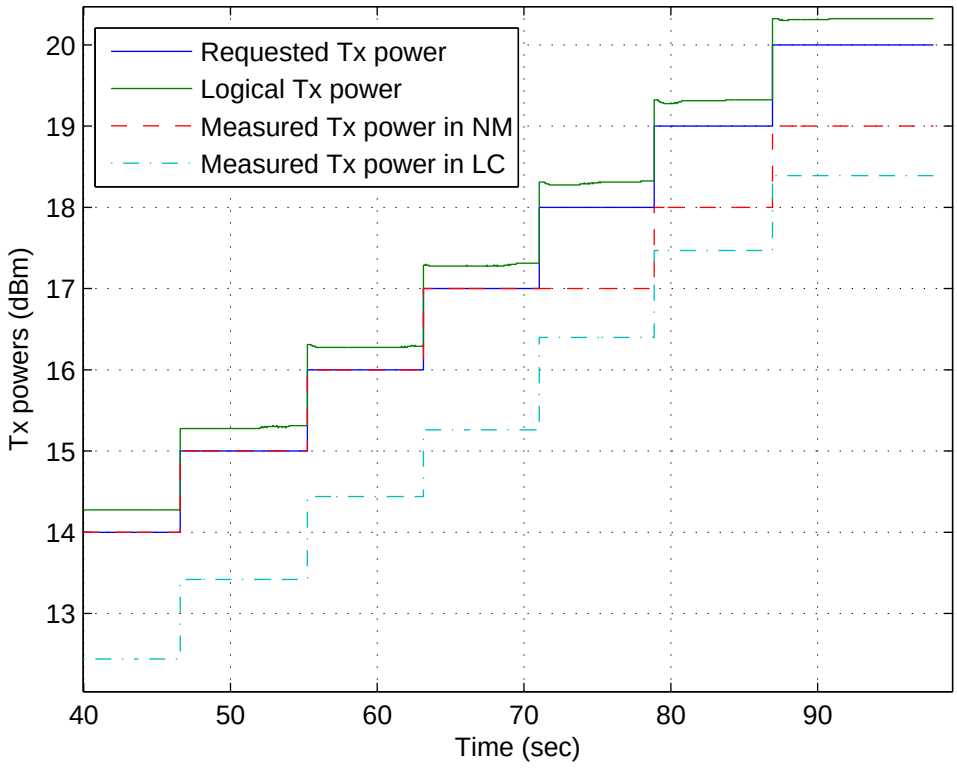

Figure 5.4: The requested and measured Tx power for local (during training) and normal modes (semi-realistic scenario) of operations.

consumption (in local mode) $P(txp)$ as a function of the Tx power txp is within $[P(txp - 2dBm)\ P(txp + 2dBm)]$. Hence, the expected worst case accuracy of the emulation system is computed below given the ± 2 dBm tolerance on Tx power.

Notations:

- Let EA stand for emulation accuracy;
- MA for mathematical approximation accuracy,;
- A for power consumption at Tx power -2 dBm, $A = P(txp - 2dBm)$ (the Tx power in both A and B are the measured values);

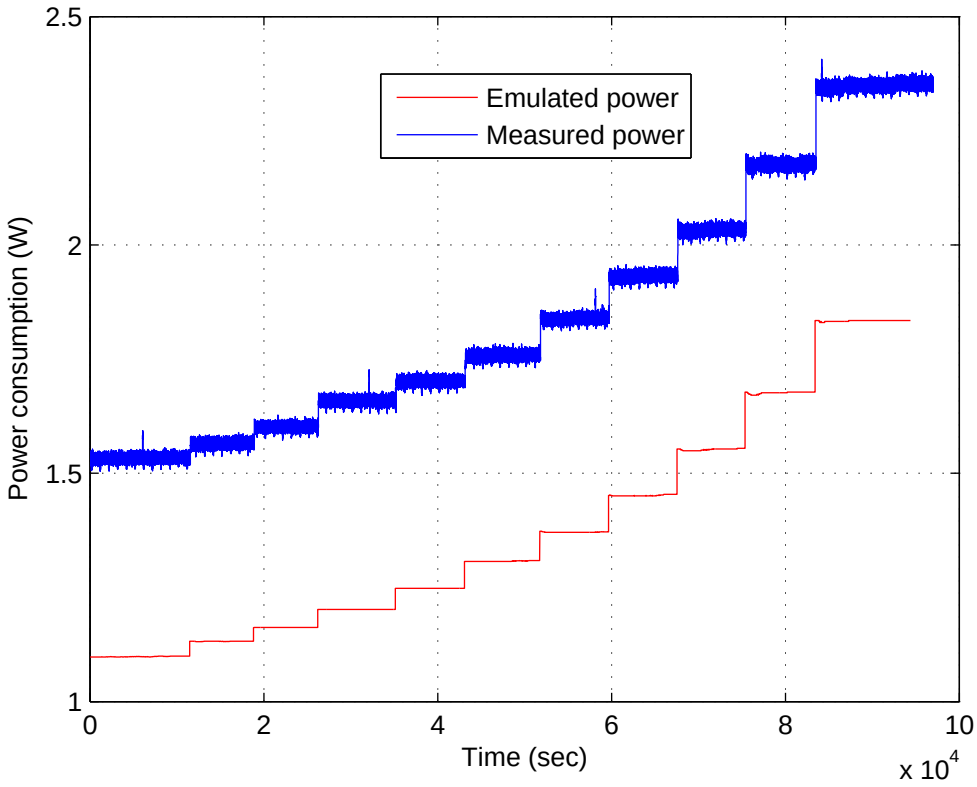

Figure 5.5: The measured and emulated power consumption while transmitting a LTE signal with ascending Tx powers. The start, step and stop Tx powers are 10, 1 and 20 dBm respectively.

- B for power consumption at Tx power +2 dBm, $B = P(txp + 2dBm)$;
- And P the power consumption as a function of Tx power.

$$EA = 100 - \left(\frac{(B - A)}{B} * 100 + (100 - MA) \right),$$

For the requested Tx powers between 10 and 23 dBm, we can expect the worst case emulation system accuracy to be 69.31% ± 2.75%. Thus, the expected

emulation accuracy is within [69.31%, 97%] ± 2.75% for worst and best cases. The worst case accuracies for the requested powers as a function of the measured Tx powers and power consumption $P(txp)$ are plotted in Figure 5.6. The Tx

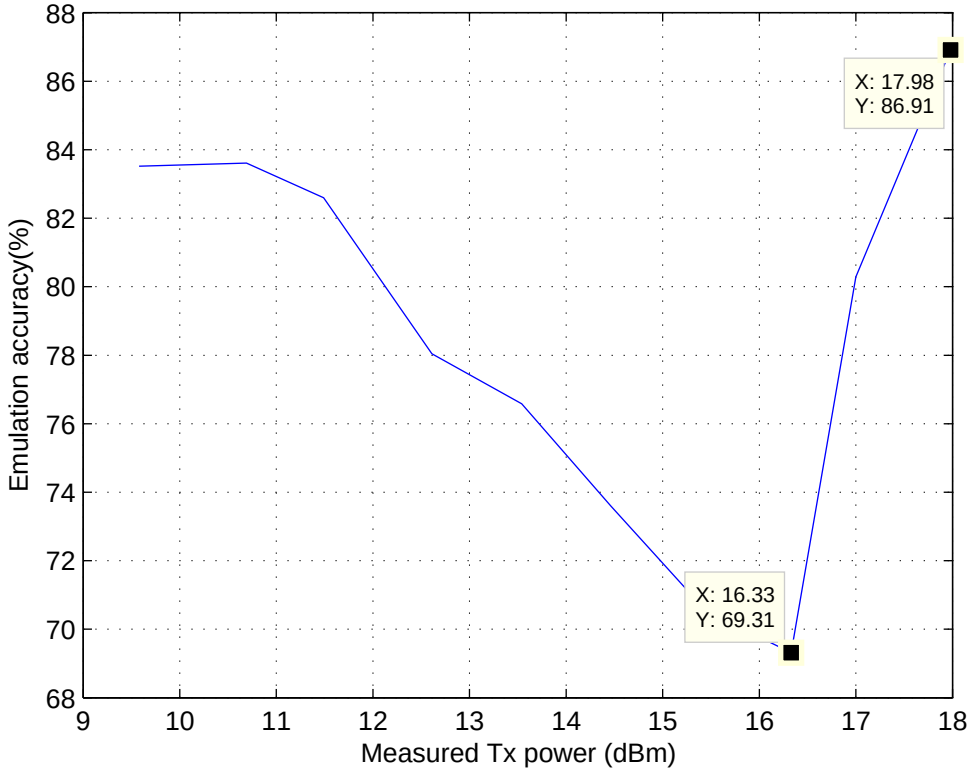

Figure 5.6: The expected emulation system accuracies as a function of the measured Tx powers.

power range from 10 dBm is chosen because it is where the significant changes, in power consumption, between the Tx powers do take effect.

In summary, the capability for emulating the RF subsystem power consumption has been shown where in the worst case scenarios when the outputted Tx power $Txp \in \{txp - 2dBm, txp + 2dBm\}$, the emulation accuracy can be as low as 69.31%. However, this is very device dependent and relies upon the tuning and calibration of the RF subsystem from device to device. The case was different for a device used early in this work [109] but it is not supported anymore. Figure 5.7 shows the emulation of the power consumption of the RF subsystem

of this device where the relative difference between the power consumption at lowest and highest Tx powers is 4.55% for the emulated and measured power consumption during a realistic transmission scenario. In Figure 5.7, the offset between local and normal modes has been omitted.

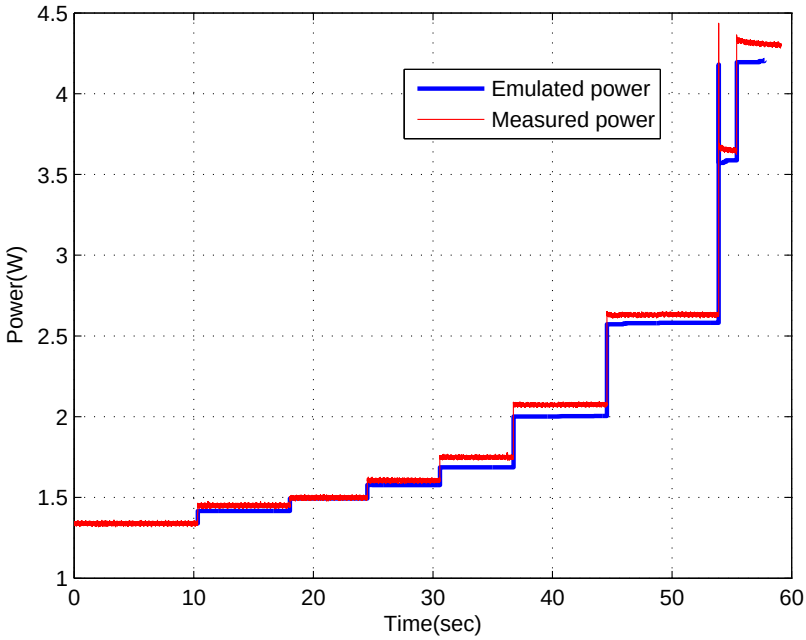

Figure 5.7: Emulation validation using a device from the early stage of the product development. The Tx power is ramped from -6 to 23 dBm.

Due to the dependence of the power control mechanisms used in local and normal modes, the development of the emulation model can be conducted in two stages depending on the maturity of the device under design. In the early phase of the design with only physical layer maturity, the emulation model would be developed in local mode. Later in the design phase, when normal mode maturity is achieved, we would then develop a corresponding emulation model whose accuracy would only depend on the accuracy of the mathematical approximation. The next section analyzes the practical use of the emulation system and the feasibility of emulating the RF subsystem power consumption for field measurements.

5.3 Integration into the power management flow

This section explains the usage of the emulation system and how this methodology can be integrated into the power management flow presented in Figure 5.8 which consists of power estimation, emulation, measurements and validation for the purpose of power consumption optimization. The power management flow starts with the power estimations which generally depend on the empirical knowledge mostly coming from experiences of previous devices. The power emulation which has so far been only for digital devices is conducted when the hardware design and corresponding RTL code is made. At this point in the design of the chipsets, the first builds of the chipsets are manufactured but with minimal functionalities (physical layer functionalities). The physical layer functionalities are hence utilized to train the emulation model for the RF subsystem which is inserted in the power management flow. When the chipset functionality matures, physical power measurements for real life scenarios are computed and compared to estimation and emulation values for validation. During the validation, analyses of the divergences between the physical power measurements, estimation and emulation are made and utilized for optimizing the power estimation and emulation methodology.

The emulation of digital circuits using the RTL hardware design is limited to simplified scenarios. This is mostly due to the requirement of the *FSDB (Fast Signal Data Base)* file, used for computing the emulated power, that fills up to a Gb for just an attach procedure (45 seconds). Moreover, we do not have the RF subsystem in the emulation environment for digital circuits, its functionality is simulated here.

Consequently, given the successful emulation of the RF subsystem power consumption for realistic scenarios early in the design process, this methodology has been evaluated for emulating the power consumption at modem level, thus for the entire modem platform. The study was conducted in our work presented in [110] where the FPLA approach was applied to find the mathematical model of the modem power consumption with an accuracy of $94.81\% \pm 2.75\%$.

We have also evaluated the feasibility of applying this methodology to the emulation of the SAR induced while transmitting from a device using our modem platform. The principles of the FLPA approach are also applied though simulation measurements are accurate enough to be used instead of physical measurements as presented in [27, 68, 69]. We have not been able to conduct SAR simulations and measurements in the course of this work. However, according to the published work, the high level parameters influencing SAR are the measurement parameters in the SAR measurement protocols defined by IEEE Std 1528-2003 [24]. These parameters include, antenna type, carrier frequency,

transmission bandwidth (if it exceeds more than 1% of the carrier frequency), output power and the distance between head and antenna.

5.3.1 Extrapolation to field measurements

The target of this work is to estimate the RF subsystem power consumption of wireless devices in real life scenarios at an early stage of the production process for the purpose of optimization. The emulation process of the power consumption conducted in the lab can also be applied on field measurements and scenarios given the logical interface parameters captured during the field testings. The power consumption estimate of the RF subsystem of the DUT, for a FTP upload scenario when the DUT is in motion, is obtained through the following steps:

1. Flash an existing mature LTE wireless device with the modem SW used by the DUT for computing the emulation model;

2. Connect the device to a trace box or insert a SDcard on which traces can be dumped, start logging the modem SW traces and connect the device to a cellular network;

3. Put the device in a car, start driving and conduct an FTP upload;

4. Extract the traces and conduct the homotopy $H_7(txp, \lambda_{bw}, \lambda_{fb7}, \lambda_T) = (1-\lambda_T)^{\alpha} H_3 + \lambda_T^{\alpha} H_6$ for the emulated power plotted in Figure 5.9.

Even though the prototype (DUT) used for training the emulation model is not capable of conducting a FTP upload, the emulated power gives an estimate (with a known accuracy) of it's power consumption for a FTP upload in motion. Thus, with this methodology, we can have an insight in the RF subsystem power consumption for all scenarios of interest given the modem SW traces. However, the training model is a 50Ω system while in the field with the antenna on, it is anything else except 50Ω. Therefore, the power consumption in the field is expected to be relatively higher due to the impendence changes that lead to higher reflection coefficients. The reflection coefficient and power consumption are expected to be positively correlated because the RF subsystem would try to compensate for the reflected power by increasing the Tx power.

5.3.2 Power consumption optimization

The target of power management is the ability of identifying and justifying hot spots. For any given scenario of the chipset, idle, call, max throughput, etc, we do have a power budget. Thus, when the emulation model has been trained, modem traces containing the logical interface parameters are used to emulate the power consumption of each scenario of interest. This provides us with the idea about how far the DUT under design is from the budgeted power. For the analysis, we would scrutinize the emulated power curve as a function of time to identify unusual behaviors. The unusual behaviors can be optimally identified by comparing the emulated curve to a reference curve of a previously power optimized chipset.

5.4 Discussion

In summary, this work has presented a new emulation methodology for the analog RF subsystem in a portable device, focusing on the LTE transmitter. The emulated power is computed as a function of the logical interface parameters and the ambient temperature using a predefined mathematical model. The mathematical model was proven to have an accuracy of $97\% \pm U$ where $U \in 2.75\%$, 2.25% and 2.7% for temperatures -10^0C, 25^0C and 55^0C, and was obtained using linear homotopy continuation.

The emulation method and results presented here focus on the RF transmitter portion because, historically, the PA was the largest power consumer in a portable device. However, in the newest smart phones, such as e.g. the Samsung Galaxy S III and its predecessor [111], dual and quad core GHz/s speed processors required for high-data rate applications start dominating the power consumption and heat removal requirements. The power consumption of these processors can be emulated by power estimation tools such as PowerTheater [15] given their RTL codes. This approach applied to realistic scenarios would have enormous memory requirements, and thus is inefficient. The approach presented in this paper can also be applied to the emulation of power consumption of the application processors under realistic operational scenarios.

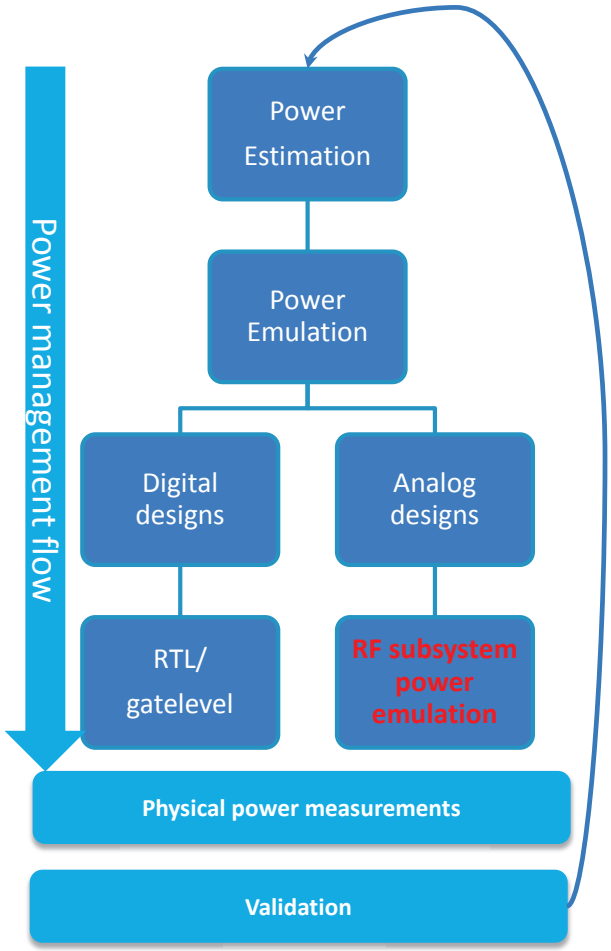

Figure 5.8: The power management flow from the design of the chipsets to the production.

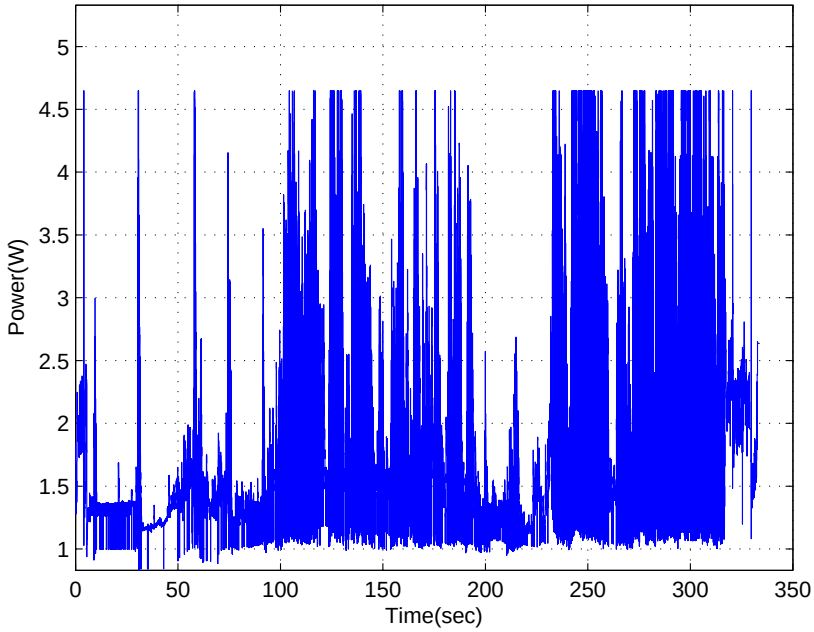

Figure 5.9: Emulated power of the DUT during a FTP upload when the device is in a moving car.

Chapter 6

Conclusions

6.0.1 Introduction

This chapter is presenting the problem domain, results and future work of the research conducted in this thesis.

6.0.2 Problem domain

The problem domain of the research in this work laid in the desire for Nokia to produce mobile devices with low power consumption and minimized electromagnetic radiation induction for users. The low power and radiation in the mobile devices is traced to the transmission process of data to the cellular network where the wireless modem plays a major part. Given the fact that the target technology of the research was LTE whose core objective is high speed cellular data transmission and also that the transmission process is one of the highest power consumers, the research narrowed down to the transmission part of the cellular device. Hence, approaches towards low power consuming digital baseband and RF subsystem of the wireless modem were in question. Low power design requires accurate power estimations/emulations during the design phase where hot spots can be identified and dealt with. Emulation approaches for digital circuits are available with accuracies of up to 90% but not for analog

circuits which the RF subsystem is composed of. Thus, the research focused on an emulation approach for the analog part of the transmission chain of the wireless modem.

The RF subsystem forwards the RF signal to the antenna for transmission which implies that the input parameters for power emulation of the RF subsystem also to do have an impact on the electromagnetic radiation generated for transmitting the RF signal. This hypothesis was also investigated in this research.

6.0.3 Results of the research

The methodology for emulating the power consumption of the RF subsystem while transmitting a LTE signal has been presented in this work. The methodology evolves from physical power measurements on the first builds of the target and utilizes prior recorded logical interface parameters of scenarios of interest to emulate the power consumption. The measurements are used for characterizing and computing the power emulation model of the DUT.

Ambiguity is raised by the fact that physical measurements are made on the target and therefore the purpose of the emulation methodology can seem trivial. The physical measurements are conducted on the first builds of the target with only physical layer functionality and thus without the possibility of measuring the power consumption for the high level scenarios as max data throughput and FTP uploading.

The methodology presented in this work provides an estimation of the power consumption of the device under design for all scenarios of interest given the logical interface parameters recorded during the execution of these scenarios. It is to be noted that the logical parameters are recorded on a mature device running on the same SW as used for the characterization.

The accuracy of the chosen emulation model has been proved up to 97% $\pm$ 2.75% but the accuracy of the emulation methodology is highly dependent on the tuning of the devices in the RF subsystem given the tolerance on the Tx power. Experiments in this work have proven emulation accuracies of 84% $\pm$ 2.75% and 94.3% $\pm$ 2.75%. It has also been proven for the device used in this work that the worst case accuracy when the Tx power is on the edges of the defined tolerances can be as low as 69.9% $\pm$ 2.75% which is an acceptable accuracy of an estimate.

6.0.4 Future work

The successful prove of concept of the power emulation methodology applying the FLPA approach for computing the emulation model has motivated the application of the methodology to the full wireless modem. The emulation of the modem power consumption during transmission has been introduced and the emulation of whole transceiver operations is the next target.

The RF subsystem and digital baseband emulation methodology that has so far focused on the uplink direction is going to be extended to cover the whole baseband and RF subsystem transceiver operations. Herein, the baseband and RF subsystem receiving operations are also to be characterized and modeled.

The methodology introduced in this work is to be applied to target devices as cell phones when the modem has gained full functionality. Though measurements can be conducted here, full scale physical power measurements for durations of several hours are not possible and so are the 2-dimensional measurements during field tests. Here, the emulation methodology is going to play a big role.

This work also looked at the possibility of emulating the SAR based on simulations and measurements in published work. The characterization and subsequently the emulation of the SAR of the target device having our modem platform is in planning at the Department of Electronic Systems at Aalborg University.

Appendix A

Appendix

A.0.5 CMOS WCDMA transmitter performances

Performance criteria / architecture	Homodyne [37]	Homodyne [38]	Homodyne [39]
Technology	0.35μm CMOS	0.18μm CMOS	90nm CMOS
Frequency range	1920 - 1980 MHz	centered at 2.0626	centered at 1.7GHz
Dynamic range	50dB	N.A	N.A
Maximum output power	6dBm	0dBm at 2GHz 6dBm at 1db compression point at 2GHz	9.6dBm
Spurious(all band)	$<$ -80dBm	N.A	N.A
ACPR	38dB at 1.92MHz	-35dBc at 5MHz ofset -50dBc at 10MHz offset	-43.2dBc at 5MHz
Power dissipation	363mW at 3.3V	223mW at 1.8V	91.4mW at 1.4V(upconverter) /3V(amplifier)
Die area	$4 \times 5mm^2$	$2 \times 4mm^2$	$1.1 \times 1.4mm^2$

Table A.1: CMOS WCDMA transmitters.

A.0.6 BiCMOS WCDMA transmitters

Performance Creteria/ architec- ture	Heterodyne [40]	Heterodyne (digital IF modulator) [41]	Heterodyne(variable IF) [42]
Technology	0.3μ SiGe BiCMOS	0.25μ SiGe BiCMOS	0.25μ SiGe BiCMOS
Frequency range	1920-1980MHz	1920-1980MHz	1920-1980MHz
Dynamic range	$>$ 100dB	N.A	N.A
Maximum output power	6dBm	3.5dBm	CW P_out = 6.2dBm HPSK P_out = 3dBm
ACPR	-45dBc at 5MHz -65dBc at 10MHz	-43dBc at 5MHz - 59dBc at 10 MHz	-47dBc at 5MHz -65dBc at 10MHz
Power dissipa- tion	213.3mW at 2.7V	58mA	285mW at 2.85V
Die area	$3 \times 3.5mm^2$	$1.8 \times 2.2mm^2$	$2.5 \times 2.5mm^2$

Table A.2: BiCMOS transmitters.

A.0.7 Architectural power efficiency comparison

Performance Creteria/ architecture	Direct conversion	LINC	Polar
DAC #	2	4	3
DAC resolution	12bit	12bit	12bit
DAC Power (mW)	40	80	>80
Baseband Filter #	2	4	3
Baseband VGA #	2	4	3
Up-Conv. Mixer #	2	4	2
IQ Divider #	1	1	1
RF-VGA #	2	4	2
PA #	1	2*	1**
System Pout (mW)	200	200	200
PA efficiency	12.5%	17%	30%
System efficiency	<12.2%	<15.9%	<26.8%

Table A.3: The transmitters power efficiency (taken from [34]).

* Non-linear PA (class C or above) with combiner. ** Power modulation PA or load modulation PA (class E)

A.0.8 Architectural performance evaluation

Transmitter/ Charac-teristic	Transmitter size	Power consump-tion	System efficiency	PA effi-ciency	Complexity**
Direct up-conversion	Good	Bad	Bad	Bad	Good
Polar modulator	Ok	Bad	Bad	Bad	Good
Polar w. offset loop	Ok	Good	Good	Good	Bad
LINC	Bad	Good	Good	Good	Bad

Table A.4: Transmitter achitectural comparison.

**Complexity; Good = low complexity and bad = high complexity

A.1 LTE review appendix

A.1.1 The orthogonality principle

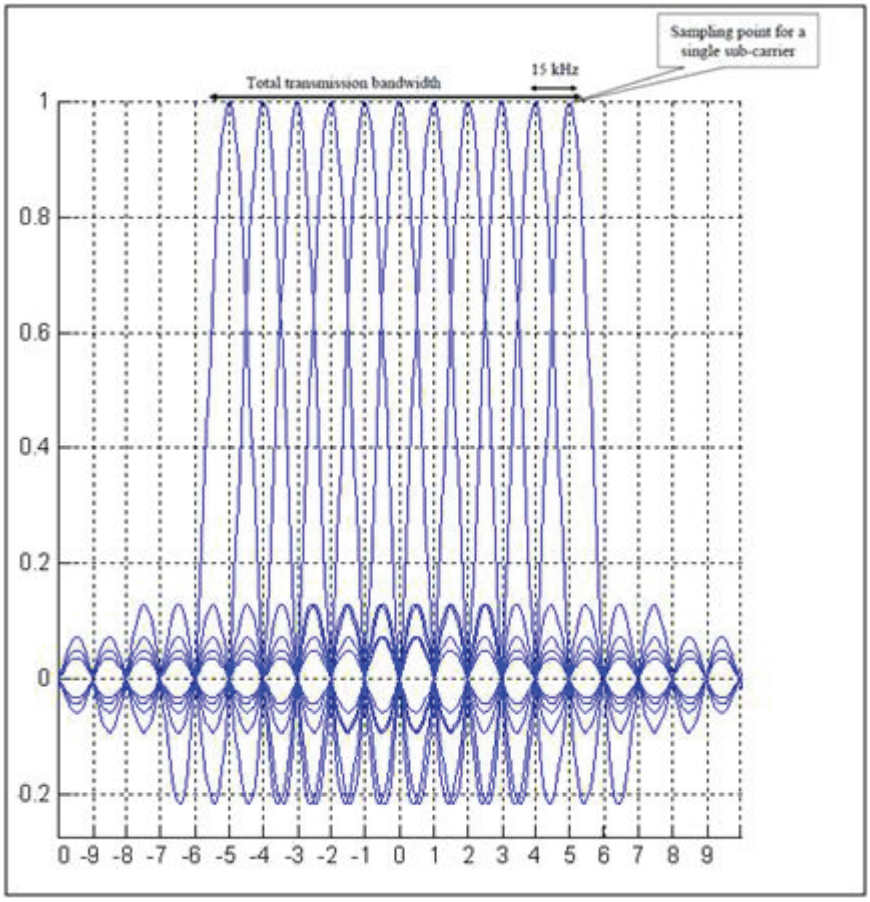

Figure A.1: The orthogonality principle.

A.1.2 The relationship between the geometric envelop and the back-off requirement.

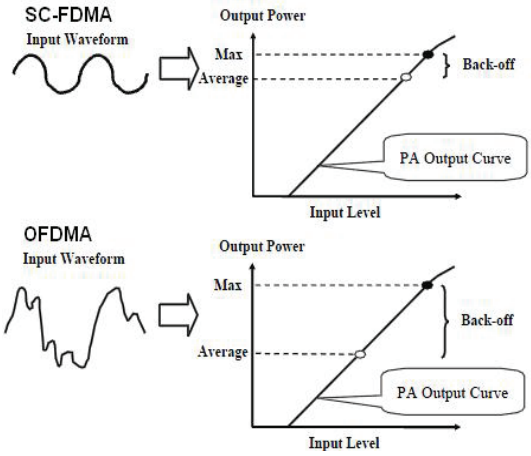

Figure A.2: Envelop Vs. PA efficiency (taken from [53]).

A.1.3 The full LTE structure

In Figure A.3, we have the whole structure of the LTE. The dashed section has been discussed in the LTE overview section and the rest of the system is discussed here.

A.1.3.1 Mobility Management Entity (MME)

The MME has the following functionalities

- Authentication and security
- Mobility management
- Subscription Profile and Service Connectivity

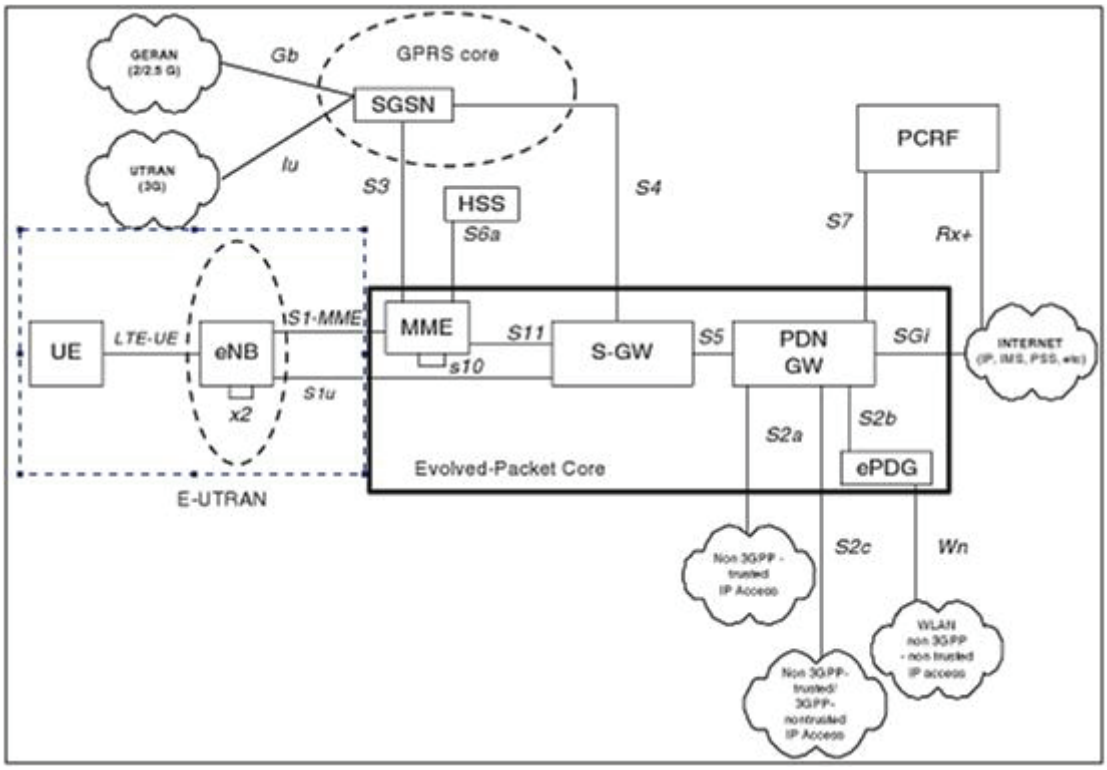

Figure A.3: LTE structure (taken from [53]).

A.1.3.2 Serving Gateway (S-GW)

The S-GW has the following functionalities

- The high level function of the S-GW in the Basic System Architetucture configuration is UP tunnel management and switching.
- When the S5/S8 interface uses PMIP, S-GW does the mapping between IP service flows in S5/S8 and GTP tunnels in S1-U interfaces and connects to PCRF to receive the mapping information.
- For the S-GWs that support PMIP S5/S8, they are responsible for mapping the IP flows in S5/S8 interface to bearers in the S1 interface.
- The S-GW acts as the anchor during mobility on commands of MME.
- The S-GW relays the data flows between eNB and P-GW.

A.1.3.3 PacketData Network Gateway (P-GW)

The P-GW is the edge router between the EPS and external packet data networks. It is also responsible for the following

- Performing traffic gating and filtering functions as required by the various services
- Allocating the IP addresses to the UE that the UE uses to communicate with the other IP hosts in the external networks
- Since the P-GW includes the PCEF, it performs gating and filtering functions as required by the policies set for the UE and the service in question
- Depending on the setting of the S5/S8 interface towards S-GW, specifically if the S-GW is based on GTP, the P-GW performs the mapping between the IP data flows to GTP tunnels which represent bearers.
- Meanwhile if the S5/S8 interface is based on PMIP, the P-GW maps all the IP service flows from external networks that belong to one UE to a single GRE tunnel and all control information is exchanged with PCRF only.

A.1.3.4 Policy and Charging Resource Function (PCRF)

The policy and Charging Resource Function (PCRF) is usually a server located with other CN elements in the operator switching centres. The PCRF is mainly responsible for policy and charging control. It also makes the following dicisions so that appropriate bearers and policing can be set up.

- Decides how to handle services in terms of QoS
- Provides PCC rules information to the PCEF located in P-GW whenever a new bearer is to be set up.
- Provides information to the BBERF located in S-GW

A.1.3.5 Home Subscription Server (HSS)

The Home Suscription Server (HSS) is a database server maintained centrally in the home operator's premises for subscription data respository for all permanent user data. The user data that can be found in the HSS

- Location of the user in the level of visited network control node
- The master copy of the subscriber profile
- The identities of those P-GWs that are in use
- The permanent key which is used to calculate the authentication vectors that are sent to a visited network for user authentification.

A.1.3.6 Services Domain

The service domain contains various subsystems which in return may contain several logical nodes for various purposes. The one subsystem that will definitely be made available is the IP Multimedia Sub-system (IMS). This subsystem is used by the operator for providing services using the session initiation protocol. This subsystem can be replaced by a server for non-IMS services.

A.1.3.7 LTE channels

LTE channels are responsible for transporting the data across the LTE radio interface in an orderly fashion. These channels do interface to the higher layers within the LTE protocol structure and enable orderly and defined segregation of the data. The data channels are grouped into 3 categories, the physical, transport and logical channels. The physical channel refers to the physical bits in the subframe, the transport channel refers to the information about where to find the logical information and the logical channels are the messages. The messages in the logical channels are either decoded directly from the physical bits of the physical channel or the decoded message pointed to by the transport channel. Below is the description of the available physical, transport and logical channels: physical channels: The channels for user and control data for both downlink and uplink.

- Downlink
  - Physical Broadcast Channel (PBCH) for system information for UEs requiring to access the network.
  - Physical Control Format Indicator Channel(PCFIC) for informing the UE about the number of OFDM symbols used for the PDCCH in a subframe.
  - Physical Downlink Control Channel(PDCCH) for carrying scheduling information.
  - Physical Hybrid ARQ Indicator Channel(PHICH) for reporting Hybrid ARQ status.
  - Physical Downlink Shared Channel for unicast and paging functions.
  - Physical Multicast Channel(PMCH) for carrying system information for multicast purposes.

- Uplink
  - Physical Uplink Control Channel(PUCCH) for sending Hybrid ARQ acknowledgments.
  - Physical Uplink Shared Channel (PUSCH) for carrying signaling and user data.
  - Physical Random Access Channel(PRACH) for random access functions.

Transport Channels: These channels transfers information to the Medium Access Control(MAC) and higher layers.

- Downlink
  - Broadcast channel (BCH): The LTE transport channel mapping to the Broadcast Control Channel(BCCH)
  - Downlink Shared Channel (DL-SCH): The main channel for data transfer.
  - Paging Channel (PCH): it conveys the PCCH.
  - Multicast Channel(MCH): This transport channel transmits MCCH information to set up multicast transmissions

- Uplink
  - Uplink Shared Channel (UL-SCH): The main channel for uplink data transfer.
  - Random Access Channel(RACH): The channel for random access requirements.

LTE logical channels

- Control channels:
  - Broadcast Control Channel (BCCH): provides system information to all mobile terminals connect to the basestation eNB.
  - Paging Control Channel (PCCH): Used for paging information when searching a unit on a network
  - Common Control Channel (CCCH): used for random access information as in setting up a network
  - Multicast Control Channel (MCCH): used for information needed for multicast reception.
  - Dedicated Control Channel (DCCH): for carrying user-spefic control information for controlling actions like power control and handovers.

- Traffic channels:
  - Dedicated Traffic Channel(DTCH) for the transmission of user data
  - Multicast Traffic Channel (MTCH) for the the transmission of multicast data

Mapping of channels: A.4 and A.5 depict the downlink and uplink channel mapping of the LTE logical, transport and physical channels.

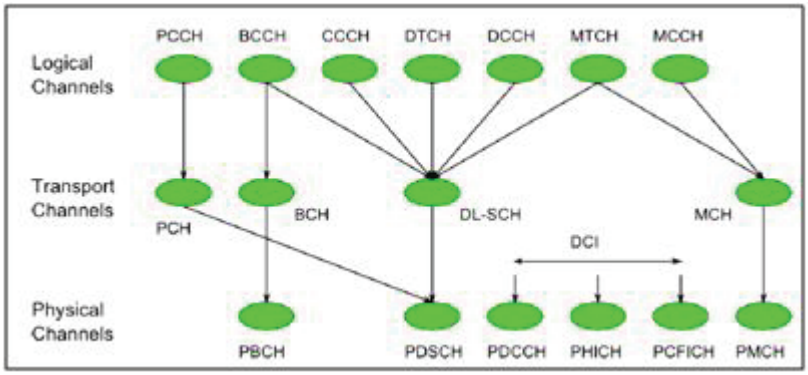

Figure A.4: Downlink mapping.

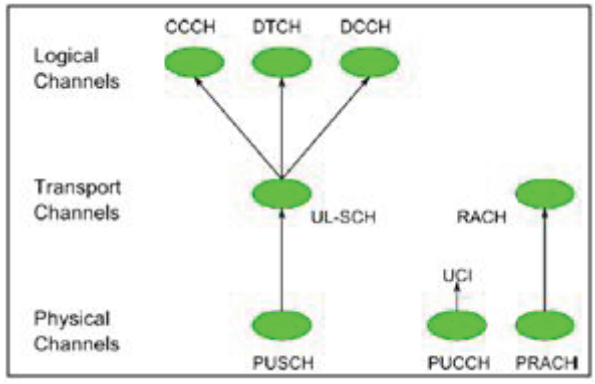

Figure A.5: Uplink map.

Bibliography

[1] B. Hochwald and D. Love, "Minimizing exposure to electromagnetic radiation in portable devices," in *Information Theory and Applications Workshop (ITA), 2012*, Feb. 2012, pp. 255–261.

[2] H. Holma and A. Toskala, *LTE for UMTS: OFDMA and SC-FDMA Based Radio Access*. Wiley & Sons, 2008, pp. 67–82.

[3] Y. Neuvo, "Cellular phones as embedded systems," in *Solid-State Circuits Conference, 2004. Digest of Technical Papers. ISSCC. 2004 IEEE International*, vol. 1, Feb. 2004, pp. 32–37.

[4] C. Aaron and G. H, "Usenixatc'10: Proceedings of the 2010 usenix conference on usenix annual technical conference." USENIX Association, 2010, pp. 271 – 284.

[5] C. A. Balanis, *Antenna Theory*. Wiley, 2005, pp. 94–104.

[6] I. McGregor, "The relationship between simulation and emulation," in *Simulation Conference*, vol. 2, Dec. 2002, pp. 1683–1688.

[7] A. Bogliolo and L. Benini, "Robust rtl power macromodels," *IEEE Transactions on Very Large Scale Integration (VLSI) Systems*, vol. 6, no. 4, pp. 578–581, Dec. 1998.

[8] F. Najm, "A survey of power estimation techniques in vlsi circuits," *IEEE Transactions on Very Large Scale Integration (VLSI) Systems*, vol. 2, no. 4, pp. 446–455, Dec. 1994.

[9] S. Gupta and F. Najm, "Power modeling for high-level power estimation," *IEEE Transactions on Very Large Scale Integration (VLSI) Systems*, vol. 8, no. 1, pp. 18–29, Feb. 2000.

[10] L. Benini, R. Hodgson, and P. Siegel, "System-level power estimation and optimization," in *International Symposium on Low Power Electronics and Design*, Aug. 1998, pp. 173–178.

[11] R. D. Gunar Schirner, "System Level Modeling of an AMBA Bus," Master's thesis, Center for Embedded Computer Systems University of California, Irvine Irvine, CA 92697-3425, USA, 2005.

[12] Cadence, http://www.cadence.com, 2011.

[13] SpyGlass, http://www.atrenta.com/solutions/spyglass-family/spyglass.htm, 2011.

[14] Galaxy, http://www.synopsys.com, 2012.

[15] PowerTheater, http://www.sequencedesign.com, 2012.

[16] PowerChecker, http://www.bulldast.com, 2012.

[17] ORINOCO, http://www.chipvision.com, 2012.

[18] D. Musiige, "Feasibility of doing power measurements in emulation environment," Master's thesis, Nokia and the Technical University of Denmark, 2009.

[19] E. Lauwers and G. Gielen, "Power estimation methods for analog circuits for architectural exploration of integrated systems," *IEEE Transactions on Very Large Scale Integration (VLSI) Systems*, vol. 10, no. 2, pp. 155–162, April 2002.

[20] S. Glock, G. Fischer, R. Weigel, T. Ussmueller, and R. Hasholzner, "A state-based power estimation methodology at system level for integrated rf front-ends," in *Semiconductor Conference Dresden (SCD), 2011*, Sept. 2011, pp. 1–4.

[21] E. Lauwers and G. Gielen, "Actif: a high-level power estimation tool for analog continuous-time filters," in *IEEE/ACM International Conference on Computer Aided Design, ICCAD-2000.*, 2000, pp. 193–196.

[22] A. Suissa, O. Romain, J. Denoulet, K. Hachicha, and P. Garda, "Empirical method based on neural networks for analog power modeling," *IEEE Transactions on Computer-Aided Design of Integrated Circuits and Systems*, vol. 29, no. 5, pp. 839–844, May 2010.

[23] B. M. Hakim, "Precise sar measurements in the near-field of rf antenna systems," Ph.D. dissertation, University of Maryland, 2006.

[24] "Approved draft ieee recommended practice for determining the peak spatial-average specific absorption rate (sar) in the human head from wireless communications devices – amendment 1: Include cad file for human head model (sam phantom) (amendment to ieee 1528-2003) replaced by 1528a-2005," *IEEE Std P1528a/D2.1*, 2005.

[25] F. C. Commission, *Evaluating compliance with FCC guidelines for human exposure to radiofrequency electromagnetic fields,*, Jan. 2001, pp. 25–27.

[26] ——, *Understanding the FCC regulations for low-power, non-licensedtransmitters*, Oct. 1993, pp. 1–29.

[27] M. Morega, A. Marinescu, and A. Morega, "Mobile phone sar analysis through experimental and numerical simulation," in *12th International Conference on Optimization of Electrical and Electronic Equipment (OPTIM)*, May 2010, pp. 95–102.

[28] B. Beard, W. Kainz, T. Onishi, T. Iyama, S. Watanabe, O. Fujiwara, J. Wang, G. Bit-Babik, A. Faraone, J. Wiart, A. Christ, N. Kuster, A.-K. Lee, H. Kroeze, M. Siegbahn, J. Keshvari, H. Abrishamkar, W. Simon, D. Manteuffel, and N. Nikoloski, "Comparisons of computed mobile phone induced sar in the sam phantom to that in anatomically correct models of the human head," *IEEE Transactions on Electromagnetic Compatibility*, vol. 48, no. 2, pp. 397–407, May 2006.

[29] K. Yee, "Numerical solution of initial boundary value problems involving maxwell's equations in isotropic media," *IEEE Transactions on Antennas and Propagation*, vol. 14, no. 3, pp. 302–307, May 1966.

[30] G. Lazzi and O. Gandhi, "On modeling and personal dosimetry of cellular telephone helical antennas with the fdtd code," *IEEE Transactions on Antennas and Propagation*, vol. 46, no. 4, pp. 525–530, Apr. 1998.

[31] B. Razavi, "Rf transmitter architectures and circuits," in *Proceedings of the IEEE Custom Integrated Circuits, 1999*, 1999, pp. 197–204.

[32] J. Groe, "Polar transmitters for wireless communications," *Communications Magazine, IEEE*, vol. 45, no. 9, pp. 58–63, Sept. 2007.

[33] R. Technologies, http://www.rficdesign.com/download/transmiter-receiver.pdf, 2010.

[34] L. Rong, F. Jonsson, L. Zheng, M. Carlsson, and C. Hedenas, "Rf transmitter architecture investigation for power efficient mobile wimax applications," in *International Symposium on System-on-Chip, 2008. SOC 2008*, Nov. 2008, pp. 1–4.

[35] B. Bakkaloglu, S. Kiaei, and B. Chaudhuri, "Delta-sigma (ΔΣ) frequency synthesizers for wireless applications," *Comput. Stand. Interfaces*, vol. 29, no. 1, pp. 19–30, Jan. 2007. [Online]. Available: http://dx.doi.org/10.1016/j.csi.2005.12.003

[36] H. H. A. Toskala;, *LTE for UMTS.* WILEY, 2009, pp. 329–331.

[37] K.-Y. Lee, S.-W. Lee, Y. Koo, H.-K. Huh, H.-Y. Nam, J.-W. Lee, J. Park, K. Lee, D.-K. Jeong, and W. Kim, "Full-cmos 2-ghz wcdma direct conversion transmitter and receiver," *IEEE Journal of Solid-State Circuits*, vol. 38, no. 1, pp. 43–53, Jan. 2003.

[38] S. Taleie, Y. Han, T. Copani, B. Bakkaloglu, and S. Kiaei, "A 0.18 x03bc;m cmos fully integrated rfdac and vga for wcdma transmitters," in *Radio Frequency Integrated Circuits Symposium*, Apr. 2008, pp. 157–160.

[39] X. Yang, A. Davierwalla, D. Mann, and K. Gard, "A 90nm cmos direct conversion transmitter for wcdma," in *Radio Frequency Integrated Circuits (RFIC) Symposium, 2007 IEEE*, June 2007, pp. 17–20.

[40] A. Bellaouar, M. Frechette, A. Fridi, and S. Embabi, "Highly-integrated sige bicmos wcdma transmitter ic," in *Solid-State Circuits Conference, 2002. Digest of Technical Papers. ISSCC. 2002 IEEE International*, vol. 1, 2002, pp. 238–463.

[41] V. Leung, L. Larson, and P. Gudem, "Digital-if wcdma handset transmitter ic in 0.25 mu;m sige bicmos," in *Solid-State Circuits Conference, 2004. Digest of Technical Papers. ISSCC. 2004 IEEE International*, vol. 1, Feb. 2004, pp. 182–521.

[42] P. Chominski, D. Malhi, L. Larson, J. Park, P. Gudem, R. Kloczkowski, C. Demirdag, A. Garlapati, and V. Pereira, "A highly integrated si/sige bicmos upconverter rfic for 3g wcdma handset applications," in *Proceedings of the 28th European Solid-State Circuits Conference, 2002. ESSCIRC 2002*, Sept. 2002, pp. 447–450.

[43] Infineon, http://www.infineon.com/cms/en/product/channel.html?channel=db3a3043163797a6011649c97e7a0734, 2010.

[44] Altair, http://www.etvcapital.com/news/news-item—lte-rf-transceiver-availability-announced-by-4g-chip-maker-altair-semiconductor.aspx, 2010.

[45] M. Racanelli, S. Voinegescu, and P. Kempf, "High performance sige bicmos technology," in *IEEE/ACES International Conference on Wireless Communications and Applied Computational Electromagnetics, 2005*, 2005, pp. 430–434.

[46] C. Galiotto, Y. Huang, N. Marchetti, and M. Zorzi, "Performance evaluation of non-ideal rf transmitter in lte/lte-advanced systems," in *European Wireless Conference, 2009*, May 2009, pp. 266–270.

[47] R. Staszewski, K. Muhammad, and D. Leipold, "Digital rf processor (drp trade;) for cellular phones," in *IEEE/ACM International Conference on Computer-Aided Design, ICCAD-2005*, Nov. 2005, pp. 122–129.

[48] R. Staszewski, J. Wallberg, S. Rezeq, C.-M. Hung, O. Eliezer, S. Vemulapalli, C. Fernando, K. Maggio, R. Staszewski, N. Barton, M.-C. Lee, P. Cruise, M. Entezari, K. Muhammad, and D. Leipold, "All-digital pll and transmitter for mobile phones," *IEEE Journal of Solid-State Circuits*, vol. 40, no. 12, pp. 2469–2482, Dec. 2005.

[49] C. Wicpalek, G. Hueber, and B. Neurauter, "Multi-mode compliant digital enhanced transmitter architectures in nano-scale cmos," in *European Conference on Wireless Technology, 2008. EuWiT 2008.*, Oct. 2008, pp. 89–92.

[50] B. Kelley, "Software defined radio for broadband ofdm protocols," in *IEEE International Conference on Systems, Man and Cybernetics, 2009. SMC 2009*, Oct. 2009, pp. 2309–2314.

[51] A. Tribble, "The software defined radio: Fact and fiction," in *Radio and Wireless Symposium, 2008 IEEE*, Jan. 2008, pp. 5–8.

[52] *3GPP TS 36.101 release 8 specification*, 2007.

[53] H. Holma and A. Toskala, *LTE for UMTS*. John Wiley and Sons, Ltd, 2009, pp. 23–65.

[54] S. Maruyama, S. Ogawa, and K. Chiba, "Mobile terminals toward lte and requirements on device technologies," in *2007 IEEE Symposium on VLSI Circuits*, June 2007, pp. 2–5.

[55] P. Vieira, P. Queluz, and A. Rodrigues, "Lte spectral efficiency using spatial multiplexing mimo for macro-cells," in *ICSPCS 2008. 2nd International Conference on Signal Processing and Communication Systems*, Dec. 2008, pp. 1–6.

[56] E. Akay, E. Sengul, and E. Ayanoglu, "Achieving full spatial multiplexing and full diversity in wireless communications," in *Wireless Communications and Networking Conference, 2006. WCNC 2006. IEEE*, vol. 4, April 2006, pp. 2046–2050.

[57] C. Ribeiro, K. Hugl, M. Lampinen, and M. Kuusela, "Performance of linear multi-user mimo precoding in lte system," in *3rd International Symposium on Wireless Pervasive Computing, 2008. ISWPC 2008*, May 2008, pp. 410–414.

[58] S. Suo, Y. Yang, Y. Tang, and Y. Wang, "Evaluation of mimo structure and channel model in lte system," in *Fourth International Conference on Communications and Networking in China, 2009. ChinaCOM 2009*, Aug. 2009, pp. 1–5.

[59] C. Zhao, R. J. Baxley, G. T. Zhou, D. Boppana, and J. S. Kenney, "Constrained clipping for crest factor reduction in multiple-user ofdm," in *Radio and Wireless Symposium, 2007 IEEE*, Jan. 2007, pp. 341–344.

[60] M. I. B. T. S. for IMT, http://standards.nortel.com/spectrum4IMT/, 2007.

[61] J. P. Andreas Gerstlauer, Rainer Domer and D. D. Gajski, *System Design: A Practical Guide with SpecC.* Kluwer Academic Publishers, 2001, pp. 63–171.

[62] Y. Li, B. Bakkaloglu, and C. Chakrabarti, "A system level energy model and energy-quality evaluation for integrated transceiver front-ends," *IEEE Transactions on Very Large Scale Integration (VLSI) Systems*, vol. 15, no. 1, pp. 90–103, Jan. 2007.

[63] G. G. P. Wambacq and J. Gerrits, *Low-Power Design Techniques and CAD Tools for Analog and RF Integrated Circuits.* Norwell, MA: Kluwer, 2001, pp. 83–103.

[64] M. Pelgrom, A. Duinmaijer, and A. Welbers, "Matching properties of mos transistors," *IEEE Journal of Solid-State Circuits*, vol. 24, no. 5, pp. 1433–1439, Oct. 1989.

[65] R. J. van de Plassche, *Integrated analog-to-digital and digital-to-analog converters.* Norwell, MA: Kluwer, 1993, pp. 90–94.

[66] J. Coburn, S. Ravi, and A. Raghunathan, "Power emulation: a new paradigm for power estimation," in *Design Automation Conference, 2005. 42nd Proceedings*, June 2005, pp. 700–705.

[67] ——, "Hardware accelerated power estimation," in *Design, Automation and Test in Europe, 2005. Proceedings*, vol. 1, 2005, pp. 528–529.

[68] Q. Yu, O. Gandhi, M. Aronsson, and D. Wu, "An automated sar measurement system for compliance testing of personal wireless devices," *IEEE Transactions on Electromagnetic Compatibility*, vol. 41, no. 3, pp. 234–245, Aug. 1999.

[69] L. Murphy and L. Williams, "Strategies for effective use of em simulation for sar," in *InternationalSymposium on Electromagnetic Compatibility, 2004. EMC 2004*, vol. 3, Aug. 2004, pp. 868–871.

[70] M. design, http://blog.medicaldesign.com/perspectives/2011/03/03/fcc-approves-finite-element-method-for-simulating-medical-device-communication-with-other-similar-devices/, 2011.

[71] CTIA, *Test Plan for Mobile Station Over the Air Performance.* 2001-2011 CTIA - The Wireless Association, 2011, pp. 70–71.

[72] R. L. Alan S. Morris, *Measurement and Instrumentation Theory and Application.* Elsevier INC, 2012, pp. 32–63.

[73] *Programmable DC Power Supplies*, 2007.

[74] *NI 6351/6353 Specifications*, 2010.

[75] *Rohde & Schwarz Signal analyzer*, 2010.

[76] R. K. E. Ramon Moore and M. J. Cloud, *Introduction to interval analysis.* SIAM (Society for Industrial and Applied Mathematics Philadelphia), 2009.

[77] S. Piramuthu, "The hausdorff distance measure for feature selection in learning applications," in *Proceedings of the 32nd Annual Hawaii International Conference on System Sciences, 1999. HICSS-32.*, vol. 6, 1999, pp. 1–7.

[78] D. Musiige, F. Anton, V. Yatskevich, L. Vincent, D. Mioc, and N. Pierre, "Rf power consumption emulation optimized with interval valued homotopies," *World Academy of Science, Engineering and Technology 81, 2011*, vol. 81, pp. 147–153, Sept. 2011.

[79] J. Laurent, N. Julien, E. Senn, and E. Martin, "Functional level power analysis: an efficient approach for modeling the power consumption of complex processors," in *Design, Automation and Test in Europe Conference and Exhibition, 2004*, vol. 1, Feb. 2004, pp. 666–667.

[80] D. Musiige, V. Laulagnet, and F. Anton, "LTE RF subsystem power consumption modeling," in *The 1st IEEE Global Conference on Consumer Electronics 2012 (IEEE GCCE 2012)*, Tokyo, Japan, 2012.

[81] N. J. Nicolas Ferry, Sylvain Ducloyer and D. Jutel, "Power/energy estimator for designing wsn nodes with ambient energy harvesting feature," *EURASIP Journal on Embedded Systems*, vol. 2011, no. 1, pp. 1–17, 2011.

[82] D. Macii and L. Negri, "An automatic power consumption measurement procedure for bluetooth modules," in *Instrumentation and Measurement Technology Conference, 2006. IMTC 2006. Proceedings of the IEEE*, April 2006, pp. 1182–1187.

[83] L. Negri, M. Sami, D. Macii, and A. Terranegra, "Fsm-based power modeling of wireless protocols: the case of bluetooth," in *Proceedings of the 2004 International Symposium on Low Power Electronics and Design, 2004. ISLPED '04.*, Aug. 2004, pp. 369–374.

[84] X. Zhang, W. Jouini, P. Leray, and J. Palicot, "Temperature-power consumption relationship and hot-spot migration for fpga-based system," in *Green Computing and Communications (GreenCom), 2010 IEEE/ACM Int'l Conference on Int'l Conference on Cyber, Physical and Social Computing (CPSCom)*, Dec. 2010, pp. 392–397.

[85] *3GPP Technical Specification 36.101*, V8.0.0 ed., 2007.

[86] *3GPP Technical Specification 36.211*, V8.9.0 ed., 2009.

[87] L. S. Sankey, "Closed-loop adaptive impedance tuners for improving rf transmitter efficiency," Ph.D. dissertation, University of Colorado at Boulder, 2007.

[88] D. M. Pozar, *Microwave Engineering.* WILEY, 2005, pp. 57–64.

[89] P. Lehana and P. Pandey, "Transformation of short-term spectral envelope of speech signal using multivariate polynomial modeling," in *2011 National Conference on Communications (NCC)*, Jan. 2011, pp. 1–5.

[90] R. L. Branham, *Scientific Data Analysis: An Introduction to Overdetermined Systems.* London: Springer-Verlag, 1990, pp. 84–119.

[91] K.-A. Toh, Q.-L. Tran, and D. Srinivasan, "Benchmarking a reduced multivariate polynomial pattern classifier," *IEEE Transactions on Pattern Analysis and Machine Intelligence*, vol. 26, no. 6, pp. 740–755, June 2004.

[92] A. Juditsky, H. Hjalmarsson, A. Benveniste, B. Delyon, L. Ljung, J. Sjöberg, and Q. Zhang, "Nonlinear black-box models in system identification: Mathematical foundations," 1995.

[93] C. M. Bishop, *Pattern Recognition and Machine Learning.* Springer, 2006, pp. 33–38.

[94] ——, *Pattern Recognition and Machine Learning.* Springer, 2006, pp. 225–284.

[95] ——, "Neural networks and their applications," *Review of Scientific Instruments*, vol. 65, no. 6, pp. 1803–1832, June 1994.

[96] P. Guillaume and R. Pintelon, "A gauss-newton-like optimization algorithm for ldquo;weighted rdquo; nonlinear least-squares problems," *IEEE Transactions on Signal Processing*, vol. 44, no. 9, pp. 2222–2228, Sep. 1996.

[97] J. Dong, B. Jiao, and L. Chen, "A new hybrid hs-dy conjugate gradient method," in *2011 Fourth International Joint Conference on Computational Sciences and Optimization (CSO)*, April 2011, pp. 94–98.

[98] Q.-j. Wu, "A nonlinear conjugate gradient method without line search and its global convergence," in *2011 International Conference on Computational and Information Sciences (ICCIS)*, Oct. 2011, pp. 1148–1152.

[99] F. Liu, H. Wang, and H. Hao, "Fletcher-reeves conjugate gradient for sparse reconstruction: Application to image compressed sensing," in *2nd Asian-Pacific Conference on Synthetic Aperture Radar, 2009. APSAR 2009*, Oct. 2009, pp. 322–325.

[100] G. G. L. Meyer and L. J. Podrazik, "A parallel projected fletcher-reeves method for optimal control," in *American Control Conference, 1992*, June 1992, pp. 147–151.

[101] E. L. Allgower and K. Georg., *Numerical continuation methods: an introduction*. Springer-Verlag New York, Inc. New York, NY, USA, 1990.

[102] A. Sodagar and G. Lahiji, "Second-order parabolic approximation: a new mathematical approximation dedicated to rom-less ddfss," in *Proceedings of the 12th International Conference on Microelectronics, 2000. ICM 2000*, 2000, pp. 47–50.

[103] B. Long, J. Hu, and P. Zhang, "Method to improve gaussian approximation accuracy for calculation of spread-spectrum multiple-access error probabilities," *Electronics Letters*, vol. 31, no. 7, pp. 529–531, Mar. 1995.

[104] Mathworks, http://www.mathworks.se/products/matlab/, 2013.

[105] H. B. Brooks, "The accuracy of commercial electrical measurements," *Transactions of the American Institute of Electrical Engineers*, vol. XXXIX, no. 1, pp. 495–615, Jan. 1920.

[106] N. Stanciu, D. Stanescu, and W. Szabo, "Evaluation of measurement uncertainty in determining the supply voltage, dips and swells, in low voltage," in *2012 13th International Conference on Optimization of Electrical and Electronic Equipment (OPTIM)*, May 2012, pp. 265–274.

[107] P. da Silva Hack and C. ten Caten, "Measurement uncertainty: Literature review and research trends," *IEEE Transactions on Instrumentation and Measurement*, vol. 61, no. 8, pp. 2116–2124, 2012.

[108] A. Giordani and L. Mari, "Measurement, models, and uncertainty," *IEEE Transactions on Instrumentation and Measurement*, vol. 61, no. 8, pp. 2144–2152, 2012.

[109] F. A. D. M. D. Musiige, V. Laulagnet, "Lte handset rf power consumption emulation," in *The Third International Conference on Digital Information Processing and Communications*, Feb. 2013, pp. 371–378.

[110] D. Musiige, L. Vincent, and F. Anton, "Lte modem power consumption, sar and rf signal strength emulation," in *2012 4th International Congress on Ultra Modern Telecommunications and Control Systems and Workshops (ICUMT)*, 2012, pp. 1–6.

[111] Samsung, http://www.samsung.com/us/galaxy-s-3-smartphone/?cid=ppc-, 2011.

Index